Forschungsbericht 2017-10

An Aeroelastic Coupled Adjoint Approach for Multi-Point Designs in Viscous Flows

Mohammad Abu-Zurayk

Deutsches Zentrum für Luft- und Raumfahrt
Institut für Aerodynamik und Strömungstechnik
Braunschweig

ISSN 1434-8454

ISRN DLR-FB--2017-10

M. Abu-Zurayk

ISRN DLR-FB--2017-10

Deutsches Zentrum für Luft- und Raumfahrt

Herausgeber
Deutsches Zentrum
für Luft- und Raumfahrt e. V.
Bibliotheks- und
Informationswesen
D-51170 Köln
Porz-Wahnheide
Linder Höhe
D-51147 Köln

Telefon (0 22 03) 6 01 - 44 44
Telefax (0 22 03) 6 01 - 47 47

ISSN 1434-8454

Aeroelastic adjoint approach, aerodynamic shape optimization, gradient-based optimization

Mohammad Abu-Zurayk
Institute of Aerodynamics and Flow Technology of the DLR, Braunschweig

An Aeroelastic Coupled Adjoint Approach for Multi-Point Designs in Viscous Flows
Doctoral Thesis Rheinisch-Westfälische Technische Hochschule Aachen
DLR-Forschungsbericht 2017-10, 2017, 86 pages, 61 figs., 7 tabs., 77 refs., 27.00 €

As the wing flies, its structural elasticity interacts with the aerodynamic loads and the wing deforms. This deformation influences the aerodynamic flow over the wing. Hence, besides employing high-fidelity flow equations, considering the structural elasticity is necessary for an accurate prediction of the wing aerodynamic coefficients. Wing shape optimizations that consider high-fidelity aeroelastic effects are computationally costly and therefore the gradient-based algorithms are suitable for them. This study presents an efficient approach for computing the gradients required for such optimizations. An existing viscous flow adjoint approach is extended to include the structural elasticity effects. The contribution of this work is, to differentiate the flow-structure coupling methods and to implement the coupled adjoint equations in order to use it within industrially relevant wing-shape optimizations. The advantages of this coupled aeroelastic adjoint approach are that it computes the gradients accurately and nearly independently of the number of design parameters engaged in the optimization, hence it is possible to use high number of design parameters. This allows high-fidelity multipoint optimizations within acceptable computational time. In this context, it is found that the adjoint approach is saving more than 80% of the computational cost when compared to the conventional finite differences approach for computing the gradients. After successfully validating the gradients obtained with the developed approach, four optimization scenarios are performed on a wing-body configuration in a transonic flow regime. The effects of considering several flight points as well as considering some rough weight constraint are tested and this latter constraint shows beneficial results for aerodynamics as well as the structure of the aircraft.

aeroelastische Adjungiertenmethode, Aerodynamische Formoptimierung, Gradient-basierte Optimierung *(Publiziert in Englisch)*

Mohammad Abu-Zurayk
Institut für Aerodynamik und Strömungstechnik des DLR, Braunschweig

Gekoppletes adjungiertes Verfahren für den Navier-Stokes basierten aeroelastischen Mehrpunktentwurf
Dissertation Rheinisch-Westfälische Technische Hochschule Aachen
DLR-Forschungsbericht 2017-10, 2017, 86 Seiten, 61 Bilder, 7 Tabellen, 77 Literaturstellen, 27,00 € zzgl. MwSt.

Während des Fluges wird der Flügel basierend auf der Interaktion der Aerodynamik mit der Elastizität der Struktur deformiert. Diese Deformation beeinflusst das aerodynamische Strömungsfeld und demzufolge ist die Berücksichtigung der Elastizität der Struktur bei der Optimierung der Flügelform notwendig, um die aerodynamischen Beiwerte präzise vorherzusagen. Gradienten basierende Optimierungsalgorithmen sind effizient und deshalb geeignet für aeroelastische Formoptimierung des Flügels mit hochwertigen numerischen Verfahren. Diese Arbeit präsentiert ein effizientes Verfahren um die Gradienten, die für solche Optimierungen notwendig sind, zu berechnen. Eine bereits existierende Methode, die reibungsbehaftete Strömungsadjungierte, wird erweitert um die Elastizitätseffekte der Struktur zu berücksichtigen. Der Hauptbestandteil dieser Arbeit besteht aus der Ableitung der Methoden zur Strömung-Struktur Kopplung und der Implementierung der gekoppelten adjungierten Gleichungen. Vorteilhaft bei dieser gekoppelten aeroelastischen Adjungiertenmethode ist, dass sie die Gradienten genau und nahezu unabhängig von der Anzahl der Entwurfsparameter der Optimierung berechnet. Dies ermöglicht hochwertigen numerischen Verfahren Mehrpunktoptimierungen mit akzeptablem numerischem Aufwand. In diesem Zusammenhang kann festgestellt werden, dass die numerischen Kosten mit dieser adjungierten Methodik um mehr als 80% reduziert werden können im Vergleich zu einem konventionellen finite Differenzen Ansatz. Nachdem das Verfahren zur Berechnung der Gradienten erfolgreich validiert ist, werden vier Szenarien für eine Flügel-/Rumpfgeometrie bei transsonischen Anströmbedingungen optimiert. Dabei werden die Einflüsse sowohl von verschiedenen Flugpunkten als auch einer Randbedingung hinsichtlich des Gewichts des Flugzeugs untersucht. Diese Randbedingung zeigt vorteilhafte Ergebnisse sowohl für die Aerodynamik als auch für die Struktur des Flugzeugs.

Forschungsbericht 2017-10

An Aeroelastic Coupled Adjoint Approach for Multi-Point Designs in Viscous Flows

Mohammad Abu-Zurayk

Deutsches Zentrum für Luft- und Raumfahrt
Institut für Aerodynamik und
Strömungstechnik
Braunschweig

86 Seiten
61 Bilder
7 Tabellen
77 Literaturstellen

Deutsches Zentrum
DLR für Luft- und Raumfahrt

An Aeroelastic Coupled Adjoint Approach for Multi-Point Designs in Viscous Flows

Von der Fakultät für Mathematik, Informatik und Naturwissenschaften der RWTH Aachen University zur Erlangung des akademischen Grades eines Doktors der Ingenieurwissenschaften genehmigte Dissertation

vorgelegt von
Mohammad Abu-Zurayk
Aus Amman / Jordanien

Berichter: Univ.-Prof. Dr. Nicolas R. Gauger
Univ.-Prof. Dr. rer. nat. Martin Frank
Univ.-Prof. Marek Behr, Ph.D.
Prof. Dr. Norbert Kroll

Tag der mündlichen Prüfung: 12. Mai 2016

Kurzfassung

Während des Fluges wird der Flügel basierend auf der Interaktion der Aerodynamik mit der Elastizität der Struktur deformiert. Diese Deformation beeinflusst das aerodynamische Strömungsfeld und demzufolge ist die Berücksichtigung der Elastizität der Struktur bei der Optimierung der Flügelform notwendig, um die aerodynamischen Beiwerte präzise vorherzusagen. Gradienten basierende Optimierungsalgorithmen sind effizient und deshalb geeignet für aeroelastische Formoptimierung des Flügels mit hochwertigen numerischen Verfahren. Diese Arbeit präsentiert ein effizientes Verfahren um die Gradienten, die für solche Optimierungen notwendig sind, zu berechnen.

Eine bereits existierende Methode, die reibungsbehaftete Strömungsadjungierte, wird erweitert um die Elastizitätseffekte der Struktur zu berücksichtigen. Der Hauptbestandteil dieser Arbeit besteht aus der Ableitung der Methoden zur Strömung-Struktur Kopplung und der Implementierung der gekoppelten adjungierten Gleichungen.

Vorteilhaft bei dieser gekoppelten aeroelastischen Adjungiertenmethode ist, dass sie die Gradienten genau und nahezu unabhängig von der Anzahl der Entwurfsparameter der Optimierung berechnet. Dies ermöglicht hochwertigen numerischen Verfahren Mehrpunktoptimierungen mit akzeptablem numerischem Aufwand. In diesem Zusammenhang kann festgestellt werden, dass die numerischen Kosten mit dieser adjungierten Methodik um mehr als 80% reduziert werden können im Vergleich zu einem konventionellen finite Differenzen Ansatz.

Nachdem das Verfahren zur Berechnung der Gradienten erfolgreich validiert ist, werden vier Szenarien für eine Flügel-/Rumpfgeometrie bei transsonischen Anströmbedingungen optimiert. Dabei werden die Einflüsse sowohl von verschiedenen Flugpunkten als auch einer Randbedingung hinsichtlich des Gewichts des Flugzeugs untersucht. Diese Randbedingung zeigt vorteilhafte Ergebnisse sowohl für die Aerodynamik als auch für die Struktur des Flugzeugs.

Abstract

As the wing flies, its structural elasticity interacts with the aerodynamic loads and the wing deforms. This deformation influences the aerodynamic flow over the wing. Hence, besides employing high-fidelity flow equations, considering the structural elasticity is necessary for an accurate prediction of the wing aerodynamic coefficients. Wing shape optimizations that consider high-fidelity aeroelastic effects are computationally costly and therefore the gradient-based algorithms are suitable for them. This study presents an efficient approach for computing the gradients required for such optimizations.

An existing viscous flow adjoint approach is extended to include the structural elasticity effects. The contribution of this work is, to differentiate the flow-structure coupling methods and to implement the coupled adjoint equations in order to use it within industrially relevant wing-shape optimizations. The advantages of this coupled aeroelastic adjoint approach are that it computes the gradients accurately and nearly independently of the number of design parameters engaged in the optimization, hence it is possible to use high number of design parameters. This allows high-fidelity multipoint optimizations within acceptable computational time. In this context, it is found that the adjoint approach is saving more than 80% of the computational cost when compared to the conventional finite differences approach for computing the gradients.

After successfully validating the gradients obtained with the developed approach, four optimization scenarios are performed on a wing-body configuration in a transonic flow regime. The effects of considering several flight points as well as considering some rough weight constraint are tested and this latter constraint shows beneficial results for aerodynamics as well as the structure of the aircraft.

Table of Contents

Kurzfassung ..... **ii**

Abstract ..... **iii**

Table of Contents ..... **iv**

List of Figures ..... **vi**

List of Tables ..... **viii**

Nomenclature ..... **ix**

Acknowledgement ..... **xii**

Chapter 1: Introduction **1**

1.1 Problem Statement 1

1.2 Background on Aerodynamic Optimization 2

1.3 Aero-Structural Effects on Aircraft Design 4

1.4 Literature Review 5

1.5 Objective and Outline 7

Chapter 2: Adjoint Approach for Aerodynamic Shape Optimization **8**

2.1 Optimization Algorithms 8

2.2 Gradients Computation Methods 10

2.3 Formulation of the Adjoint Approach 14

2.4 Application of the Discrete Adjoint Approach for Aerodynamic Shape Optimization 18

Chapter 3: Adjoint formulation for Coupled Aero-Elastic Systems **26**

3.1 Aero-Structural Problems 26

3.2 Derivation of the Coupled Aero-Structural Adjoint 32

3.3 Terms of the Coupled Aero-Structural Adjoint Equations 35

3.4 Solution of the Coupled Aero-Elastic Adjoint Equation 42

3.5 Convergence of the Coupled Aero-Elastic Adjoint Solution 43

3.6 Terms of the Gradients 44

Chapter 4: Elements of the Aero-Elastic Coupled Optimization **47**

4.1 The Computational Structure Model 48

4.2 Effect of Considering Viscosity 48
4.3 CFD Mesh Study 50
4.4 Optimization Algorithm Study 54
4.5 Design Parameters Study 55

Chapter 5: Optimization Scenarios 60
5.1 Unconstrained Single-Point Optimization 60
5.2 Unconstrained Multi-Point Optimization 63
5.3 Constrained Single-Point Optimization 69
5.4 Constrained Multi-Point Optimization 74
5.5 Computational Efficiency 77

Chapter 6: Conclusions and Outlook 81

References 83

List of Figures

Figure 1: The main components of an Aerodynamic optimization 3
Figure 2: Wing bending under aero-structural effects [21] 4
Figure 3:Comparison of pressure distributions at different sections of a transport aircraft wing, the effect of considering wing's elasticity [21] 5
Figure 4: Global sensitivity map; drag gradients of the wing 9
Figure 5: Gradient approximation using the finite differences approach 10
Figure 6: The effect of the step-size on the gradients (whole view & zoomed view) 12
Figure 7: Freeform-Deformation parameterization of an ONERA M6 wing 19
Figure 8: *FFD* parameterization on a wing-body configuration 20
Figure 9: Components of an aerodynamic shape optimization 20
Figure 10: MDOrmec unstructured surface grid 21
Figure 11: Gradients validation for drag at constant lift 23
Figure 12: Convergence history of the aerodynamic shape optimization 23
Figure 13: Aerodynamic optimization results; chordwise Cp distribution 24
Figure 14: Aerodynamic optimization, spanwise drag (up) and lift (bottom) distributions 25
Figure 15: Components of the Aero-Structural Coupling Loop 27
Figure 16: Converged Aero-Structual Coupling 28
Figure 17: Convergence of the aero-structural coupling 29
Figure 18: Wing shapes after the different coupling steps 29
Figure 19: Flexural axis of a backward-swept wing 30
Figure 20: Comparison of bending and twist for the jig and flight wing shapes 31
Figure 21: C_p at a section close to wing tip (η=0.9) 32
Figure 22: Pressure interpolation nodes from *CFD* grid (right) to the *CSM* grid (left) 37
Figure 23: Force interpolation on the *CSM* grid with quadrilateral elements 38
Figure 24: Validation of the differentiation of the linear interpolation 39
Figure 25: Validation of the differentiation of the RBF mesh deformation tool 42
Figure 26: Convergence history of the solution of the aerodynamic adjoint equation 44
Figure 27: Convergence history of the aerodynamic and structural adjoint vectors 44
Figure 28: Validation of the gradients computed by coupled adjoint approach 46
Figure 29: Information flow within the Aero-Elastic optimization 47
Figure 30: The *CSM* grid employed in the optimizations 48
Figure 31:The grids employed in the flow fidelity study 49
Figure 32: The convergence history of the inviscid and the viscous optimization and the viscous evaluation of the resulting inviscid design 50
Figure 33: C-type (left) and O-type (right) structured grids 51
Figure 34: behind the wing tip, before (upper) and after (lower) the wing deformation 52

Figure 35: Grid refinement study 53
Figure 36: Convergence histories of the optimizations driven by *CG* and *VMM* 55
Figure 37: The top (up) and front (bottom) views of the basic design parameters setting, green are free and red are fixed parameters 57
Figure 38: Top view of the chordwise refined (CWR) setting 57
Figure 39: Top view of the spanwise refined (SWR) setting 58
Figure 40: history of the optimizations performed within the design parameters study 58
Figure 41: Convergence history of the unconstrained single point optimization 60
Figure 42: The wing sections' thicknesses were kept constant throughout the optimization 61
Figure 43: Top and front views for the Cp contour on both baseline and optimized configurations 61
Figure 44: Chordwise Cp distribution of both baseline and optimized configurations for the single point optimization 62
Figure 45: The flow separation at the wing-body junction for both configurations in the single point optimization. 62
Figure 46: Twist distribution along the wings spans for the baseline and the optimized configurations 63
Figure 47: Comparison of load distributions; lift (upper), Cl (middle) and drag (lower) 64
Figure 48: The points considered in the multi-point optimization 65
Figure 49: Convergence history of the multi-point optimization objective 66
Figure 50: The LoD curve for the multi-point and single-point optimizations in comparison to the baseline configuration 67
Figure 51: The drag rise trends for the multi-point and the single-point optimizations in comparison to the baseline configuration 68
Figure 52: The resulting forces and moments on the wing 69
Figure 53: Rough relation between the wing mass and the rolling moment at constant C_L 71
Figure 54: Convergence of the constrained single-point optimization 72
Figure 55: Spanwise local C_L and lift force distributions for the constrained and the unconstrained single-point optimizations compared to the baseline configuration 73
Figure 56: The Von-Mises stress for the wings resulting from the constrained and the unconstrained optimizations, in comparison to the baseline configuration 74
Figure 57: C_{MX} of the Baseline configuration at the five points in comparison to the C_{MX} of the designs resulting from the constrained as well as the unconstrained optimizations 75
Figure 58: Convergence history of the constrained multi-point optimization cost function 75
Figure 59: C_{MX} convergence throughout the constrained multi-point optimization 76
Figure 60: The LoD trends for the constrained optimizations 78
Figure 61: The drag rise trends for the constrained optimization 79

List of Tables

Table 1: Number of nodes for the grids in study 53
Table 2: The aerodynamic coefficients of the initial and the deformed configurations for both grids 54
Table 3: Drag reduction for the optimized flight conditions..... 66
Table 4: CD, CMx and the mass of the unconstrained single-point optimization 71
Table 5: Drag reduction for the five points in the constrained multi-point optimization 76
Table 6: Number of required coupled adjoint computations whenever the gradient is required 77
Table 7: Computational cost of the various optimizations..... 80

Nomenclature

A	Vector of aerodynamic shape design variables
b	Wing span
C	Inequality constraint
C_D	Drag coefficient
C_L	Lift coefficient
C_{MX}	Rolling moment coefficient
C_P	Pressure coefficient
CAD	Computer aided design
CFD	Computational fluid dynamics
CG	Conjugate gradient
CS	Complex step approach
CSM	Computational structure mechanics
D	Vector of design variables
DOE	Design of experiment
DLR	Deutsches Zentrum für Luft- und Raumfahrt; German aerospace research center
f	Optimization objective
F	Forces and aerodynamic loads applying on the structure
FD	Finite differences
FFD	Free-form deformation technique
FE	Finite element
G	Equality constraints
h	Finite differences step size
I	Optimization cost function
K	Structure stiffness matrix
L	Lagrange
LoD	Lift to drag ratio

MDO	Multi-disciplinary design optimization
MDOrmec	MDO of rear-mounted engine configuration; a DLR internal project
n	Normal unit vector
NS	Navier-Stokes flow equations
p	Pressure
p_∞	Far-field pressure
PDE	Partial differential equation
q_∞	Stagnation pressure
R_a	Residual of aerodynamic flow equations
R_m	Residual of mesh deformation
R_s	Residual of structure equations, governed by linear elasticity here.
RANS	Reynolds-averaged Navier-Stokes flow equations
RBF	Radial basis function
S_w	Wing area
SA	Sensitivity analysis
SD	Steepest descent algorithm
SQP	Sequential quadratic programming
T	Structural design variable (thickness)
u	Structural deformations
v	Flow velocity
VMM	Variable metric method
w	Flow state variables
x,y,z	Coordinate vectors

Greek Letters

α	Flow angle of attack
ε_{ij}	Euclidian distance between points i and j
η	Normalized span of the wing
ρ	Flow density

σ	Surface deformation
τ	Volume deformation
ψ_a	Aerodynamic adjoint field (or Lagrange multiplier)
ψ_s	Structure adjoint field
ψ_m	Mesh adjoint field

Acknowledgement

Firstly, I would like to express my sincere gratitude to my advisors; Prof. N. Gauger and Prof. N. Kroll for their aspiring guidance, their invaluable criticism and the continuous motivation they armed me with throughout this journey. Besides that, I am very thankful to Prof. N. Kroll for giving me the chance to complete my thesis at DLR, Institute for Aerodynamics and Flow technologies, and to Prof. N. Gauger for his constant supervision, which enriched my mathematical knowledge.

In addition, I would like to thank the reviewers of my thesis and the exam committee; Prof. Martin Frank, Prof. Marek Behr, Prof. Sebastian Noelle, Prof. Siegfried Müller and Prof. Gerhard Hiß for their time, the useful discussions we had and the enlightening questions.

Furthermore, I want to take this opportunity to thank, with much appreciation, my colleagues; Caslav Ilic, and Joel Brezillon for the intensive and constructive discussions. I am also grateful to my colleagues Anna Pal, Markus Widhalm, Arthur Stück, Dirk Franke, Stefan Görtz, Olaf Brodersen, Stefan Keye, Martin Kruse, Tobias Wunderlich, and to my former colleague Richard Dwight for the fruitful talks.

بالإضافة لذلك, أود, و بلغتي العزيزة, أن أشكر عائلتي الحبيبة على الدعم المتواصل. أبدأ بديانا, نصفي الأفضل, التي حملت بمفردها طوال عام على الأقل ما نتقاسم عادة لتتيح لي ظروف النجاح. أشكرك على صبرك الجميل. أشكرك على الإيمان بي, و على الكلمات الرقيقة التي قيلت حين احتجتها. أشكرك على الأثر الظاهر في سطور هذه الرسالة. أود أيضا أن أتقدم بالشكر لإخوتي إياد, رند ووعد على الدعم المعنوي الدائم. وأنتهي ببدايتي, أمي و أبي الحبيبين. أشكركما على الدعم الدائم بكل اشكاله و على الدفء والحكمة اللذين، برغم البعد، يرافقان كل حديث بيننا.

Chapter 1: Introduction

1.1 Problem Statement

Due to the increase in fuel prices and the strict constraints on emission and other environmental aspects, the aircraft industry is immensely investing in the search for advanced designs that consume less fuel and produce less emission. The Flightpath-2050 [1] provides a vision for Europe's aviation systems and industries by the year 2050. It expects a 75% reduction in CO_2 emission per passenger kilometre, a 90% reduction in NOx emission and a 65% reduction in noise emission of air vehicles -by 2050- relative to those of the year 2000. On the other hand, the worldwide air traffic is predicted to grow by 4-5 % per year, which makes the fulfilment of these expectations a highly challenging task.

Aircraft optimization, which can be performed using numerical techniques, is an indispensable choice to face the Flightpath-2050 challenges and to increase the aircraft's efficiency. In the research field, numerical optimization techniques have been intensively used for aircraft design in the last decades [2, 3, 4, 5] and proved trustworthy. They have maturely covered a wide range of applications in the aircraft design. Some techniques dealt with reducing the aircraft structural weight, while others optimized the wing planform or the aircraft tail in order to enhance its aerodynamic performance. In industry, on the other hand, the use of optimization techniques for aircraft design is still modest, several papers [6, 7, 8, 9] show the first integration of numerical optimization in the design process.

Aerodynamics plays a significant role in driving the aircraft efficiency; the lift/drag (*LoD*; lift over drag) ratio, for example, directly affects the aircraft fuel consumption. However, considering the aerodynamics solely in the aircraft optimization process is not sufficient, since it is strongly coupled with other disciplines that affect it, and get affected by it, like the elasticity of the aircraft structure. Therefore, the relevant disciplines need to be considered as well during such optimizations.

An optimization that incorporates more than one discipline is called a multidisciplinary design optimization (MDO). Employing MDO in aircraft design, yields realistic designs that fulfil the constraints of the engaged disciplines and reduces the development risks. MDO also helps in understanding the influences one discipline has on another. However, the complexity of the problem in MDO significantly increases when compared to single-disciplinary optimizations. The computational cost of MDO is generally higher than the sum of the single-disciplinary optimizations' computational costs for the disciplines included in the MDO problem [10]. Therefore, the optimization algorithms that drive the MDO need to be efficient.

Furthermore, in a MDO, that is intended to meet the high challenges of Flightpath-2050, three aspects are necessary. The first aspect concerns using high-fidelity models for the engaged disciplines, which increases the reliability of the resulting designs. The second aspect lies in employing approaches that can handle high number of design parameters. This gives the optimizer more freedom and a larger space to find the optimum design. The third aspect lies in performing the design at several aircraft operating points (flight

conditions) simultaneously. This aspect leads to a design that performs better not only at a single flight condition (the aircraft's cruise point for example), but at other operating points as well. However, considering these three aspects will only increase the computational cost of MDO, which emphasizes again the need for efficient optimization algorithms.

Optimization algorithms require the value of the function being optimized after any design iteration. In addition to that, some algorithms require also the sensitivity of the function being optimized with respect to the design parameters. These so-called gradient-based algorithms are known to be efficient because gradients contain information about the fastest direction of improvement. However, computing the sensitivities (gradients) for these efficient algorithms with the conventional finite-differences approach is costly when the number of design parameters (second aspect) is high. The cost is then linearly dependent on the number of design parameters. This raises the need for an efficient approach to compute the gradients employed in high-fidelity multidisciplinary gradient-based optimizations.

1.2 Background on Aerodynamic Optimization

As mentioned previously, a meaningful measure for evaluating the aircraft's aerodynamic efficiency is the lift/drag ratio. The higher this ratio, the larger the distance an aircraft can fly, or the lower the fuel consumption. However, a precise evaluation of this measure requires an accurate computation of the aerodynamic loads (lift and drag). Two aspects affect the accuracy of their computation directly; the first concerns the fidelity of the numerical aerodynamic model employed, and the second lies in including the relevant disciplines while computing the aerodynamic loads.

The aerodynamic loads can be evaluated either using the wind tunnel or by employing adequate numerical techniques. The constant development in computational fluid dynamics (*CFD*) and the evolution of the high performance computing are helping this relatively new field to play a bigger role in the development within aerospace sciences. In *CFD*, the fluid flow can be modelled at different levels of fidelity. The higher the fidelity, the more accurate and more costly-to-compute the model becomes. One flow model is represented by the Euler equations. These equations describe rotational but inviscid flows. Hence, they can be used to predict the lift to some extent (over predicted) and the drag due to lift, but not the friction part of drag. If the viscous terms are included in the flow model, the so-called Navier-Stokes (*NS*) equations result. These equations can accurately describe the different flow regimes. Therefore, the *RANS* (the Reynolds averaged Navier-Stokes) equations are required for reliable aerodynamic shape optimizations.

CFD introduced the ability to couple the numerical flow solvers with optimization algorithms, building up automatic optimization environments. Such environments give the designers a chance to decrease the manual iterative work, including the trial and error missions they are engaged into, while seeking an efficient design.

A typical aerodynamic optimization loop couples four main components (the rectangular boxes) as shown in Figure 1.

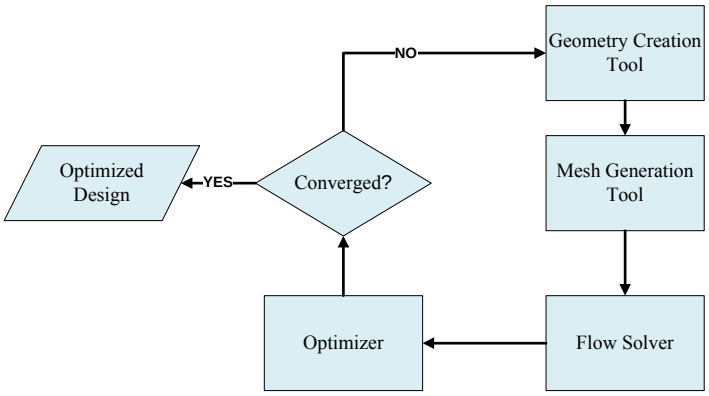

Figure 1: The main components of an Aerodynamic optimization

The optimization starts with creating the geometry using a geometry-modelling tool. Then, a mesh (grid) generation tool discretizes the computational domain around the geometry. After that, the flow solver (the third component) computes the flow state for the computational domain. Finally, the optimizer reads in the flow state and suggests new design parameters after evaluating the optimization objective under certain constrains. The new design parameters are then employed to generate the model's geometry again, in order to start a new optimization loop. The process is repeated until a given convergence criteria is satisfied. Optimization loops can be set using a scripting language that connects its components. One efficient and simple-to-use language is the Python scripting language [11].

The optimizer (also called optimization algorithm), which is the engine of the optimization process, tries mainly to solve the following problem [12]:

$$\text{Minimize } I(D) \qquad \text{subject to } \begin{cases} G(D) = 0 \\ C(D) \le 0 \end{cases} \tag{1}$$

Where I is the cost function (or objective) of the optimization, that should be minimized (or maximized), D is the vector of design parameters (or design variables), and G and C are equality and inequality constraints, respectively.

Many publications have shown studies and results of different aerodynamic optimization techniques [13,14, 15, 16, 17, 18, 19, 20]. Such publications serve as a rich database, which helps in comprehending the different components and algorithms used in optimizations, and provides best-practice knowledge.

Optimization algorithms can be mainly divided into gradient-based and gradient-free algorithms, depending on whether the gradient information is needed throughout the optimization. Deciding which optimization technique to use depends on the objective function, in addition to the number and the nature of constraints and design variables (especially in high-fidelity optimizations) involved in the problem. The application of the gradient-based techniques for problems with high number of design variables was until lately not adequately affordable; since the computational cost of the gradient scaled linearly with the number of design variables. In the late 80s, Jameson [20] applied an approach that computes the gradients independently of the design variables'

number. This approach is called, under other names, the *adjoint approach*. It stimulated the application of gradient-based algorithms in aerodynamic optimizations using high-fidelity models.

When optimizing a system whose objectives depend on several disciplines, it is necessary to include the effects of these disciplines in the optimization. Otherwise, the optimization may result in a suboptimal design, and the predicted objectives might be inaccurate, especially if the relevant disciplines are strongly coupled. Aerodynamics and structure -in aircraft design- are strongly coupled disciplines, while a change in one of them enhances a change in the other. As a response to the aerodynamic loads on a wing, for instance, the wing deforms during the flight, and this deformation affects the flow over the wing. In this case, if *LoD* is to be maximised, it is essential to consider the flow and the structural behaviour that affects the flow during the wing optimization.

1.3 Aero-Structural Effects on Aircraft Design

The jig shape of a wing is the manufacturing shape (when supported in the jig) which is not exposed to any loads, whether gravitational or aerodynamic ones. If only the gravitational loads are considered, when the aircraft is settled on the ground, the wing will have the so-called ground shape at which the wing is slightly bent downwards. The gravitational loads might then include the fuel weight. Figure 2 shows the wing shapes at different conditions. During the flight, the wing is exposed not only to gravitational loads, but also to aerodynamic loads. The wing shape under these loads is called, the flight shape. This shape varies with the fuel consumption and the flight conditions. However, the stiffer the wing, the closer these three shapes to each other.

Figure 2: Wing bending under aero-structural effects [23]

The wing deformation during flight depends on the aerodynamic loads in addition to its weight (including fuel) and stiffness; the lower the stiffness, the higher the deformation. As the wing deforms, the flow around it changes, which might affect the pressure distribution on the wing drastically [21], especially in transonic flow regimes [22]. Hence, in order to predict the flow coefficients accurately, the wing's elastic effects need to be considered.

Figure 3 shows the effect of considering the structure's elasticity while predicting the pressure over a wing [23]. The chordwise pressure distribution for a long-range jet airliner at a flight test condition is depicted for both the aerodynamic (uncoupled) and aero-structural (coupled) computations, at chosen span stations. As expected, the flight

test results have a better matching with the results of the aero-structural coupled computation, and this discrepancy between the coupled and the uncoupled computations increases towards the wingtip. This emphasizes again the necessity for considering the wing's elasticity.

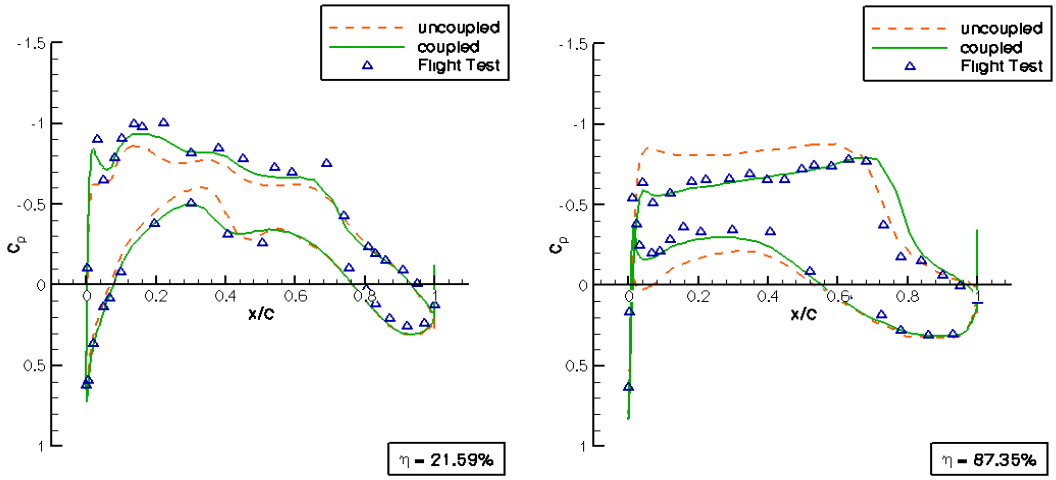

Figure 3: Comparison of pressure distributions at different sections of a transport aircraft wing, the effect of considering wing's elasticity [23]

To compute the flight shape of a wing numerically, a coupling between the flow (*CFD*) and the structure (*CSM*; computational structure mechanics) governing equations has to take place. This aero-structural coupling might be strong or loose. More details about these coupling strategies will be discussed in section 3.1.

As mentioned earlier, the efficient gradient-based optimization algorithms are required whenever the evaluation of the objective is costly and the number of the design variables is high. Considering the structural elasticity while evaluating the aerodynamic objectives can only increase the computational cost. Since the adjoint approach was proven efficient and independent of the number of design parameters, an existing flow adjoint approach will be further extended to include the structural elasticity, and afterwards, it will be applied within several MDO scenarios that employ gradient-based algorithms. In the following, a review of using the adjoint approach for coupled aero-structural problems will be presented.

1.4 Literature Review

Gradient-free optimization algorithms have been used in MDO, however, by compromising the level of model fidelity in the problem or the number of design parameters. In [24], an aero-structural optimization was performed for a wing-body configuration with high fidelity models on both the aerodynamic and the structure side. However, only six design parameters that control the wings planform were used, in order to keep the computational cost reasonable.

The use of gradient-based algorithms to optimize aero-structural problems was limited before the development of the adjoint approach. Guinta and Sobieski [25] have employed a technique that relies on the finite differences approach to compute the gradi-

ents and perform an aeroelastic optimization of a supersonic jet. The aeroelastic optimization employed a finite element code and an inviscid flow solver, the optimization turned very costly even though the flow was considered inviscid, which confirms the shortcomings of the finite differences approach in such optimizations.

The efficient adjoint approach for aeronautical *CFD* problems was first applied in 1988 by Jameson, where he demonstrated its use in aerodynamic design [20]. Before that, Pironneau applied it for potential flow problems [26]. In structure mechanics, the adjoint theory was even used earlier to perform sensitivity analysis (*SA*) by Haug et al. [27]. After becoming mature in both disciplines, the adjoint approach was employed by Martins [28] for aero-structural problems. Several studies followed the work of Martins; however, by employing low-fidelity models for at least one of the two disciplines. In the following, a summary of these studies is presented.

In the pioneer work by Martins [18,29], the adjoint approach for coupled aero-structural systems was successfully applied to optimize a proof-of-concept supersonic business jet configuration at two flight conditions with two load cases. The flow was considered inviscid; hence, he used the Euler equations to compute the flow. Furthermore, the structure finite element (FE) model was made of truss and triangular-plane-stress-plate elements with three translational degrees of freedom for each node; this means that the structure elements could not carry bending moment, since they have no rotational degrees of freedom. To be able to add the structure problem to the adjoint approach, Matrins employed some kind of constraints aggregation based on the KS (Kreiselmeier-Steinhauser) function. Such aggregation is conservative, and hence is not expected to bring reasonable mass reduction as expected on the aerodynamic side when using the adjoint approach. Nevertheless, the use of the coupled adjoint technique in this study has proven to be very efficient when compared to the traditional finite differences approach.

In other studies, Maute et al. [30] and Fazzolari [19] derived again the coupled adjoint approach for inviscid flows, however, the structural finite element model employed here shell elements with 6 degrees of freedom at its nodes, which means that the structure model could hold bending. To apply the developed formulation, Maute chose a prototype wing to increase its *LoD* ratio at a constant lift and maximum wing stress (KS constraint lumping). The optimization showed successful results. On the other hand, Fazzolari, who coupled the structured flow solver; FLOWer [31] with the commercial FE solver NASTRAN [32], performed two optimizations for a wing, one of them reduced the drag, and the other increased the flight range. In both cases, the coupled adjoint has shown higher efficiency when compared to the FD approach.

Leoviriyakit and Jameson also presented sensitivity-driven aero-structural optimizations in several papers [33, 34, 35, 36] , where the wing sections and planform were modified by the optimizer to reduce the drag and the weight of the aircraft. In some of these papers, the flow was considered viscous and the *RANS* equations were employed. However, no structural/elasticity adjoint equation was solved, and hence no coupled adjoint, since the analytical weight relation to the shape design variables was implemented within the flow adjoint solver.

Other studies that were lately performed by Martins' MDO group, handled again the coupled aero-structural adjoint approach [37, 38, 39] , they enhanced the FE model and the optimization methodology. Furthermore, they enhanced the flow model fidelity to deal with viscous flows, however, only on structured grids, which increases the obsta-

cles when complex geometries are simulated. Again, the KS constraint aggregation was used to force the adjoint approach on the structure side.

The latest study to our knowledge is done at ONERA; the French Aerospace Centre, where a sensitivity analysis for a coupled aero-structural system was performed by Marcelet [40], and an extension to the coupled adjoint approach took place by Ghazlane [41]. The approach considers viscous flows. The turbulence terms were frozen here during the flow adjoint computation, which affects the accuracy of the gradients, especially for transonic flow regimes. Furthermore, the structure is modelled using an Euler-Bernoulli beam model, thus, no high-fidelity FE model is employed.

1.5 Objective and Outline

This study aims at developing and industrializing an adjoint approach for coupled aeroelastic problems. The novelty of this work lies in developing this efficient approach and then applying it on industry-relevant problems that are represented by fully turbulent viscous *RANS* flows on the aerodynamics side and high fidelity FE models on the structure side. The contribution thereupon is mainly the industrialization of such technique, and can be summarized in differentiating the flow-structure coupling tools, and implementing and solving the coupled adjoint equations for realistic aero-structural problems. This requires extending the flow adjoint boundary condition to include the structure elasticity effect. Furthermore, the developed approach will be employed and tested on an industry-relevant case in two different optimization scenarios. The first scenario will not consider any weight constraints whereas the second one will. Both scenarios will be tested for single-point as well as multi-point design optimizations in order to demonstrate that the developed approach can be efficiently used for industrial type problems.

The implementation of the boundary condition should be done in such a way that it is irrelevant to the flow type, whether viscous or inviscid, or the turbulence effects, whether fully turbulent or viscous flows with frozen turbulence. Furthermore, it should be able, independently, to use any of the differentiated turbulence models in DLR's flow solver (Spalart- Allmaras as well as *k*-*w*).

Within the next chapters, this study attempts to present the development and the application of the coupled adjoint approach. Chapter 2 presents the gradient-based optimization techniques, and introduces the adjoint approach, showing a typical application for the aerodynamic adjoint approach.

The main contribution of this thesis starts in Chapter 3, which starts by introducing the coupling methodology used in this study. Then, it presents the development of the coupled adjoint approach. Furthermore, it zooms into the detailed formulation to show how the terms of the coupled adjoint approach were derived. After that, section 3.5 presents a validation of the gradients obtained by the coupled adjoint approach.

Chapter 4 presents a study on the basic elements engaged in the optimizations. A mesh and a design variables study followed by an optimization algorithm study will be presented in this chapter. Afterwards in Chapter 5 an industry relevant wing-body configuration is used for single-point and multi-point optimizations. Finally, chapter 6 concludes and suggests some future steps.

Chapter 2: Adjoint Approach for Aerodynamic Shape Optimization

As mentioned in the introduction of this thesis, there is no magic algorithm that suits all kinds of optimization problems. Choosing the optimization algorithm depends on the nature of the problem under consideration. The algorithms can be divided into two main groups with respect to the use of gradient information: gradient-based algorithms and gradient-free (derivative-free*)* ones. Furthermore, optimization algorithms might be divided with respect to other criteria such as constrained or unconstrained, random or deterministic, etc…. These classifications, however, are out of the scope of this thesis, and the interested reader might refer to Nocedal and Wright [12] for more information.

2.1 Optimization Algorithms

2.1.1 Gradient-Free Algorithms

The main advantages of gradient-free optimization algorithms are their ability to find global or near-global optimums [42]; they do not fall directly to local optimums the way gradient-based techniques do. Furthermore, they only require the computation of the objective value at each optimization iteration, which makes their use generally easier for the user. However, such algorithms typically need orders of magnitude more evaluations than the number of design variables, and might therefore be inefficient, in particular when high-fidelity methods are involved.

Evolutionary algorithms and the simplex-based methods (like subplex) are frequently employed gradient-free algorithms. Evolutionary algorithms inspired their mechanisms from the biological evolution and natural selection, such as survival of the fittest. These algorithms are generally slow techniques, especially when the problem contains a high number of design variables.

The subplex (Subspace-searching simplex) method was developed by Rowan [43] in 1990. It discretizes the domain space of the optimization problem into several sub-domains and then uses the simplex method suggested by Nelder and Mead [44] to minimize the objective in each sub-domain. The simplex method is frequently used to solve non-linear optimization problems where the direction of the search is determined using (N+1) objective evaluations for a problem with (N) design variables [6].

2.1.2 Gradient-Based Algorithms

The gradient of a scalar value is the vector that points in the direction of the highest rate of increase for this scalar value, where the magnitude of the vector is then the rate of increase. Figure 4 shows an example of the gradients of drag with respect to the displacement of every grid point on a wing surface. In some applications, this so-called global (linear) sensitivity map is used to perform a sensitivity analysis. Without any optimization algorithm it gives the aerodynamic shape designer a sense of orientation, how to change the geometry in order to modify a given cost function. In the example in

Figure 4, the green and blue colours indicate regions that need to be deformed outwards in order to reduce the drag over the wing, whereas the yellow and red colours depict regions that need to be deformed inwards.

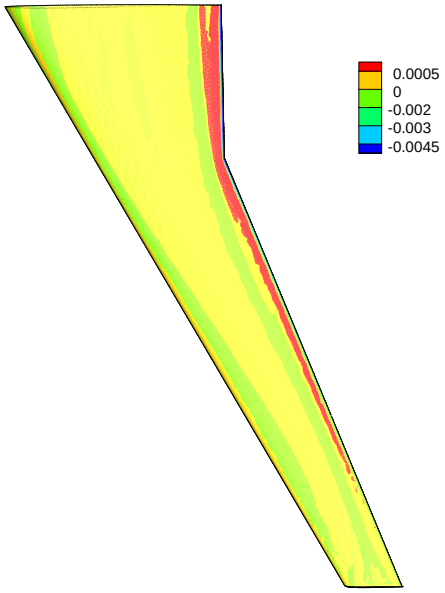

Figure 4: Global sensitivity map; drag gradients of the wing

The advantage of the gradient-based algorithms lies in their efficiency. The gradients provide the optimizer with a direction leading to a minimum, however, the closest local minimum. Other than falling for the closest local minima, gradient-based algorithms are limited by the fact that they can optimize only continuous design variables; for example, design variables that accept only integers (number of seats in an aircraft) cannot be optimized *directly* with gradient-based algorithms.

Several gradient-based algorithms are used in optimization, with the simplest being the steepest descent (SD) algorithm. In *SD* algorithm, the gradient is computed, and then the optimizer modifies the design parameters by moving a step along the negative (in case of minimization) gradient direction. There are several ways to decide the magnitude of the step; for more information about that, the reader is referred to [12]. This method is known to be simple to implement and to have low storage requirements; O(*N*) for a problem with (*N*) design variables. Nevertheless, the convergence of this technique is generally slow in real-world (poorly conditioned) applications. In [13], different aerodynamic optimizations show that this algorithm converged similarly as the Subplex algorithm for a problem with small number (only 10) of design parameters, without a valuable difference between their efficiencies.

Another gradient-based algorithm is the nonlinear conjugate-gradient (CG) algorithm. This technique was first introduced by Fletcher and Reeves [45]. The main advantage of this technique is that it does not require high storage; O(*N*), while it is a simple modification of the steepest descent approach; however, it is more efficient than the steepest descent. The reason behind that is that it includes information about the gradient, not only at the current step, but also at previous steps as well.

Other gradient–based techniques use an approximation of the Hessian, where the Hessian is the second derivative of a function. These methods are called quasi-Newton meth-

ods [46], where the Newton methods are those which use the exact Hessian information during an optimization. An example on the quasi-Newton method is the variable metric method (*VMM*) [47], which proved to be very efficient for different optimization problems [13].

Having an efficient algorithm to solve the optimization problem does not necessarily mean that the optimization will be efficient. The main efficiency obstacle in gradient-based techniques lies in computing the gradients. Several approaches to compute the gradients are available, like the finite differences approach, the complex step and the adjoint approach. In the following, the merits and shortcomings of these methods are discussed.

2.2 Gradients Computation Methods

2.2.1 The finite Differences Approach

Driven by its simplicity, this approach is the most common approach for computing the gradients. The finite difference (*FD*) schemes are obtained from the Taylor series expansions, which are truncated about a point p to derive the first derivative (gradient) of a function I with respect to a set of design variables D as illustrated in Figure 5. There are mainly three different ways to approximate the gradient at a point p using the values at p and neighbouring points in one space dimension: namely the forward, the backward (first order approximations) and the central differences (second order approximation).

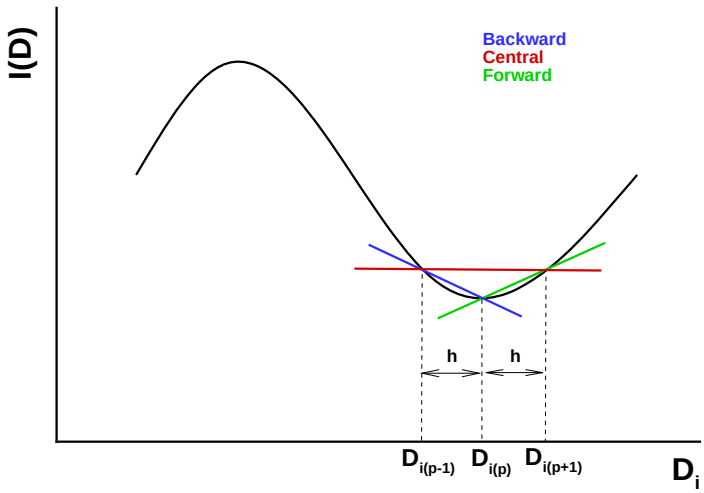

Figure 5: Gradient approximation using the finite differences approach

If the point p in addition to the point to its right $p+1$ are used to approximate the gradient of I with respect to one of the design variables D_i, then the result is a forward difference, presented in equation (2). Otherwise, if p and the point to its left $p-1$ are used, the backward difference results as in equation (3).

$$\frac{dI}{dD_i} = \frac{I(D_{i(p+1)}) - I(D_{i(p)})}{h} + O(h) \tag{2}$$

$$\frac{dI}{dD_i} = \frac{I(D_{i(p)}) - I(D_{i(p-1)})}{h} + O(h) \tag{3}$$

From equations (2) and (3) it is clear that the cost function needs to be computed at the point of interest *p*, as seen in Figure 5, and additionally at the neighbouring point *p+1* or *p-1*, in order to obtain the gradient.

To compute the gradients with respect to *N* design variables with any of these two techniques, *N+1* computations are needed. The error in the approximation will then be of the order (*h*), where *h* is the distance between the points; i.e. the step (or perturbation) size. Hence, reducing the step size *h* by a factor would reduce the error in computing the gradient by that same factor.

To decrease the error in the gradient approximation for the given step size, the central finite differences approach is employed. In this approach the information are used from both sides of point *p*, left and right that is.

$$\frac{dI}{dD_i} = \frac{I(D_{i(p+1)}) - I(D_{i(p-1)})}{2h} + O(h^2) \tag{4}$$

As seen in equation (4) the error here is of a second order. However, to compute the gradients for *N* design variables, *2N* state computations are needed.

The application of this approach is rather simple because no modification to the computational code is required. Nevertheless, computing the gradients using the *FD* approach might lead to wrong values of gradients. The step size *h* needs to be chosen so that it is small enough to reduce the error in the approximations and big enough to avoid the dominance of the subtractive cancellation errors within the approximation. This situation is the so-called step-size dilemma [18]. Therefore, for complex applications, a study has to be made for each design variable, in order to find the suitable range of steps *h* that ensure the accuracy of the gradient computation.

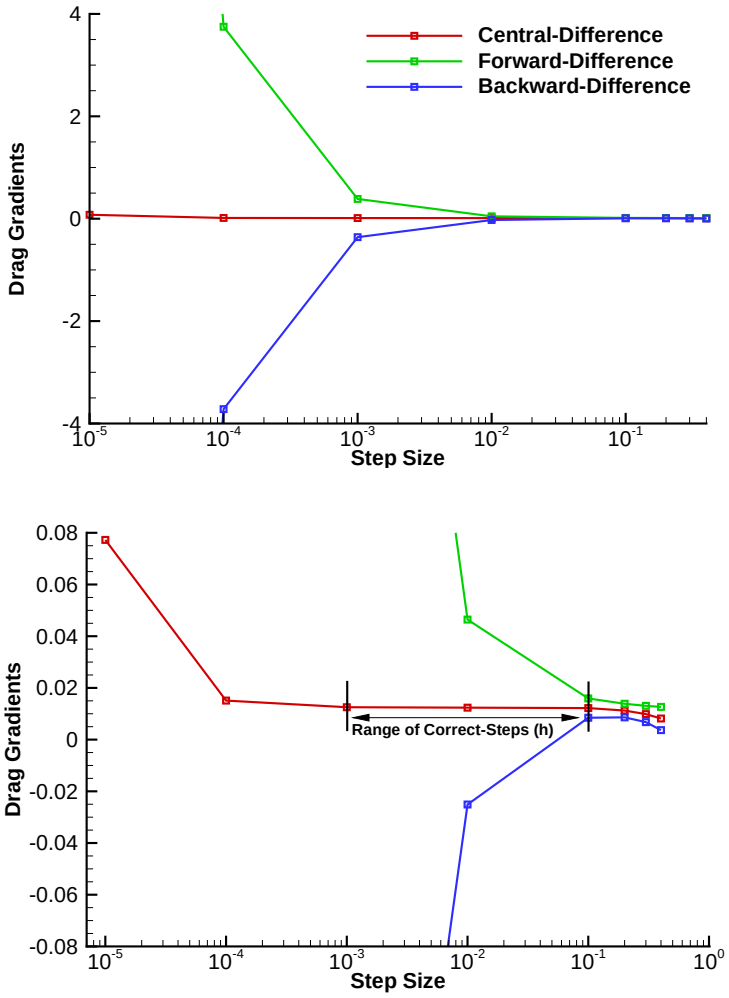

Figure 6: The effect of the step-size on the gradients (whole view & zoomed view)

As Figure 6 shows, there is usually a range of finite steps *h* that does not degrade the gradient accuracy; a range at which the computed gradient is constant. However, such study is costly and can be prohibitively expensive to perform.

The figure shows how the step-size affects the gradients quality. For this test case, which is a 3D wing-body configuration, one design variable is perturbed by different steps ($10^{-5}$to $4*10^{-1}$) and the gradients are then evaluated using the forward, the backward and the central finite differences approaches. It is clear from the figure that the central finite differences approach could produce constant gradient for a range of step values between 10^{-3} and 10^{-1}. The figure also illustrates that the forward-difference scheme approaches this constant gradient at higher steps values (0.1 to 0.4).

2.2.2 The Complex Step Approach

To eliminate the dependency of the gradient accuracy on the step size *h*, another approach can be used, namely the complex-step (*CS*) approach. Unlike the *FD* approach, the complex step approach needs to be implemented within the computational code, which, depending on the code's complexity, might be very laborious. The *CS* approach

is as accurate as the central *FD* (truncation error is $O(h^2)$), however, it requires the same computational effort as in forward or the backward finite differences. Following the derivation in Martins' study [48], the complex-step derivative approximation of a cost function I with respect to a design variable (D_i) is:

$$\frac{dI}{dD_i} = \frac{\mathrm{Im}[I(D_i + ih)]}{h} + O(h^2) \tag{5}$$

Martins compares in his study the *FD* approach with the *CS* approach for a large range of steps (10^0 to 10^{-305}), and shows how *CS* converges as the central *FD* until the subtractive cancellation errors dominate the *FD* approach (starting from 10^{-5}), where *FD* starts to diverge. The CS approach on the other hand, continues to converge adequately with a normalized error less than (10^{-15}) for the rest of the steps. However, as in the *FD*, the *CS* approach is prohibitively expensive for high-fidelity aircraft optimizations with high number of design variables since it requires $N+1$ computations to get the gradients for N design variables.

2.2.3 The Adjoint Approach

In Figure 4, where the global sensitivity map was presented, the gradient was computed at every surface mesh point. When all surface grid points are used as design parameters, we have the so-called mesh-point parameterization (sometimes also called parameter-free [49]). Here the designer will have the highest possible degree of freedom to parameterize the object of interest. In such case, if the wing has 5000 surface grid points for example, it will be unaffordable to compute the gradients using the *FD* or *CS* techniques and the computational power available today. Such a problem needs 5001 state computations to get the forward or backward difference gradients. Moreover, for higher accuracy, 10000 computations are needed by *FD*. Therefore, in such cases, while dealing with high-fidelity flow models, like the *RANS* equations, *FD* and *CS* approaches are practically out of question with the computational power available today.

In the late 1980's Jameson introduced the adjoint approach to aerodynamic problems [20], which eliminates the dependencies of the gradient computation on the number of design variables in practical terms. The formulation of the adjoint technique might be continuous or discrete. In the continuous approach, the partial differential equations (PDE) representing the flow physics are differentiated prior to discretization. On the other hand, in the discrete approach, it is the other way around; the flow equations are first discretized then differentiated.

Several studies tried to explore the advantages and disadvantages of both formulations. The main points as mentioned by Giles et al. [50] are the following: The discrete formulation of the adjoint approach provides the exact gradients, where in the continuous approach the gradients are exact only when the flow solution is smooth with no shocks, and the grid is infinitely fine. Hence, for infinitely small grids, both discrete and continuous approaches should provide equal gradients. Another advantage of the discrete approach is that the implementation of it is straightforward. On the other hand, the advantage of the continuous approach is that it does not require high memory as the discrete formulation does, where the discrete adjoint requires saving the Jacobi matrices. In this study, the discrete adjoint approach available in DLR's flow solver TAU is adopted.

2.3 Formulation of the Adjoint Approach

The adjoint approach can be introduced following two different procedures that are detailed in [50], which is an excellent reference for comprehending the adjoint technique. The first point of view considers duality and the second point of view considers the Lagrange approach. In this study, the Lagrange approach is used since it is related to the optimal control theory and hence easier to understand in this context. In the following, the derivation of the discrete adjoint approach for aerodynamic applications will be presented and employed in an aerodynamic shape optimization. Here the {} parenthesis correspond to a vector and the [ ] parenthesis correspond to a matrix, these notations will be used only in equations.

The aerodynamic optimization problem minimizes the scalar objective function $I \in \mathbb{R}$ subject to the flow equations and constraints under consideration. R_a represents the residual of the governing flow equations. This means that the designer is interested in minimizing the objective I under the physical relationships described by $R_a=0$. The objective changes when the geometry and thus the flow state variables, like pressure or temperature, change. Hence, the objective is a function of both the vector of shape design variables $A=A_i \in \mathbb{R}^N$, and the flow state variables $w(A) \in \mathbb{R}^{dw}$, where N is the number of design variables and dw is 5 times number of *CFD* grid nodes, see equation (8). Here, the dependency on A includes implicitly the dependency on the computational mesh $X_a \in \mathbb{R}^{dm}$, having dm to be three times the number of CFD nodes when following the Cartesian coordinate system. The flow governing equations are the compressible *RANS* equations, and their residual R_a is a function of A and $w(A)$ as well.

$$A = \begin{Bmatrix} A_1 \\ A_2 \\ . \\ . \\ A_N \end{Bmatrix} \tag{6}$$

The Navier-Stokes (NS) equations in 3D are written in the conservative form [51] as:

$$\frac{\partial}{\partial t} \iiint_{cv} w \; ds = - \iint_{dcv} F \; . \; n \; ds \tag{7}$$

where cv is a control volume which has an outer boundary dcv and an outer normal of n, and w, at each computational node, represents the conservative state variables vector:

$$w = \begin{Bmatrix} \rho \\ \rho u \\ \rho v \\ \rho w \\ \rho E \end{Bmatrix} \tag{8}$$

Having ρ as the density, u, v *and* w are respectively the velocities in the x, y and z directions, and E represents the specific total energy per unit mass. The flux density tensor F contains the viscous and the inviscid flux vectors in the three coordinate directions. A

detailed description of these components can be found in [52]. The *NS* equations are averaged in time and commonly a 1-equation or 2-equatrions turbulence model is employed to model the turbulence. This adds extra term(s) to *w* that correspond to turbulence. In this thesis, the 1-equation Spalart-Allmaras model was employed.

The optimization problem can be stated as follows:

$$\text{Minimize } I = I(A, w(A)) \tag{9}$$

subject to the finite volume discretization of the RANS equations:

$$R_a = R_a(A, w(A)) = 0 \tag{10}$$

The cost function and the residual are linearized (differentiated) as:

$$\left\{\frac{dI}{dA}\right\} = \left\{\frac{dI}{dA_1} \quad \frac{dI}{dA_2} \quad \cdots \quad \frac{dI}{dA_N}\right\} = \left\{\frac{\partial I}{\partial A}\right\} + \left\{\frac{\partial I}{\partial w}\right\}\left[\frac{dw}{dA}\right] \tag{11}$$

and

$$\left[\frac{dR_a}{dA}\right] = \left[\frac{\partial R_a}{\partial A}\right] + \left[\frac{\partial R_a}{\partial w}\right]\left[\frac{dw}{dA}\right] \tag{12}$$

Having R_a equal to zero for any A, means that a Lagrange function

$$L(w, A, \psi) = I + \{\psi\}^T \{R_a\} \tag{13}$$

has the same gradients as those of the cost function for all A and all ψ :

$$\left\{\frac{\partial L}{\partial A}\right\} = \left\{\frac{dI}{dA}\right\} \tag{14}$$

where (ψ), the so-called Lagrangian multiplier, holds elements which correspond to the state variable vector elements at each computational node. It is also called the adjoint field. Since this vector is multiplied by the aerodynamic residuals, which should be zero (see equation (10)), its value can be chosen freely. Equation (14) can be written as:

$$\left\{\frac{\partial L}{\partial A}\right\} = \left\{\frac{dI}{dA}\right\} + \{\psi\}^T\left[\frac{dR_a}{dA}\right] \tag{15}$$

Combining equations (11) and (12) with (15) gives:

$$\left\{\frac{\partial L}{\partial A}\right\} = \left(\left\{\frac{\partial I}{\partial A}\right\} + \left\{\frac{\partial I}{\partial w}\right\}\left[\frac{dw}{dA}\right]\right) + \{\psi\}^T\left(\left[\frac{\partial R_a}{\partial A}\right] + \left[\frac{\partial R_a}{\partial w}\right]\left[\frac{dw}{dA}\right]\right) \tag{16}$$

Now there are two ways to compute the gradients, in which it is assumed that the inverse of the flux Jacobi matrix $\partial R_a / \partial w$ exists and that there exists a unique flow solution for each set of design variables A that is encountered during optimization. The first way would be solving for (dw/dA) in equation (12)

$$\left[\frac{\partial R_a}{\partial w}\right]\left\{\frac{dw}{dA_i}\right\} = -\left\{\frac{\partial R_a}{\partial A_i}\right\} \tag{17}$$

once for every $A_i \in A$ to get the full [*dw/dA*] and setting ψ =0, and then finding $\partial L / \partial A$ to be:

$$\left\{\frac{\partial L}{\partial A}\right\} = \left\{\frac{\partial I}{\partial w}\right\}\left[\frac{dw}{dA}\right] + \left\{\frac{\partial I}{\partial A}\right\} \tag{18}$$

This is called the *direct approach*. Otherwise, equation (16) can be rearranged as:

$$\left\{\frac{\partial L}{\partial A}\right\} = \left(\left\{\frac{\partial I}{\partial A}\right\} + \{\psi\}^T\left[\frac{\partial R_a}{\partial A}\right]\right) + \left(\left\{\frac{\partial I}{\partial w}\right\} + \{\psi\}^T\left[\frac{\partial R_a}{\partial w}\right]\right)\left[\frac{dw}{dA}\right] \tag{19}$$

where ψ can be freely chosen. ψ is computed by solving:

$$\left[\frac{\partial R_a}{\partial w}\right]^T \{\psi\} = -\left\{\frac{\partial I}{\partial w}\right\}^T \tag{20}$$

in order to eliminate the expensive [*dw*/*dA*] matrix which requires a converged flow solution for each design variable A_i. Then compute $\{\partial L / \partial A\}$, (which is *dI*/*dA*) by:

$$\left\{\frac{\partial L}{\partial A}\right\} = \left\{\frac{\partial I}{\partial A}\right\} + \{\psi\}^T\left[\frac{\partial R_a}{\partial A}\right] \tag{21}$$

This approach is called the dual or the *adjoint approach*.

Which option to choose, depends on the number of cost functions, constraints and design variables. The direct approach has to be solved one time for each design variable, whereas the adjoint approach has to be solved one time for each constraint or cost function. So if the number of design variables is less than that of the constraints and cost functions, the direct approach is more efficient, otherwise the adjoint approach should be chosen. In this study, the optimization problem is of the second type; the number of the design variables -controlling the geometry- is much higher than that of the constraints and cost functions. Hence, the adjoint approach is employed.

By solving the adjoint equations, the flow adjoint field (ψ) followed by the gradients are computed as proposed by equation (21).

There are two ways to compute the gradients *dI*/*dA*, the first one is by finite differencing the two terms $\partial I / \partial A$ and $\partial R_a / \partial A$ [53] which is much cheaper than finite differencing *dI*/*dw*, and the second one is by extending this equation to include the mesh dependencies, also called metric sensitivities, and then solving a mesh adjoint equation [54]. This approach gives the exact gradients at each surface mesh point, providing the designer with the global linear sensitivity map.

With the finite differencing approach, the terms in equation (21) are approximated as:

$$\frac{\partial I}{\partial A_i} \cong \frac{I(w, A_i + \Delta A_i) - I(w, A_i)}{\Delta A_i} \tag{22}$$

and

$$\frac{\partial R_a}{\partial A_i} \cong \frac{R_a(w, A_i + \Delta A_i) - R_a(w, A_i)}{\Delta A_i} \tag{23}$$

and then the gradients of the cost function are computed using equation (21). To use this approach (for computing $\partial I/\partial A$ and $\partial R_a/\partial A$) without *degrading* the advantages of the efficient adjoint approach, an efficient mesh deformation tool is required to perform the deformations presented in (22) and (23) in a time comparable to the time required to solve the adjoint equation. Dwight [53] has shown that this approach is accurate and efficient.

In the mesh deformation approach, on the other hand, a mesh deformation residual (R_m):

$$\{R_m(\tau,\sigma)\} = 0 \tag{24}$$

is added to the Lagrange formulation, where τ is the unknown volume deformation whereas σ is the known surface deformation. The Lagrange function then becomes:

$$L = I(w, X_a, A) + \{\psi\}^T \{R_a(w, X_a, A)\} + \{\psi_m\}^T \{R_m(X_a, A)\} \tag{25}$$

where ψ_m is the mesh adjoint field and X_a is the computational mesh. By deriving and arranging the terms, we get:

$$\begin{aligned}\left\{\frac{\partial L}{\partial A}\right\} = &\left(\left\{\frac{\partial I}{\partial A}\right\} + \{\psi\}^T\left[\frac{\partial R_a}{\partial A}\right] + \{\psi_m\}^T\left[\frac{\partial R_m}{\partial \sigma}\right]\left[\frac{\partial \sigma}{\partial A}\right]\right)\\ &+\left(\left\{\frac{\partial I}{\partial w}\right\} + \{\psi\}^T\left[\frac{\partial R_a}{\partial w}\right]\right)\left[\frac{dw}{dA}\right]\\ &+\left(\left\{\frac{\partial I}{\partial X_a}\right\} + \{\psi\}^T\left[\frac{\partial R_a}{\partial X_a}\right] + \{\psi_m\}^T\left[\frac{\partial R_m}{\partial \tau}\right]\right)\left[\frac{dX_a}{dA}\right]\end{aligned} \tag{26}$$

After solving for (ψ) in

$$\left\{\frac{\partial I}{\partial w}\right\} + \{\psi\}^T\left[\frac{\partial R_a}{\partial w}\right] = 0 \tag{27}$$

which is the second term of the right hand side in equation (26), The mesh adjoint field ψ_m is computed by solving

$$\left\{\frac{\partial I}{\partial X_a}\right\} + \{\psi\}^T\left[\frac{\partial R_a}{\partial X_a}\right] + \{\psi_m\}^T\left[\frac{\partial R_m}{\partial \tau}\right] = 0 \tag{28}$$

Then the gradient of the cost function is computed by taking the rest of equation (26):

$$\left\{\frac{dI}{dA}\right\} = \left\{\frac{\partial I}{\partial A}\right\} + \{\psi\}^T\left[\frac{\partial R_a}{\partial A}\right] + \{\psi_m\}^T\left[\frac{\partial R_m}{\partial \sigma}\right]\left[\frac{\partial \sigma}{\partial A}\right] \tag{29}$$

Which option to choose here in order to determine the mesh effects (whether finite differencing or mesh-adjoint) depends on the parameterization used in the optimization. The mesh adjoint requires solving a linear system in equation (28) in addition to computing the term $\partial\sigma/\partial$A, whereas the finite differencing requires deforming each control point (twice for more accuracy), which can be performed in parallel. Hence, if the mesh-point parameterization is used or a control point parameterization with differentiated relation to the surface mesh points (the sensitivity of the mesh points to parameteri-

zation is available), then it makes sense to use the mesh-adjoint extension. Otherwise, the finite differencing approach should be as efficient and as accurate, especially if the central finite differencing is used. However, the right step-sizes for the finite differences have to be found, which might be time consuming sometimes.

After computing the gradients, they are passed together with the objective and constraint values to the optimizer to predict the new design variables.

2.3.1 The Adjoint Approach in TAU

In DLR's flow solver TAU, the discrete adjoint approach was implemented and tested for different aerodynamic optimization problems [55]. It is implemented for inviscid as well as viscous (*RANS*) flows where the one-equation Spalart-Allmaras and the two-equation *k-w* turbulence models are linearized. To solve the linear adjoint equations, and compute the Lagrangian multiplier, TAU might employ one out of three options. The first approach uses an iterative solver implemented in TAU [13]. The second one uses the open-source external linear solver package PETSc [56], to which interfaces were implemented in TAU. Furthermore, the third option employs the lately implemented linear solver package (SAMG) [57] which is showing excellent results.

The computational effort needed for solving the adjoint equations and the flow equations is of the same order. This is the case at least with the linear iterative solver. With PETSc or SAMG, it is remarked that the time required to solve the flow adjoint tends to be much less in 3D viscous cases.

The mesh adjoint approach was recently implemented in TAU as presented in Nielsen's study [58] and then applied successfully to optimize a viscous 2D airfoil and the 3D inviscid Onera-M6 wing [54]. The deformation (R_m) is represented by the linear elasticity PDE.

2.4 Application of the Discrete Adjoint Approach for Aerodynamic Shape Optimization

Before including the structure in the adjoint approach, it makes sense at this point to test the efficiency and the reliability of the flow adjoint approach, which is implemented in DLR's flow solver TAU. This study will use the gradient-based nonlinear *CG* algorithm as an optimizer. The gradients of the design parameters are computed using the discrete adjoint approach. The objective of the optimization is to reduce the drag at constant lift and wing thickness for a wing-body configuration that is based on the regional jet Dornier-728 geometry. This configuration was used in the frame of an internal DLR project called MDOrmec [59], which was concerned with performing MDO for a rear mounted engine configuration. For this reason, and to simplify the nomenclature in this thesis, the configuration will be called the MDOrmec configuration here.

To control the geometry, the free form deformation (*FFD*) [60] technique is employed. In this technique, a box of control points is set around the objects of interest, where the geometry deforms in accordance to the movement of the control points (design parameters).

Figure 7 illustrates an example on *FFD*. The Onera-M6 wing here is controlled by 60 *FFD* control points (design parameters). As the two nodes on the leading edge move (their new position in red), the wing deforms correspondingly.

Figure 8 shows the MDOrmec configuration with the *FFD* design parameters. As illustrated, 110 *FFD* design parameters are controlling the clean wing-body configuration. The wing *FFD* parameters (in blue) are used in a way that keeps the wing thickness constant. Here, only the upper group of *FFD* points (40 points) are allowed to move freely, and the adjacent lower ones follow them with the same deformation suggested by the optimizer. This implicitly keeps the thickness of the wing-box constant. The *FFD* parameters on the fuselage (in red) are fixed so that its geometry stays constant while being able to change the intersection line between the wing and the fuselage slightly using the wing *FFD* box as illustrated in Figure 8 (bottom at wing root).

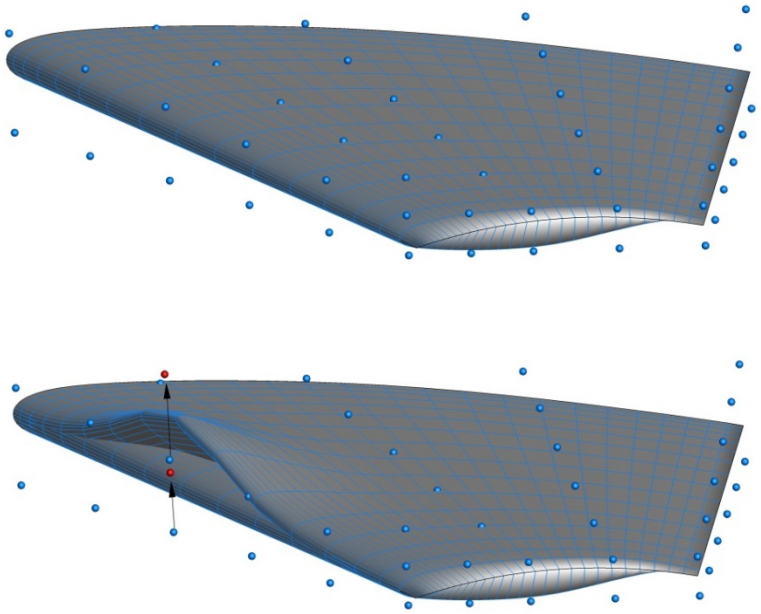

Figure 7: Freeform-Deformation parameterization of an ONERA M6 wing

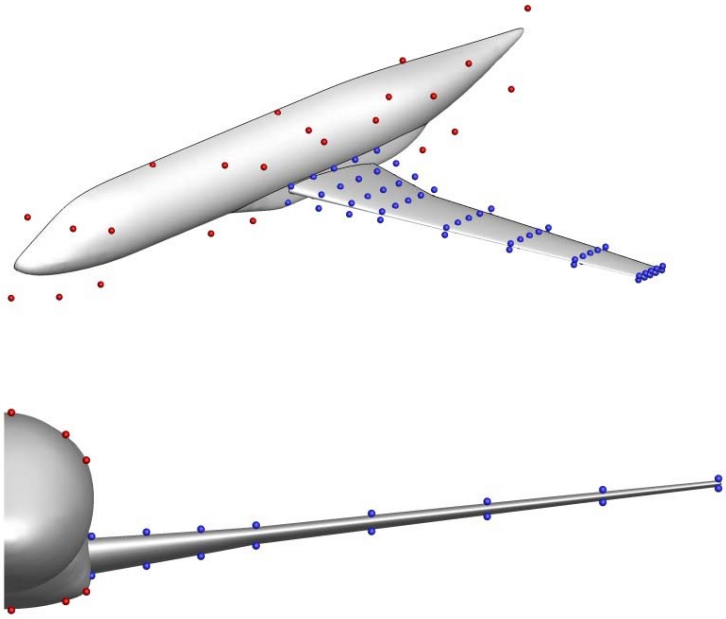

Figure 8: *FFD* parameterization on a wing-body configuration

The *FFD* technique here is applied directly on the surface mesh using an efficient mesh deformation tool. This means that there will be no need to include CAD in the loop; such optimizations are said to be CAD-free, as in the block diagram shown in Figure 9, which does not include a CAD generation tool as explained earlier (in Figure 1)

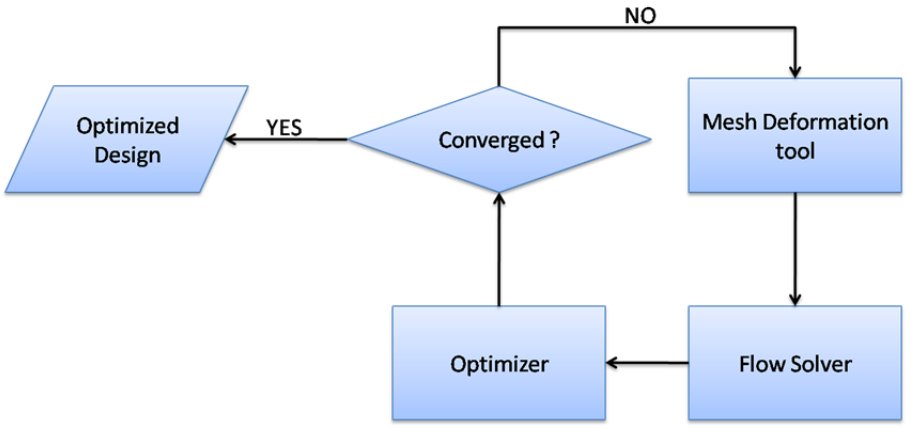

Figure 9: Components of an aerodynamic shape optimization

No mesh study was performed at this stage, since the aim here is to test the optimization architecture that will be employed later. Furthermore, a good mesh for an aerodynamic computation is not necessarily good for an aero-elastic computation because the later includes mesh deformations that correspond to the wing bending. Therefore, before spending much effort on a mesh study, an unstructured hybrid mesh that is generated using CENTAUR [61] mesh generator is employed. The unstructured mesh contains 1.7 million nodes; 59 thousand of them are surface nodes, see Figure 10 for the surface mesh.

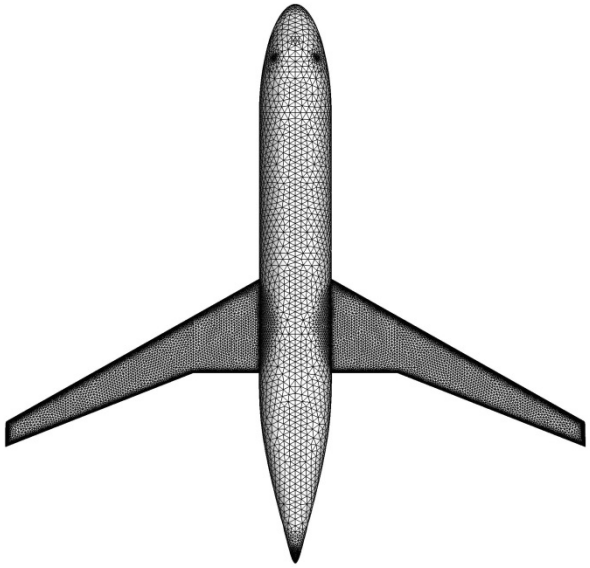

Figure 10: MDOrmec unstructured surface grid

The lift of the configuration is implicitly kept constant at a target value C_L = 0.55, by automatically adapting the angle of attack α during the flow solution. The Mach and Reynolds numbers are set to 0.8 and $21*10^6$ respectively. The one-equation Spalart-Allmaras (*SA*) [62] model is employed to model turbulence. Before starting with the optimization, the adjoint gradients are validated against the central FD gradients.

To compute the gradients of the drag at constant lift, the following relations should hold:

$$\begin{aligned} &\text{Minimize } C_D(w, A, \alpha) \\ &\text{such that } \begin{cases} R_a(w, A, \alpha) = 0 \\ C_L(w, A, \alpha) = C_L^{\text{Target}} \end{cases} \end{aligned} \tag{30}$$

And since the target C_L is kept by adjusting α , any change in the design variables which would change C_L results in a change in α to bring C_L back to its target value. This means that.

$$\alpha = \alpha(A) \tag{31}$$

The gradient of C_D at constant lift is then:

$$\left\{\frac{dC_D}{dA}\right\} = \left\{\frac{dC_D}{dA}\right\}_{\text{at fixed }\alpha} + \frac{\partial C_D}{\partial \alpha}\left\{\frac{d\alpha}{dA}\right\} \tag{32}$$

Where $\left\{\frac{dC_D}{dA}\right\}_{\text{at fixed }\alpha}$ contains implicitly the dependency on the flow state *w* that's present in (30). The gradient of C_L is:

$$\left\{\frac{dC_L}{dA}\right\} = \left\{\frac{dC_L}{dA}\right\}_{\text{at fixed }\alpha} + \frac{\partial C_L}{\partial \alpha}\left\{\frac{d\alpha}{dA}\right\} = 0 \tag{33}$$

which is equal to zero since C_L is to be kept at its target value. Again (33) states that any change of C_L due to change in design variables is opposed by a counter change via the angle of attack α , from which it can be concluded that:

$$\left\{\frac{d\alpha}{dA}\right\} = -\frac{\{dC_L / dA\}_{\text{at fixed }\alpha}}{\partial \mathrm{C_L} / \partial \alpha} \tag{34}$$

Assuming that

$$\frac{\partial C_L}{\partial \alpha} \neq 0 \tag{35}$$

which holds for cases of practical interest, such as cruise flight where $\frac{\partial C_L}{\partial \alpha} > 0$.

Inserting the term ($d\alpha /dA$) from (34) into equation (32), gives

$$\left\{\frac{dC_D}{dA}\right\} = \left\{\frac{dC_D}{dA}\right\}_{\text{at fixed }\alpha} - \frac{\partial C_D / \partial \alpha}{\partial C_L / \partial \alpha}\left\{\frac{dC_L}{dA}\right\}_{\text{at fixed }\alpha} \tag{36}$$

To compute the terms dC_D / dA and dC_L / dA, both at constant α , which are the gradients of drag and lift coefficients with respect to the design variables, two flow adjoint computations are required; one for drag and one for lift. The terms $\partial C_D / \partial \alpha$ and $\partial C_L / \partial \alpha$ are already differentiated per hand, and implemented in the TAU solver; they are provided at the end of the corresponding adjoint computations.

Moreover, to compute the gradients with the central finite differences, the two flow computations with target lift are performed for each design variable. The gradient validation result is illustrated in Figure 11, where only 10 design variables (out of 40) were tested due to the high expenses such validation requires as explained earlier in section 2.2.1. Nevertheless, the design variables were chosen at different locations over the wing; i.e. leading edge to trailing edge, and wing root to wing tip. The first 5 design variables are close to the wing root whereas last 5 are close to the wing tip. Each 5 design variables were distributed equally along the airfoil's chord; from the leading edge to the trailing edge.

The figure shows a very good matching between the adjoint gradients and the central finite differences gradients. To emphasize the advantages the adjoint approach, it is worth mentioning here that the time needed to compute the gradients for these 10 design variables with the adjoint approach is around 14% of that needed by the finite differences approach, having more design variables can only decrease this ratio.

The optimization environment used to solve the optimization problem is Pyrahna [13], which is a Python-based environment developed at DLR. The nonlinear *CG* algorithm implemented in Pyrahna is utilized for the optimization. Figure 12 shows the convergence history of the aerodynamic shape optimization. As presented, the optimization converged after 35 flow computations and 11 gradient computations. The drag was reduced by around 85 drag counts (0.0085 of C_D) which is around 20% of the initial drag,

at a constant lift and wing thickness. The optimization needed around 50 hours on 96 processing cores to converge.

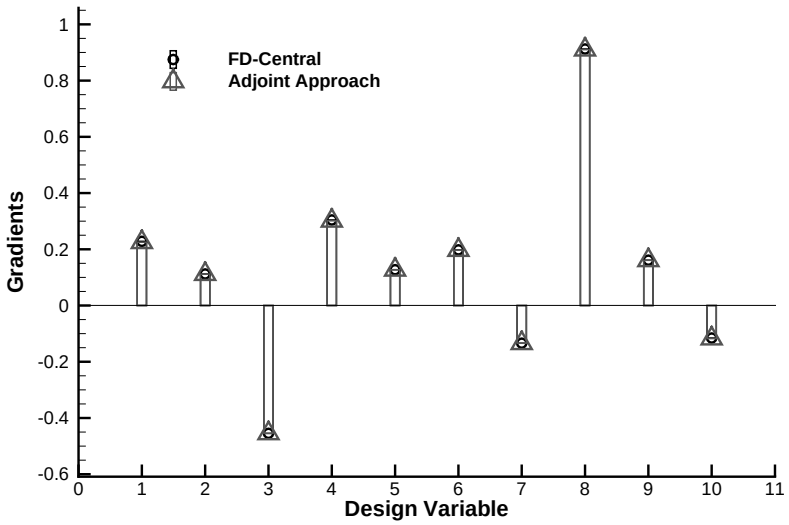

Figure 11: Gradients validation for drag at constant lift

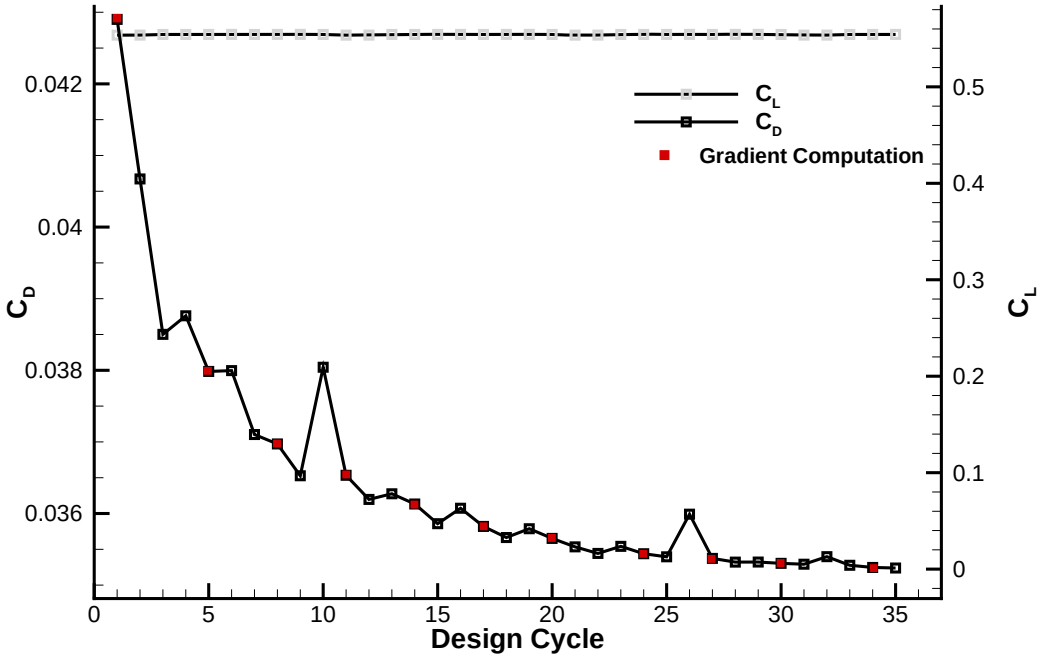

Figure 12: Convergence history of the aerodynamic shape optimization

The chordwise pressure and the spanwise loads distribution over the initial and the optimized wings are presented in Figure 13 and Figure 14, respectively.

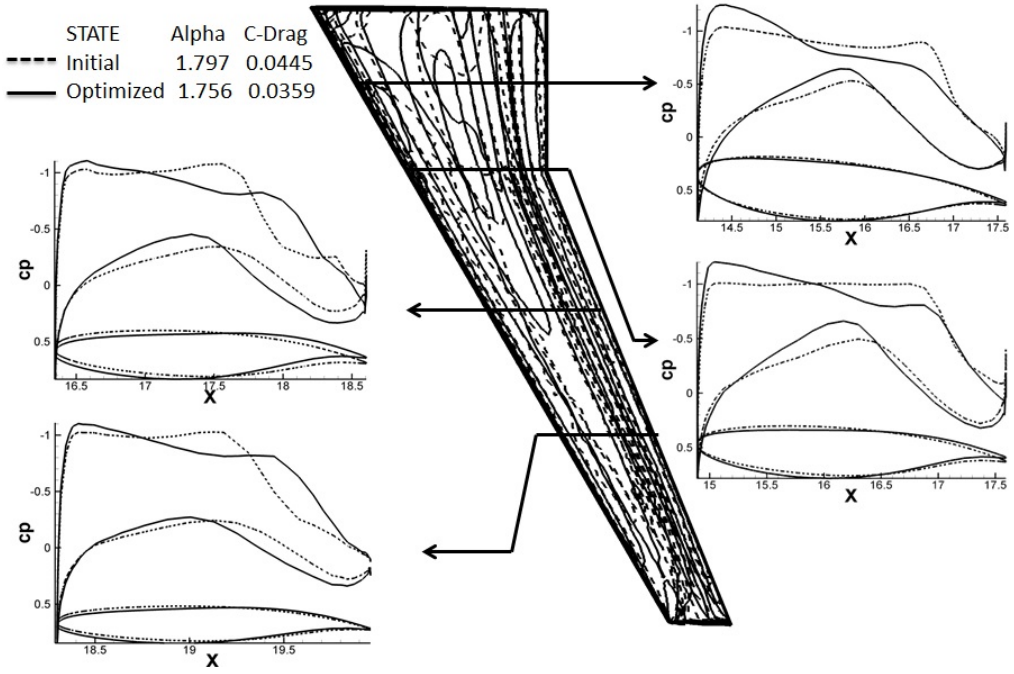

Figure 13: Aerodynamic optimization results; chordwise C_p distribution

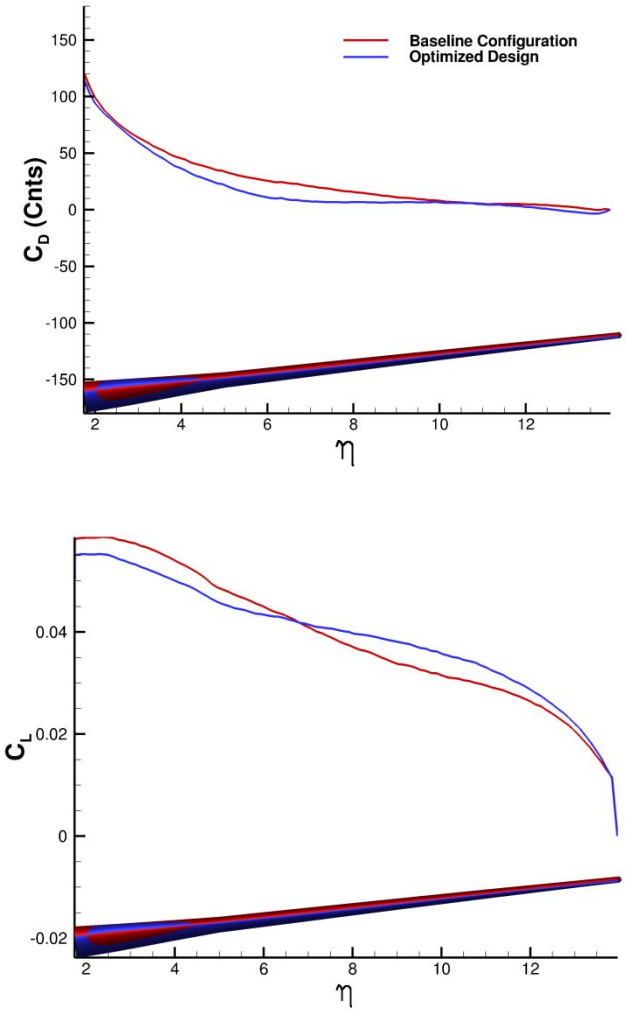

Figure 14: Aerodynamic optimization, spanwise drag (up) and lift (bottom) distributions

As shown in Figure 13, the shock on the MDOrmec wing is reduced, and the angle of attack changed only slightly by a 0.042 degrees. Figure 14 shows that the spanwise drag is reduced over the wingspan. Furthermore, the lift distribution became more elliptical for the optimized design, which implies a reduction in the induced drag. Nevertheless, such loading increases the bending moment at the wing root, which tends to increase the structural mass. This result is expected from a pure aerodynamic optimization. It shows that aero-elastic effects need to be considered.

Moreover, the optimization demonstrated that the optimization process is working correctly, and can be further used for the next steps in this study.

Chapter 3: Adjoint formulation for Coupled Aero-Elastic Systems

This study is concerned with developing and applying the adjoint approach for aero-structural systems. The aim of considering the wing structure here is to predict the aero-dynamic forces accurately during the flight.

To introduce this chapter, the method to compute the flight shape of a wing will be presented, and the components of the aero-structural coupling loop will be revealed. After that, the adjoint formulation of coupled aero-structural systems will be derived together with a detailed look at each term in this formulation. At the end of this chapter, the gradients computed with the coupled adjoint approach are validated in order to assess the implementation of this system of equations.

3.1 Aero-Structural Problems

At each flight condition, the wing is subject to different bending associated with different twist due to the aerodynamic loads. These bending-twist effects might change the aerodynamic behaviour over the wing, influencing the wing drag or lift for example. For this reason, it was common practice in the past to limit the effects of aero-elasticity by designing stiffer wings [63]; however, this requires increasing of the wing structural weight, which directly decreases the efficiency of the aircraft.

Another technique consists in designing the wing structure so that it deforms into its intended design shape in cruise flight [64]. In this approach, the optimum shape is obtained by a pure aerodynamic optimization, and then the jig-shape, is obtained by subtracting the wing deflection under cruise load from the optimum flight shape. Several couplings between the structural optimisation and the deformation are mandatory to retrieve the desired cruise shape. Details about this approach can be found in Mavris's study [65]

The main advantage of this technique is the ability to decouple the complex aero-elastic system into separate aerodynamic and structural problems. However, there is no guarantee this approach should converge for the optimal design, where the main driver here is the designers experience [66]. Furthermore, this technique is not likely to work for multi-point designs, where the wing is designed at multiple flight conditions. A good example for that is the multi-point optimization of a supersonic jet mentioned in Vazquez's study [64], where the aero-elastic behaviour is different in supersonic and subsonic flow regimes.

A third approach to deal with elasticity during the design process is to consider the flow and the structure simultaneously. Here, the flight shape is computed from the jig-shape by coupling the flow solver with the structure solver. This means of course that additional effort is required for coupling the solvers and for computing each time the flight shape from the jig shape. Nevertheless, with this approach it is possible to consider multi-point design.

3.1.1 Components of the Aero-Structural Coupling Loop

The aero-structural coupling might be strong or weak (loose) [67]. In the strong coupling environment, the flow and the structural equations are solved simultaneously; this means that one system of equations, that represents both disciplines, has to be constructed. In this system, the boundary conditions at the interface between the two disciplines have to be taken into account, which makes the implementation more challenging.

On the other hand, in the loose-coupling environment the different disciplines are treated separately. The flow and the structural equations are computed separately while the information between the two disciplines is exchanged. This iterative process is performed several times until the exchanged information (also called coupling variables) does not change anymore. This "partitioning" approach was introduced by Park and Felippa [68]. The loose coupling approach is easier to implement than the strong coupling approach. At DLR, a loose-coupling environment is available [69] and will be used in this study. The loop is presented in Figure 15.

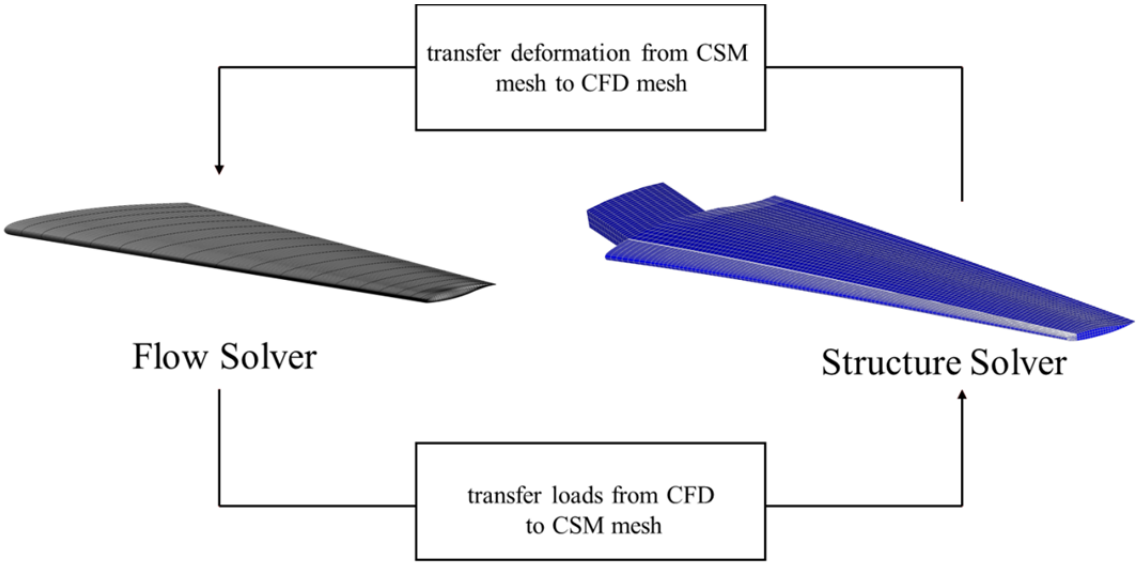

Figure 15: Components of the Aero-Structural Coupling Loop

In the loose-coupling loop, as the figure illustrates, two grids are employed; a *CFD* grid (to the left) and a computational structure mechanics (*CSM*) grid (to the right). The loop includes four main steps; two disciplinary steps that produce the interpolation variables and two interdisciplinary mapping steps that interpolate these variables from one discipline to the other. The loop starts by solving the flow equations for the *CFD* mesh, using a flow solver, which in this study will be TAU. Then the pressure computed over the wing is transferred and interpolated as loads on the *CSM* mesh using a linear interpolation tool. Now, the *CSM* mesh is loaded and ready to be solved by the structure solver, which is ANSYS Mechanical in this case. Ansys solves the linear structural problem and computes the deformations at each *CSM* node. The deformations are written out and then interpolated back to the *CFD* mesh using a volume-spline based radial-basis-function (*RBF*) interpolation tool [70]. Afterwards, the *CFD* mesh is deformed using the grid deformation tool available in TAU, and with this step, the first coupling loop is completed.

The second coupling loop starts by computing the flow state variables over the deformed *CFD* mesh, then the same steps take place again, as seen in Figure 16

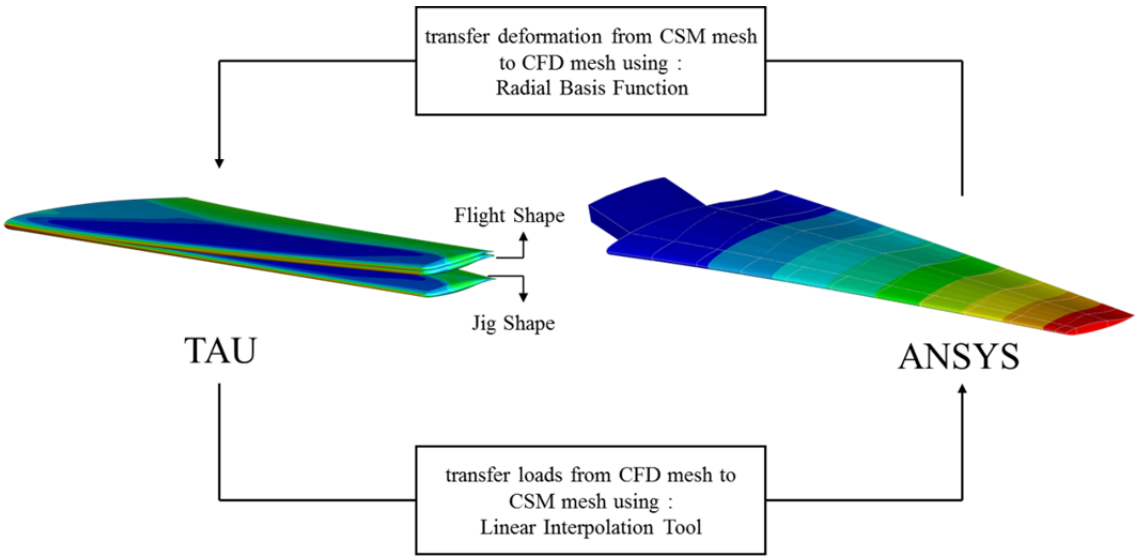

Figure 16: Converged Aero-Structual Coupling

The loop is repeated several times until the deformation and the loads, (their contour is shown in the figure) do not change anymore, i.e. converge. At this point, the aerodynamic coefficients and consequently the structural deformations become constant. In this way, it is possible to compute the flight shape from a jig shape of a wing with a specific stiffness under a defined flight condition. Practically, 5 to 10 coupling loops are required in order to achieve a converged coupling process and to compute the flight shape.

3.1.2 Convergence of the Coupling Process

The different nature of the governing equations on the structure and the flow sides lead to different solution strategies. The nonlinear governing flow equations require a certain level of accuracy and a relatively fine grid, where for the structure linear equations are used to model the expected small deformations adequately. Hence, the solution of the structural problem takes several seconds on one processor, while the solution of the flow equations might take several hours on a large number of processors. For this reason, it makes no sense for practical applications to converge the costly flow equation in each coupling loop completely. The convergence of both disciplines should be guaranteed only at the end of the coupling process.

Figure 17 shows a typical flow convergence history for a coupled flow-structure computation for a wing-body configuration. As seen in the figure, the structural displacement is updated several times, and the system is considered converged when the difference in drag is less than 0.1 drag counts between two couplings, which is the case here. On the structure side, the system is considered to have converged when the structure deformations over two consequent couplings is less than a prescribed tolerance (here 10 mm at the wingtip); Figure 17 and Figure 18.

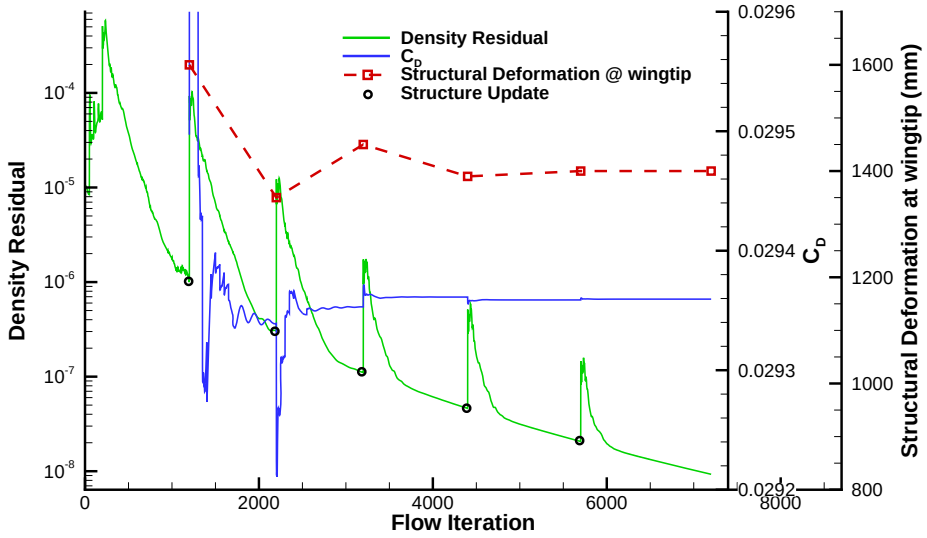

Figure 17: Convergence of the aero-structural coupling

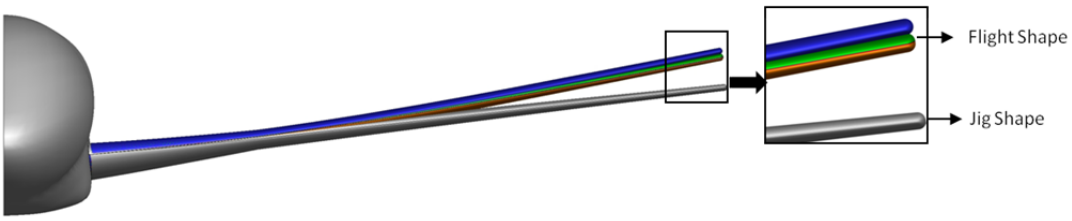

Figure 18: Wing shapes after the coupling steps

3.1.3 Aero-Elastic Analysis of Backward-Swept Wings

The aim of this section is to present the physical aerodynamic and structural behavior of the wing in its flight shape in comparison to its un-deformed shape. Here, the results of the aero-structural coupling performed in the previous subsection will be presented. The following is generally valid for backward-swept wings.

The flexural line of a wing is the axis that connects the flexural centers of each cross section of the wing, where a flexural center of a cross section is a point at which a force can be applied without producing rotation in that section [71]. This means, if a line load is applied at the flexural axis of a wing, the wing will bend without twisting (Figure 19).

The locus of aerodynamic centers for a wing usually does not coincide with the flexural axis. Therefore, as the wing becomes subject to the aerodynamic loads, the wing bends and twists. A backward-swept wing twists in a way such that the line AB, which is perpendicular to the flexural axis (Figure 19), rather than the line AC (in flow direction), has the same bending. This means, the point *C* has higher bending than point A, since it (C) is closer to the wing tip than point B. Hence, as a backward-swept wing flies, it gets a nose-down twist. This, in turn, results usually in a lower suction peak and an upstream shifting of the shock position [23] in comparison to the flow over an un-deformed wing.

Figure 20 presents the twist and the bending of the wing jig and flight shapes. The chordwise C_p distribution near the wing tip is illustrated in Figure 21.

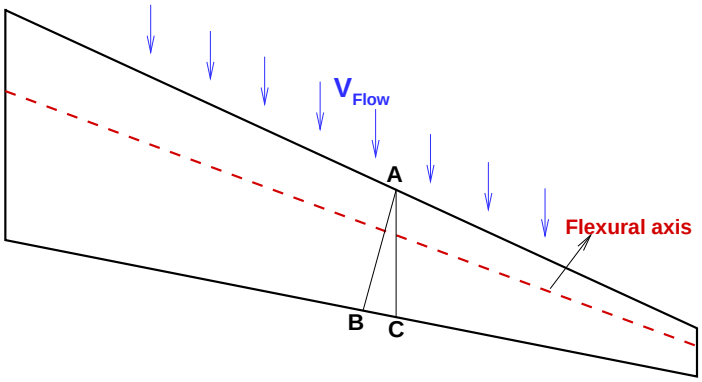

Figure 19: Flexural axis of a backward-swept wing

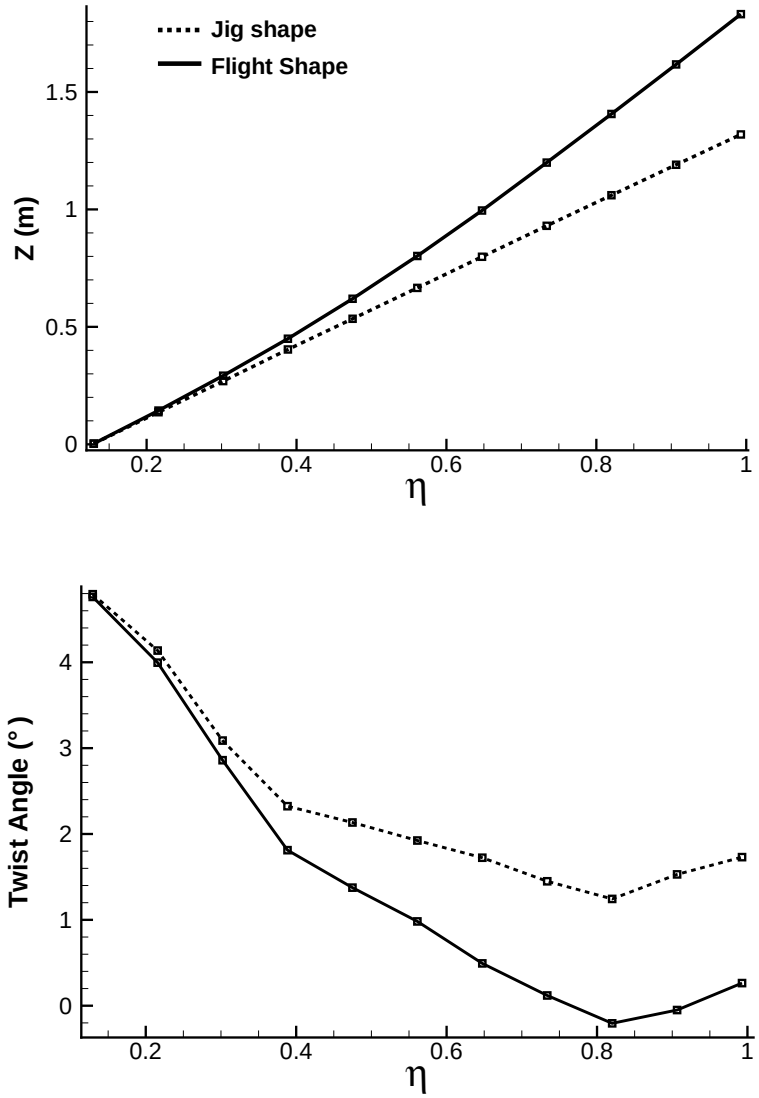

Figure 20: Comparison of bending and twist for the jig and flight wing shapes

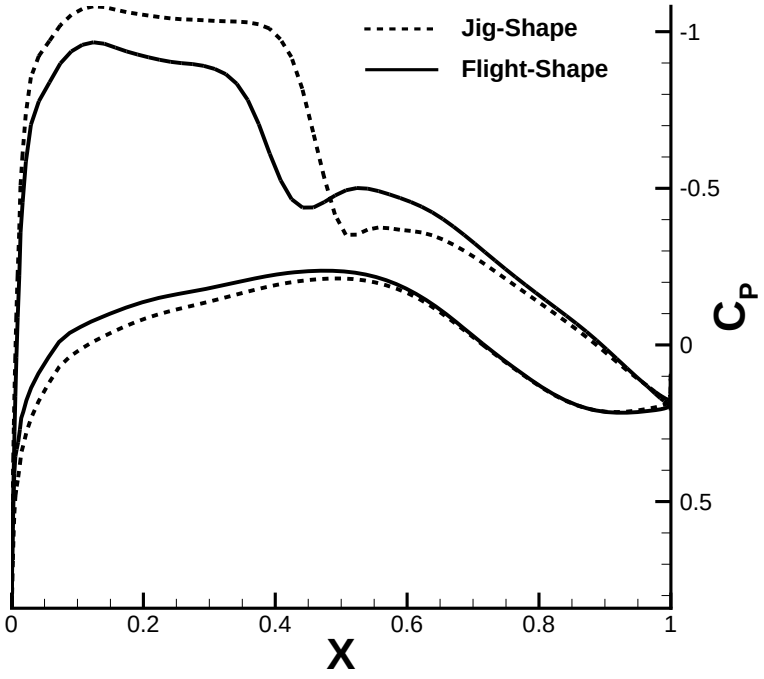

Figure 21: C_p at a section close to wing tip (η=0.9)

3.2 Derivation of the Coupled Aero-Structural Adjoint

In section 2.3, the discrete flow adjoint implemented in DLR's TAU was presented. Building on that formulation, the coupled aero-structural adjoint approach will be further developed here to include the structure elasticity effects.

The optimization problem in this study, as shown in eq. (37), is concerned with minimizing a scalar cost function I for a set of design variables D. The optimization runs under the equality constraints represented by the residuals of both disciplines R; namely the residual of the *RANS* equations governing the flow R_a and the residual of the linear elasticity equation governing the structure R_s; eq. (38). The objective function contains aerodynamic terms only; however, the effect of the wing elasticity will be taken into account to ensure that the aerodynamic coefficients are predicted accurately.

$$\text{Minimize I } (W(D),D); \qquad \text{Subject to } R(W(\text{D}), \text{D}) = 0 \tag{37}$$

Where W is the set of state variables of the coupled system, and it includes the flow state variables w and the structure state variables u which is the structural deformation. The design variables vector D includes the aerodynamic shape design variables A and the structure design variables T like the structure thickness. A vector representation of the mentioned elements that define the coupled aero-structure system is presented by equations (38)-(40).

$$\text{The residual vector of the coupled system } R = \begin{Bmatrix} R_a \\ R_s \end{Bmatrix} \tag{38}$$

$$\text{The state variables of the coupled system } W = \begin{Bmatrix} w \\ u \end{Bmatrix} \tag{39}$$

$$\text{The design variables of the coupled system } D = \begin{Bmatrix} A \\ T \end{Bmatrix} \tag{40}$$

It is worth mentioning here that the structural residual R_s follows the linear elasticity equation:

$$\{R_s\} = \{F\} - [K]\ \{u\} \tag{41}$$

where F represents the loads on the *CSM* model including the aerodynamic loads and the structural weight, K is the finite element stiffness matrix of the structure model, and u is, as previously mentioned, the structural displacement at each *CSM* node.

As (37) shows, both the cost function and the residuals are functions of the state variables and the design variables. Considering these dependencies, the gradient of the cost function with respect to the design variables becomes:

$$\begin{Bmatrix} \frac{dI}{dD} \end{Bmatrix} = \begin{Bmatrix} \frac{dI}{dA} & \frac{dI}{dT} \end{Bmatrix} = \begin{Bmatrix} \frac{\partial I}{\partial A} & \frac{\partial I}{\partial T} \end{Bmatrix} + \begin{Bmatrix} \frac{\partial I}{\partial w} & \frac{\partial I}{\partial u} \end{Bmatrix} \begin{bmatrix} \frac{\partial w}{\partial A} & \frac{\partial w}{\partial T} \\ \frac{\partial u}{\partial A} & \frac{\partial u}{\partial T} \end{bmatrix} \tag{42}$$

Having the same dependencies, the same form is taken for the gradient of the flow (43) and structure residuals (44) with respect to the design variables.

$$\begin{bmatrix} \frac{dR_a}{dD} \end{bmatrix} = \begin{bmatrix} \frac{dR_a}{dA} & \frac{dR_a}{dT} \end{bmatrix} = \begin{bmatrix} \frac{\partial R_a}{\partial A} & \frac{\partial R_a}{\partial T} \end{bmatrix} + \begin{bmatrix} \frac{\partial R_a}{\partial w} & \frac{\partial R_a}{\partial u} \end{bmatrix} \begin{bmatrix} \frac{\partial w}{\partial A} & \frac{\partial w}{\partial T} \\ \frac{\partial u}{\partial A} & \frac{\partial u}{\partial T} \end{bmatrix} \tag{43}$$

$$\begin{bmatrix} \frac{dR_s}{dD} \end{bmatrix} = \begin{bmatrix} \frac{dR_s}{dA} & \frac{dR_s}{dT} \end{bmatrix} = \begin{bmatrix} \frac{\partial R_s}{\partial A} & \frac{\partial R_s}{\partial T} \end{bmatrix} + \begin{bmatrix} \frac{\partial R_s}{\partial w} & \frac{\partial R_s}{\partial u} \end{bmatrix} \begin{bmatrix} \frac{\partial w}{\partial A} & \frac{\partial w}{\partial T} \\ \frac{\partial u}{\partial A} & \frac{\partial u}{\partial T} \end{bmatrix} \tag{44}$$

As in the single discipline adjoint formulation, the Lagrange approach will be adopted to formulate the coupled aero-elastic adjoint. The Lagrange function L here is defined as the following:

$$L = I + \{\psi\}^T \{R\} = I + \{\psi_a\}^T \{R_a\} + \{\psi_s\}^T \{R_s\} \tag{45}$$

where the Lagrange multiplier ψ includes for the coupled aero-elastic system an aerodynamic adjoint field ψ_a and a structure adjoint field ψ_s

$$\psi = \begin{Bmatrix} \psi_a \\ \psi_s \end{Bmatrix} \tag{46}$$

The aerodynamic adjoint field ψ_a has five components at each grid node in the inviscid Euler case or laminar Navier-Stokes case; each component corresponds to a flow state variable. When turbulence is considered, a sixth component, that represents the adjoint counterpart for turbulent variable, is added. This applies in case a one-equation turbulence model is used. In case of *k*-*w* two-equation turbulence model, two additional components (sixth and seventh) are considered; one corresponds to the *k*-equation and one corresponds to the *w*-equation counterparts. On the other hand, the structural adjoint field ψ_s has as many components as the number of degrees of freedom for each grid node. In this study, the FE model used has six degrees of freedom for each node; three translational and three rotational, hence ψ_s contains six components at each grid node.

Since the residual *R* is zero for any set of design variables *D*, the gradient of the Lagrange function with respect to the design variables is equal to the gradient of the cost function with respect to the design variables, which is the gradient required by the optimizer. Considering all the presented dependencies, the gradient of Lagrange function becomes:

$$\begin{aligned} \begin{Bmatrix} \frac{dI}{dD} \end{Bmatrix} = \begin{Bmatrix} \frac{\partial L}{\partial D} \end{Bmatrix} = & \left(\begin{Bmatrix} \frac{\partial I}{\partial A} & \frac{\partial I}{\partial T} \end{Bmatrix} + \begin{Bmatrix} \frac{\partial I}{\partial w} & \frac{\partial I}{\partial u} \end{Bmatrix} \begin{bmatrix} \frac{\partial w}{\partial A} & \frac{\partial w}{\partial T} \\ \frac{\partial u}{\partial A} & \frac{\partial u}{\partial T} \end{bmatrix} \right) \\ & + \begin{Bmatrix} \psi_a \\ \psi_s \end{Bmatrix}^T \left(\begin{bmatrix} \frac{\partial R_a}{\partial A} & \frac{\partial R_a}{\partial T} \\ \frac{\partial R_s}{\partial A} & \frac{\partial R_s}{\partial T} \end{bmatrix} + \begin{bmatrix} \frac{\partial R_a}{\partial w} & \frac{\partial R_a}{\partial u} \\ \frac{\partial R_s}{\partial w} & \frac{\partial R_s}{\partial u} \end{bmatrix} \begin{bmatrix} \frac{\partial w}{\partial A} & \frac{\partial w}{\partial T} \\ \frac{\partial u}{\partial A} & \frac{\partial u}{\partial T} \end{bmatrix} \right) \end{aligned} \tag{47}$$

which, after rearranging the terms, becomes:

$$\begin{aligned} \begin{Bmatrix} \frac{dI}{dD} \end{Bmatrix} = \begin{Bmatrix} \frac{\partial L}{\partial D} \end{Bmatrix} = & \left(\begin{Bmatrix} \frac{\partial I}{\partial A} & \frac{\partial I}{\partial T} \end{Bmatrix} + \begin{Bmatrix} \psi_a \\ \psi_s \end{Bmatrix}^T \begin{bmatrix} \frac{\partial R_a}{\partial A} & \frac{\partial R_a}{\partial T} \\ \frac{\partial R_s}{\partial A} & \frac{\partial R_s}{\partial T} \end{bmatrix} \right) \\ & + \left(\begin{Bmatrix} \frac{\partial I}{\partial w} & \frac{\partial I}{\partial u} \end{Bmatrix} + \begin{Bmatrix} \psi_a \\ \psi_s \end{Bmatrix}^T \begin{bmatrix} \frac{\partial R_a}{\partial w} & \frac{\partial R_a}{\partial u} \\ \frac{\partial R_s}{\partial w} & \frac{\partial R_s}{\partial u} \end{bmatrix} \right) \begin{bmatrix} \frac{\partial w}{\partial A} & \frac{\partial w}{\partial T} \\ \frac{\partial u}{\partial A} & \frac{\partial u}{\partial T} \end{bmatrix} \end{aligned} \tag{48}$$

In this equation, the very last matrix, that contains the sensitivities of the state variables with respect to the design variables, is computationally expensive for a high number of design variables, since it requires one converged coupling computation for each design variable. This makes the direct computation of the gradients unaffordable. To eliminate this term, the adjoint field vector ψ is found such that:

$$\begin{Bmatrix} \frac{\partial I}{\partial w} & \frac{\partial I}{\partial u} \end{Bmatrix} + \begin{Bmatrix} \psi_a \\ \psi_s \end{Bmatrix}^T \begin{bmatrix} \frac{\partial R_a}{\partial w} & \frac{\partial R_a}{\partial u} \\ \frac{\partial R_s}{\partial w} & \frac{\partial R_s}{\partial u} \end{bmatrix} = 0 \tag{49}$$

or

$$\begin{bmatrix} \frac{\partial R_a}{\partial w}^T & \frac{\partial R_s}{\partial w}^T \\ \frac{\partial R_a}{\partial u}^T & \frac{\partial R_s}{\partial u}^T \end{bmatrix} \begin{Bmatrix} \psi_a \\ \psi_s \end{Bmatrix} = -\begin{Bmatrix} \frac{\partial I}{\partial w} & \frac{\partial I}{\partial u} \end{Bmatrix}^T \tag{50}$$

Equation (50) is the coupled aero-structural adjoint equation. It is not dependent on the number of design variables, and should be solved one time for each aerodynamic or structural cost function or constraint. After solving this system of equations for the aero-structural adjoint field vector, this vector is used to compute the Lagrange function gradient:

$$\begin{Bmatrix} \frac{dI}{dD} \end{Bmatrix} = \begin{Bmatrix} \frac{\partial L}{\partial D} \end{Bmatrix} = \begin{Bmatrix} \frac{\partial I}{\partial A} & \frac{\partial I}{\partial T} \end{Bmatrix} + \begin{Bmatrix} \psi_a \\ \psi_s \end{Bmatrix}^T \begin{bmatrix} \frac{\partial R_a}{\partial A} & \frac{\partial R_a}{\partial T} \\ \frac{\partial R_s}{\partial A} & \frac{\partial R_s}{\partial T} \end{bmatrix} \tag{51}$$

In the next section, the terms presented in the coupled adjoint equation and the gradient will be discussed and derived in case it is not already implemented for the flow adjoint solver.

3.3 Terms of the Coupled Aero-Structural Adjoint Equations

A deeper look at the coupled adjoint (50) and gradient equations (51) and makes it clear that the terms included in this equation can be generally divided into three categories; aerodynamic terms, structure terms and cross terms. The components of the aerodynamic and the structure sensitivities originate from one system. For example, they might be sensitivities of aerodynamic residual with respect to the aerodynamic state variables, or sensitivities of a structural residual with respect to the structural thickness. On the other hand, the cross (off-diagonal) terms are sensitivities of one system with respect to the variables of the other system. These terms are responsible for exchanging the information between the aerodynamic and the structure adjoint fields. The terms of the coupled adjoint equation, followed by the terms of the gradients, are going to be discussed and derived if necessary.

The first aerodynamic term in the coupled adjoint equations (50) is the Jacobian $\partial R_a/\partial w$. This term represents the change in the aerodynamic residual that corresponds to a perturbation in the flow state variables. This Jacobian matrix, which has 6x6 elements for each grid node (in case of one-equation turbulent model), is a sparse matrix with values only corresponding to neighbouring and next neighbouring nodes. It is already derived and implemented in TAU [53]. For this reason, and while this study simply builds up on the existing flow adjoint approach, there is no effort needed in deriving or implementing this term.

The second aerodynamic term is $\partial I/\partial w$. It represents the right-hand side term in the linear flow adjoint equation used in the frame of shape optimization. This term is implemented in TAU's adjoint solver for different aerodynamic cost functions like drag, lift and pitching moment. Since in this study, the cost function will be a combination of aerodynamic objectives, there is no need to do any further derivation and implementation here unless the chosen cost function is not among the differentiated list.

The next term is the structural term $\partial \mathrm{R_s}/\partial \mathrm{u}$. It represents the way the structural residual changes as a response to a change in the structural displacements. It is clear from equation (41) that this term is nothing but the negative of the finite element stiffness matrix (-*K*). To use this matrix, it can be written out by the structure solver, or can even be used inside it while solving the structural adjoint equation as will be explained later.

The following term is the off-diagonal term $\partial \mathrm{R_s}/\partial \mathrm{w}$. This sensitivity represents the change in the structural residual corresponding to a change in the flow state variables. Having the possibility in TAU to exchange between the primitive and the conservative flow variables, this term is derived with respect to the primitive flow state variables. In the structural residual, only the aerodynamic force is directly related to the flow state variables. Therefore, when considering only the primitive flow state variables, this matrix $\partial \mathrm{R_s}/\partial \mathrm{w}$ is represented as follows:

$$\left[\frac{\partial R_{\mathrm{S}}}{\partial w}\right] = \left[\frac{\partial F}{\partial w}\right] = \left[\frac{\partial F}{\partial p}\right] \tag{52}$$

where p is the pressure; the only primitive variable that directly affects the structural force F. This term is therefore reduced to the sensitivity of the structural forces with respect to the change in the flow pressure. To derive this term, the linear interpolation tool that interpolates pressure into forces had to be analytically differentiated.

The interpolation tool does the interpolation over three stages. In the first stage, it computes the pressure coefficient C_p from the pressure p on the *CFD* side, and then, in the second stage, the tool relates each *CSM* node to three geometrically relevant *CFD* nodes and interpolates the computed C_p on the *CSM* mesh using three weighting values, each corresponding to one *CFD* node. In the last stage, the tool computes the forces F on the *CSM* grid from the interpolated pressure coefficients. Using the chain rule, the three stages can be presented as:

$$\left[\frac{\partial F_{CSM}}{\partial p_{CFD}}\right] = \left[\frac{\partial F_{CSM}}{\partial C_{p_{CSM}}}\right]\left[\frac{\partial C_{p_{CSM}}}{\partial C_{p_{CFD}}}\right]\left[\frac{\partial C_{p_{CFD}}}{\partial p_{CFD}}\right] \tag{53}$$

The first stage, represented by the third term $\partial C_{p_{CFD}} \big/ \partial p_{CFD}$ can be derived using the equation:

$$C_p = \frac{p - p_\infty}{q_\infty} \tag{54}$$

where q_∞ is the incompressible stagnation pressure and p_∞ is the far-field pressure. Hence:

$$\frac{\partial C_{p_{CFD,i}}}{\partial p_{CFD,j}} = \begin{cases} \dfrac{1}{q_\infty} & ,i = j \\ 0 & ,else \end{cases} \tag{55}$$

The term representing the second stage in the interpolation process is ($\partial C_{p_{CSM}} / \partial C_{p_{CFD}}$). Each *CSM* node is related to three *CFD* nodes as mentioned previously. Let the three *CFD* nodes be (j_1, j_2, j_3) for any *CSM* node (i) (see Figure 22), then:

$$C_{p_i} = C_1 \; C_{p_{j1}} + C_2 \; C_{p_{j2}} + (1 - (C_1 + C_2)) \; C_{p_{j3}} \tag{56}$$

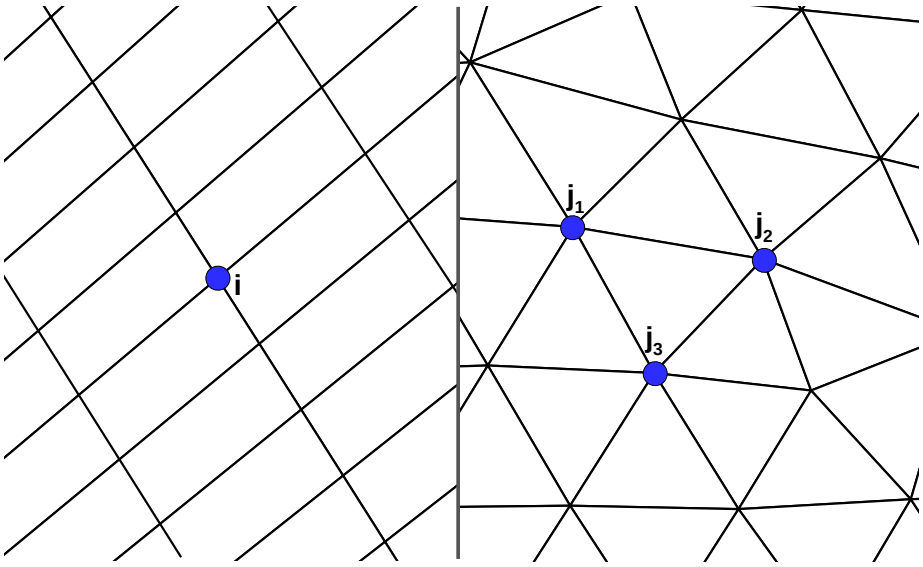

Figure 22: Pressure interpolation nodes from *CFD* grid (right) to the *CSM* grid (left)

which leads to:

$$\left[\frac{\partial C_{p_{CSMi}}}{\partial C_{p_{CFD_j}}}\right] = \begin{cases} C_1 & j = j_1(i) \\ C_2 & j = j_2(i) \\ 1-(C_1 + C_2) & j = j_3(i) \\ 0 & else \end{cases} \tag{57}$$

The last term, representing the third stage, is ($\partial F_{CSM} / \partial C_{p_{CSM}}$). If the force ($F_{e,m}$) is the force computed on the *CSM* shell element *m*:

$$F_{e,m} = C_p^* \; q_\infty n \tag{58}$$

where *n* is the normal of the CSM shell element in the *x,y* or *z* axis, and C_p^* is the average of interpolated C_p on the *CSM* element :

$$C_p^* = \frac{1}{nd} \sum_{kd=1}^{nd} C_{p,kd} \tag{59}$$

where *nd* is the number of nodes building an element (nd=|*ND*|); which means that *nd*=3 for triangular *CSM* elements and *nd*=4 for quadrilateral elements. . Assuming that *ne* is the size of set *NE* that include the neighbouring elements of a node (ne =|*NE*|), the force at each *CSM* node *i* is:

$$F_i = \frac{1}{ne} \sum_{ke=1}^{ne(i)} F_{e,ke} \tag{60}$$

and hence:

$$\left[\frac{\partial F_{CSM,i}}{\partial C_{p_{CSM,j}}} \right] = \begin{cases} \dfrac{q_\infty}{ne(i)} \displaystyle\sum_{ke \in NE(i)} \frac{n_{ke}}{nd_{ke}} & \ldots j \in ND_{ke} \\ 0 & \ldots j \notin ND_{ke} \end{cases} \tag{61}$$

Figure 23 presents an example of quadrilateral structural elements, showing the node force (in red) and the four element forces, in this example *ne* =4 for the force of interest *F* (in red) and *nd*=4 for each of the four elements.

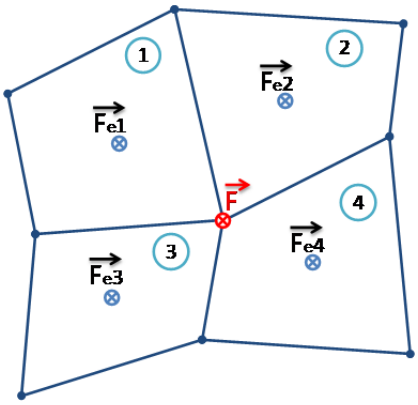

Figure 23: Force interpolation on the *CSM* grid with quadrilateral elements

To test the implementation of this term, the analytical differentiation was evaluated by comparison with the central finite differences for three grid nodes (see Figure 24). It is important here to mention that while performing the finite differences it was guaranteed that after perturbing the pressure at one *CFD* node, only the pressure coefficient at that *CFD* node was allowed to be perturbed in order to get the partial derivative. Otherwise, if C_p at other (neighboring) nodes was allowed to change, the resulting derivative would be the total derivative, and this is not what the sensitivity here represents.

The presented evaluation was performed for three nodes, each with respect to the forces in the three directions (*x,y* and *z*). It is worth mentioning here that the sensitivities with the highest peaks (as shown in the figure) represent the partial derivative of the forces along the y-axis, which, in this case, is the axis parallel to the vertical direction during the flight. This result is expected because a change in the pressure on the *CFD* side should affect mostly the interpolated forces (on *CSM* side) in the vertical (*y*) axis.

The last two terms remaining in the coupled adjoint equation are the off-diagonal term $\partial R_a / \partial u$ and the right-hand side term $\partial I / \partial u$. Using the chain rule, they can be decomposed as:

$$\left[\frac{\partial R_a}{\partial u}\right] = \left[\frac{\partial R_a}{\partial X_a}\right]\left[\frac{\partial X_a}{\partial u}\right] \tag{62}$$

and

$$\left\{\frac{\partial I}{\partial u}\right\} = \left\{\frac{\partial I}{\partial X_a}\right\}\left[\frac{\partial X_a}{\partial u}\right] \tag{63}$$

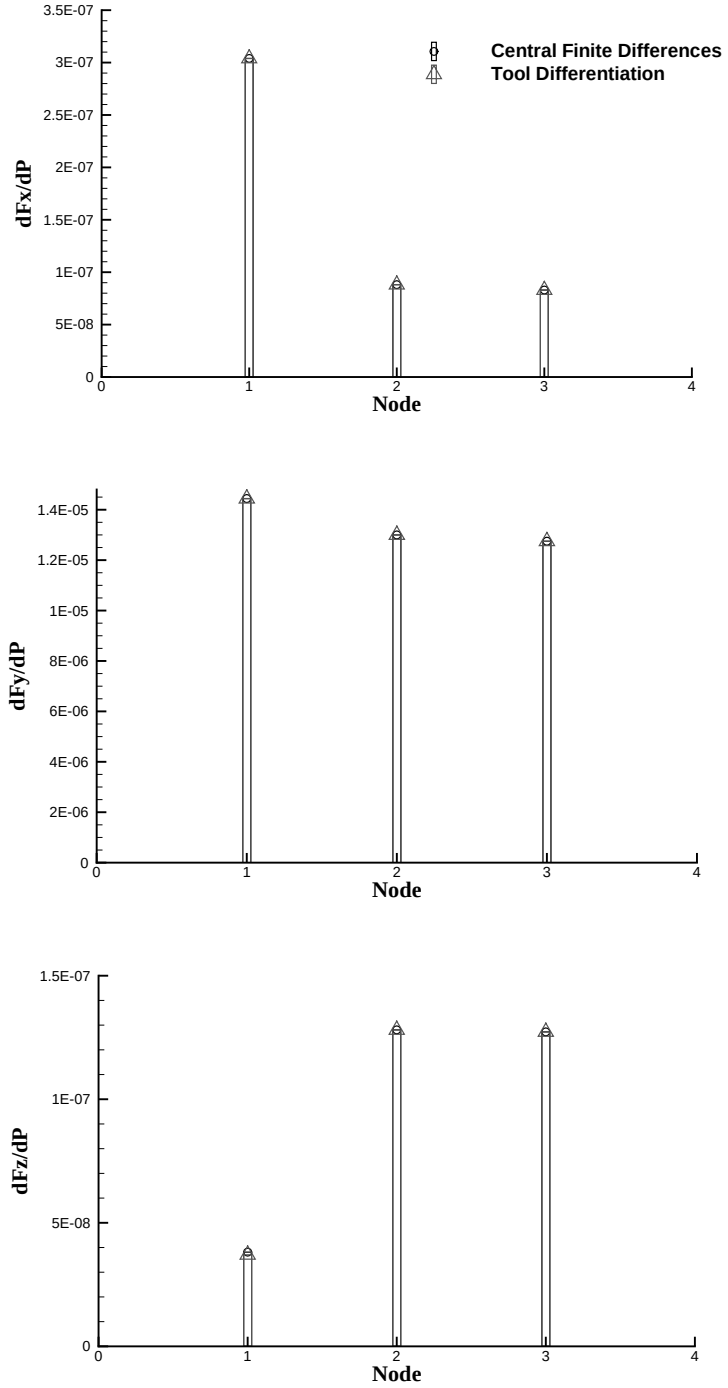

Figure 24: Validation of the differentiation of the linear interpolation

where X_a represents the *CFD* mesh. Making use of the existing differentiation of $\partial I/\partial X_a$ and $\partial R_a/\partial X_a$ in TAU [54], only the term $\partial X_a/\partial u$ needs to be derived instead of those two terms. $\partial X_a/\partial u$ is the sensitivity of the aerodynamic mesh corresponding to a change in the structure deformation u. The derivation of this term is dependent on the tool that interpolates deformations from the *CSM* grid to the *CFD* grid. For this reason, the volume-spline based RBF interpolation tool was differentiated and then the result was evaluated against central finite differences.

The RBF interpolation technique within Tau [72] is described through the following set of equations:

$$\{U_{x,y,z}\} = [A]\ \{\lambda_{x,y,z}\} \tag{64}$$

where U is the vector of the known structural displacements in one of the three directions (x,y or z), A is an interpolation matrix which is made of the *CSM* grid coordinates, and λ represents the interpolation coefficients vector that will be later used to compute the displacements (x,y or z) on the *CFD* side.

$$\begin{Bmatrix} 0 \\ 0 \\ 0 \\ 0 \\ u_{x1} \\ . \\ . \\ u_{xns} \end{Bmatrix} = \begin{bmatrix} 0 & 0 & 0 & 0 & 1 & 1 & ... & 1 \\ 0 & 0 & 0 & 0 & x_1 & x_2 & ... & x_{ns} \\ 0 & 0 & 0 & 0 & y_1 & y_2 & ... & y_{ns} \\ 0 & 0 & 0 & 0 & z_1 & z_2 & ... & z_{ns} \\ 1 & x_1 & y_1 & z_1 & 0 & \varepsilon_{12} & ... & \varepsilon_{1ns} \\ 1 & . & . & . & \varepsilon_{21} & 0 & ... & . \\ . & . & . & . & . & . & ... & . \\ 1 & x_{ns} & y_{ns} & z_{ns} & \varepsilon_{ns1} & \varepsilon_{ns2} & ... & 0 \end{bmatrix} \begin{Bmatrix} \alpha_{x1} \\ \alpha_{x2} \\ \alpha_{x3} \\ \alpha_{x4} \\ \beta_{x1} \\ \beta_{x2} \\ . \\ \beta_{xns} \end{Bmatrix}$$

$$\begin{Bmatrix} 0 \\ 0 \\ 0 \\ 0 \\ u_{y1} \\ . \\ . \\ u_{yns} \end{Bmatrix} = \begin{bmatrix} 0 & 0 & 0 & 0 & 1 & 1 & ... & 1 \\ 0 & 0 & 0 & 0 & x_1 & x_2 & ... & x_{ns} \\ 0 & 0 & 0 & 0 & y_1 & y_2 & ... & y_{ns} \\ 0 & 0 & 0 & 0 & z_1 & z_2 & ... & z_{ns} \\ 1 & x_1 & y_1 & z_1 & 0 & \varepsilon_{12} & ... & \varepsilon_{1ns} \\ 1 & . & . & . & \varepsilon_{21} & 0 & ... & . \\ . & . & . & . & . & . & ... & . \\ 1 & x_{ns} & y_{ns} & z_{ns} & \varepsilon_{ns1} & \varepsilon_{ns2} & ... & 0 \end{bmatrix} \begin{Bmatrix} \alpha_{y1} \\ \alpha_{y2} \\ \alpha_{y3} \\ \alpha_{y4} \\ \beta_{y1} \\ \beta_{y2} \\ . \\ \beta_{yns} \end{Bmatrix} \tag{65}$$

$$\begin{Bmatrix} 0 \\ 0 \\ 0 \\ 0 \\ u_{z1} \\ . \\ . \\ u_{zns} \end{Bmatrix} = \begin{bmatrix} 0 & 0 & 0 & 0 & 1 & 1 & ... & 1 \\ 0 & 0 & 0 & 0 & x_1 & x_2 & ... & x_{ns} \\ 0 & 0 & 0 & 0 & y_1 & y_2 & ... & y_{ns} \\ 0 & 0 & 0 & 0 & z_1 & z_2 & ... & z_{ns} \\ 1 & x_1 & y_1 & z_1 & 0 & \varepsilon_{12} & ... & \varepsilon_{1ns} \\ 1 & . & . & . & \varepsilon_{21} & 0 & ... & . \\ . & . & . & . & . & . & ... & . \\ 1 & x_{ns} & y_{ns} & z_{ns} & \varepsilon_{ns1} & \varepsilon_{ns2} & ... & 0 \end{bmatrix} \begin{Bmatrix} \alpha_{z1} \\ \alpha_{z2} \\ \alpha_{z3} \\ \alpha_{z4} \\ \beta_{z1} \\ \beta_{z2} \\ . \\ \beta_{zns} \end{Bmatrix}$$

In (65) x_i, y_i and z_i (i from 1 to *ns*) are the coordinates of the *CSM* nodes, *ns* is the number of *CSM* nodes and ε_{ij} represents the Euclidean distance between two *CSM* nodes:

$$\varepsilon_{ij} = \sqrt{(x_i - x_j)^2 + (y_i - y_j)^2 + (z_i - z_j)^2} \tag{66}$$

After solving equation (64) for the interpolation coefficients vector (λ) once for each direction, the vector coefficients are employed to compute the deformation for the *CFD* mesh (here with index *j*) by adding the deltas computed by:

$$\begin{aligned}
\Delta x_j &= \alpha_{x1} + \alpha_{x2}\, x_j + \alpha_{x3}\, y_j + \alpha_{x4}\, z_j + \sum_{i=1}^{ns} \beta_{xi} \sqrt{(x_j - x_i)^2 + (y_j - y_i)^2 + (z_j - z_i)^2} \\
\Delta y_j &= \alpha_{y1} + \alpha_{y2}\, x_j + \alpha_{y3}\, y_j + \alpha_{y4}\, z_j + \sum_{i=1}^{ns} \beta_{yi} \sqrt{(x_j - x_i)^2 + (y_j - y_i)^2 + (z_j - z_i)^2} \\
\Delta z_j &= \alpha_{z1} + \alpha_{z2}\, x_j + \alpha_{z3}\, y_j + \alpha_{z4}\, z_j + \sum_{i=1}^{ns} \beta_{zi} \sqrt{(x_j - x_i)^2 + (y_j - y_i)^2 + (z_j - z_i)^2}
\end{aligned} \tag{67}$$

to the *CFD* mesh coordinates. Following the two steps over which RBF functions (equation 64 then 67), the sought term $\partial X_a / \partial u$ can be decomposed using the chain rule into:

$$\left[\frac{\partial X_a}{\partial u}\right] = \left[\frac{\partial X_a}{\partial \lambda}\right]\left[\frac{\partial \lambda}{\partial u}\right] \tag{68}$$

From equation (67), the term $\partial X_a / \partial \lambda$ is found to be:

$$\left[\frac{\partial X_{ai}}{\partial \lambda_j}\right] = \varphi_j(X_i) \tag{69}$$

where

$$\varphi_j(X_i) = \begin{cases} 1 & j = 1 \\ x_i & j = 2 \\ y_i & j = 3 \\ z_i & j = 4 \\ \varepsilon_{ij} & j = 5 \ldots . n_s + 4 \end{cases} \tag{70}$$

Here *i* loops over the n_f which presents the number of *CFD* nodes. From equation (64), the term $\partial \lambda / \partial u$ is found to be:

$$\left[\frac{\partial \lambda}{\partial u}\right] = [A]^{-1} \tag{71}$$

Where *A* is invertible since the RBF used is a distance function for *ns* distinct points [73]. To test the differentiation and its implementation, the term was evaluated against the sensitivity computed via central finite differences. Figure 25 shows the validation of this term for different nodes corresponding to different degrees of freedom (*x,y,z*), where a very good matching is demonstrated.

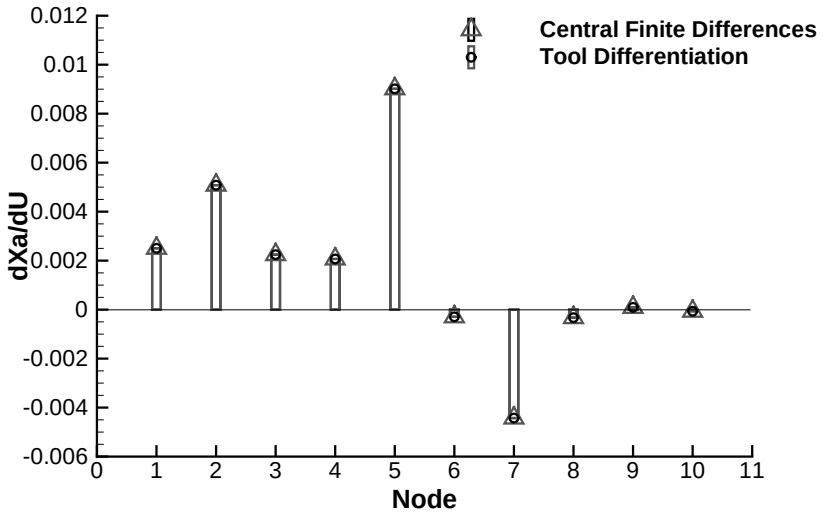

Figure 25: Validation of the differentiation of the RBF mesh deformation tool

By differentiating of the RBF tool, all the terms in the coupled adjoint system of equations become available for inviscid as well as viscous flows, and for a structure that is described by the linear elasticity equation (41). Therefore, what is left now is to solve the coupled adjoint equations. In the following, the method used for solving the coupled system of equation will be presented.

3.4 Solution of the Coupled Aero-Elastic Adjoint Equation

The coupled adjoint equation (50) is solved here using a lagged iterative method. This iterative method functions quite similarly to the aero-structural coupling itself, where here the lagged aerodynamic and structure adjoint vectors are exchanged until they converge. The two lagged equations are:

$$\left[\frac{\partial R_a}{\partial w}\right]^T \{\psi_a\}^{current} = -\left\{\frac{\partial I}{\partial w}\right\}^T - \left[\frac{\partial R_s}{\partial w}\right]^T \{\psi_s\}^{previous} \tag{72}$$

and

$$\left[\frac{\partial R_s}{\partial u}\right]^T \{\psi_s\}^{current} = -\left\{\frac{\partial I}{\partial u}\right\}^T - \left[\frac{\partial R_a}{\partial u}\right]^T \{\psi_a\}^{current} \tag{73}$$

where The lagged iterative system is solved as the following:

1. The solution is initialized for $\psi_s{}^{previous} = 0$.
2. Equation (72) is solved for ($\psi_a{}^{current}$).
3. Equation (73) is then solved for ($\psi_s{}^{current}$).
4. Convergence criterion is checked.
5. If the solution did not converge, back to step 2.

which is the block Gauß-Seidel method. To solve equation (72), the flow solver is used where the term ($[\partial R_s / \partial w]^T \{\psi_s\}^{previous}$) on the right hand side was added to the flow adjoint implementation within TAU. On the other hand, and since equation (73) is similar in its structure to equation (41); with ($[-K]^T = [\partial Rs / \partial u]^T$), equation (73) is solved by the structure solver. To allow that, there are two necessary points to be considered, firstly, the right hand side term ($-\left\{\frac{\partial I}{\partial u}\right\}^T - \left[\frac{\partial R_a}{\partial u}\right]^T \{\psi_a\}^{current}$) which represents the force in equation (41) is computed and provided to the structure solver. Secondly, the gravity switch within the structure solver needs to be turned off, as any other physical switches that the structure solver has in its default mode. The reason is that the problem to be solved here does not have the physical characteristics the linear elasticity problem has. Another way to solve equation (73) would be to write out the stiffness matrix and provide it to any other efficient linear solver. This method was tried as well within this thesis and proved efficient and successful.

3.5 Convergence of the Coupled Aero-Elastic Adjoint Solution

It was mentioned earlier that the solution of the flow adjoint equation costs almost the same as the solution of the flow problem. Since this applies to the structure part of the system, it applies to the complete coupled system as well.

Figure 26 presents the convergence history of the solution of the coupled adjoint equations applied to a wing-body configuration. The figure shows both the convergence of the residual of equation (73) and the update of the structural adjoint. Figure 27 presents the convergence of the residual of the l^2 norm for structural adjoint vectors at all *CSM* nodes, where residual here is just the value of the norm at coupling step n subtracted from the value of the norm at the next coupling step; n+1.

Here, the flow adjoint equation was solved 4 times and the structure adjoint equation was solved three times updating the structure adjoint field each time. As illustrated in Figure 26, the first structure update has the largest effect on the progress of the convergence; the following updates have less effect. Furthermore, the figure shows that the peaks indicating the structural adjoint update progressively decrease.

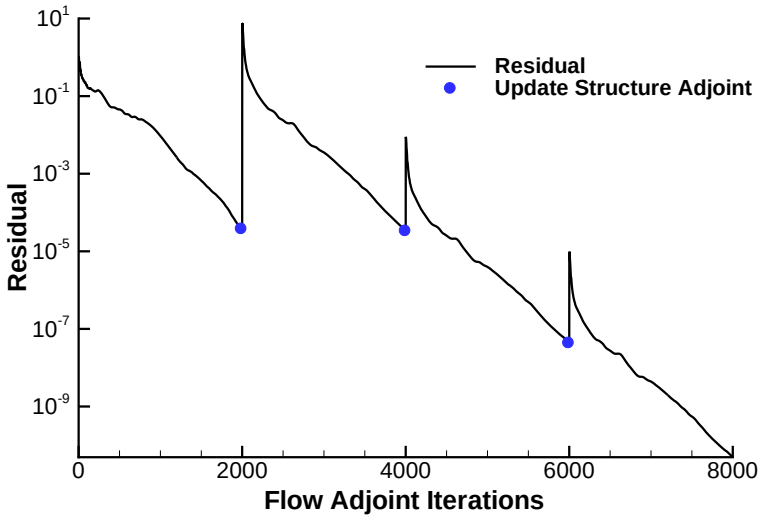

Figure 26: Convergence history of the solution of the aerodynamic adjoint equation

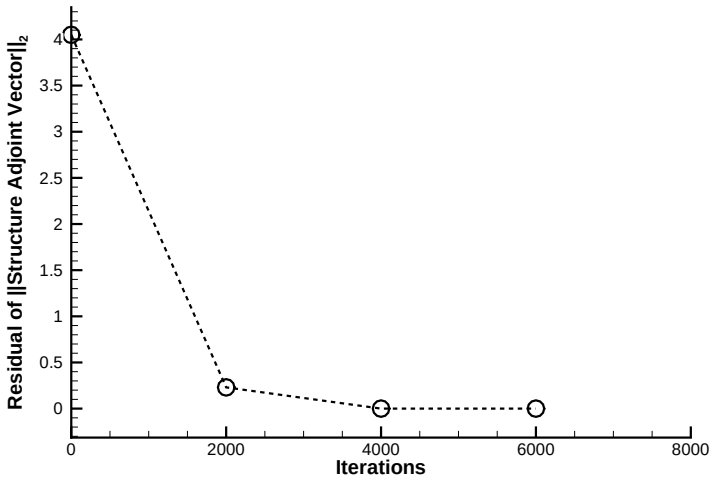

Figure 27: Convergence history of the structural adjoint vectors

3.6 Terms of the Gradients

As mentioned earlier, the objective of the optimization in this study will be aerodynamic performance, and shape design parameters will be employed to control the geometry during in the optimization. However, the effect of the structural elasticity will still be considered in order to insure accurate prediction of the aerodynamic coefficients.

The gradients are, as previously presented in (51):

$$\left\{\frac{dI}{dD}\right\} = \left\{\frac{\partial I}{\partial A} \quad \frac{\partial I}{\partial T}\right\} + \left\{\begin{matrix}\psi_a \\ \psi_s\end{matrix}\right\}^T \left[\begin{matrix}\frac{\partial R_a}{\partial A} & \frac{\partial R_a}{\partial T} \\ \frac{\partial R_s}{\partial A} & \frac{\partial R_s}{\partial T}\end{matrix}\right] \tag{74}$$

Having no structural design variables (T), the terms dependent on them vanish, as in (75):

$$\left\{\frac{dI}{dD}\right\} = \left\{\frac{\partial I}{\partial A} \quad 0\right\} + \left\{\begin{matrix}\psi_a \\ \psi_s\end{matrix}\right\}^T \left[\begin{matrix}\frac{\partial R_a}{\partial A} & 0 \\ \frac{\partial R_s}{\partial A} & 0\end{matrix}\right] = \left\{\frac{\partial I}{\partial A}\right\} + \{\psi_a\}^T \left[\frac{\partial R_a}{\partial A}\right] + \{\psi_s\}^T \left[\frac{\partial R_s}{\partial A}\right] \tag{75}$$

The differences between this gradient (equation 75), and the aerodynamic gradient presented in equation (21) is twofold; firstly the presence of the structure adjoint field ψ_s and the structure residual, and secondly the fact that the flow adjoint field contains now structural *information*, which was included in the flow adjoint field during the iterative solution of the coupled adjoint equations.

The terms in (75) can be decomposed using the chain rule as:

$$\left\{\frac{\partial I}{\partial A}\right\} = \left\{\frac{\partial I}{\partial X_a}\right\} \left[\frac{\partial X_a}{\partial A}\right] \tag{76}$$

and

$$\left[\frac{\partial R_a}{\partial A}\right] = \left[\frac{\partial R_a}{\partial X_a}\right] \left[\frac{\partial X_a}{\partial A}\right] \tag{77}$$

This gives the chance to compute this gradient in two ways, the first is by computing the term $\partial X_a / \partial A$ using the finite differences approach, and here the advantage of having an efficient mesh deformation tool plays a significant role. The second way is to use the previously described (section 2.3) finite differencing tool that computes directly $\partial I / \partial A$ and $\partial R_a / \partial A$. In both cases, the sensitivity $\partial R_s / \partial A$ is computed via finite differences. This sensitivity represents the change that occurs in the interpolation of forces when the shape design variables are perturbed. Fazzolari [74] suggests to neglect this term since its contribution to the gradients is small.

The central finite differences are chosen as a reference for validating the gradients obtained with the coupled adjoint approach. The test case chosen for this validation is the wing-body configuration mentioned in section (2.4). The validated cost function is drag at a constant lift, and the gradient of this objective is:

$$\frac{dC_D}{dA} = \frac{dC_D}{dA}_{\text{at fixed}\,\alpha} - \frac{\partial C_D / \partial \alpha}{\partial C_L / \partial \alpha} \left(\frac{dC_L}{dA}\right)_{\text{at fixed}\,\alpha} \tag{78}$$

where (α) is the angle of incidence. As seen in (78) the gradient of this objective requires the gradients of drag and lift; (dC_D / dA, and dC_L / dA), in addition to the partial

derivative of both coefficients with respect to the angle of attack; ($\partial C_D/\partial\alpha$, $\partial C_L/\partial\alpha$). These two are implemented in the adjoint solver, and are hence provided by the solver after the coupled flow adjoint computation has converged.

The parameterization employed here is the *FFD*. Nine design parameters that control the wing shape are chosen for the validation, where they were chosen at different points along the chord to ensure that the sensitivities at the leading and trailing edge, which are normally more sensitive to deformation, are accurate.

Figure 28 presents the gradient validation. The coupled adjoint gradients match very well with the central *FD* gradients. Even though two coupled adjoint computations were needed to compute the gradient of this cost function, the time needed is about 20% of that required to compute the gradients with the central finite differences approach.

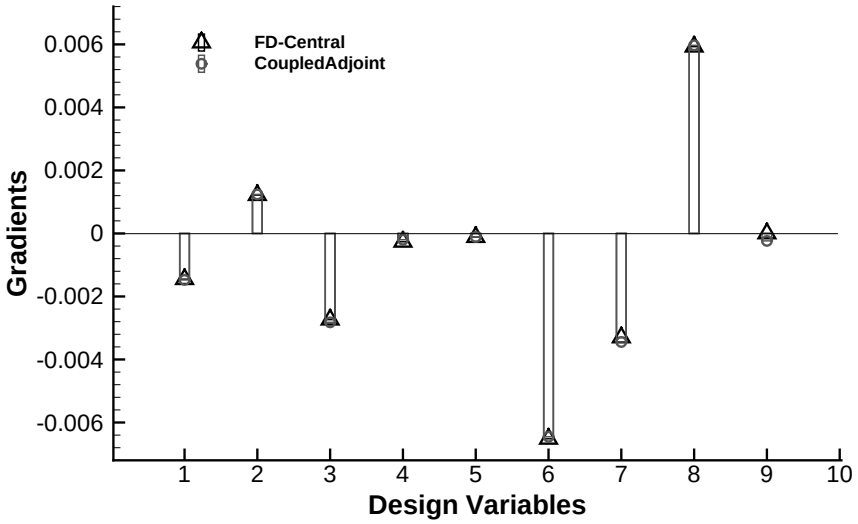

Figure 28: Validation of the gradients computed by coupled adjoint approach

Chapter 4: Elements of the Aero-Elastic Coupled Optimization

This chapter presents and discusses the main elements that will be used within the optimization scenarios in this study. Having the general aerodynamic optimization loop (Figure 1) in mind, the gradient-based aero-elastic optimization loop considered here is presented in Figure 29

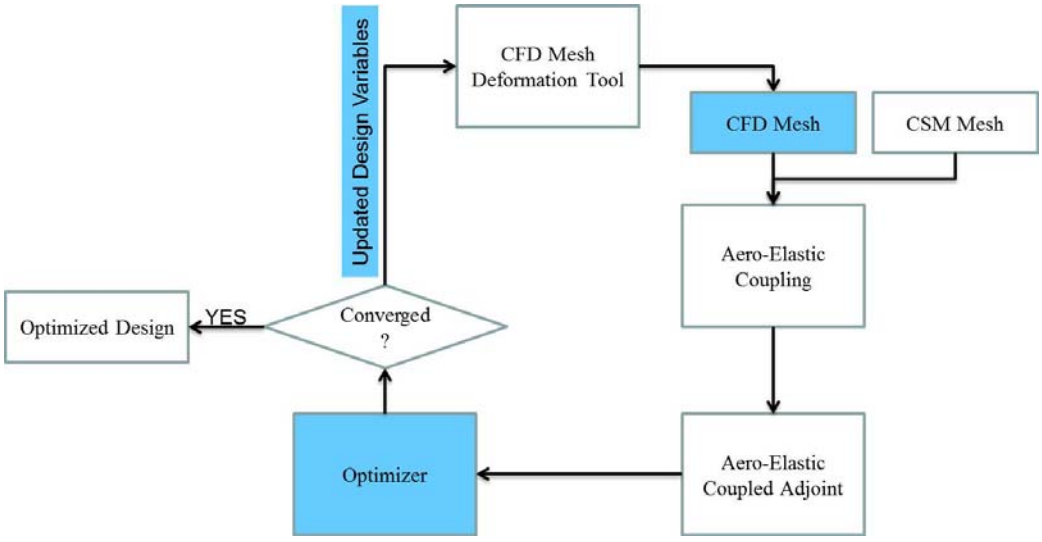

Figure 29: Information flow within the Aero-Elastic optimization

In the beginning, the *CSM* model employed within the optimizations is introduced. Then the three elements highlighted in Figure 29 (the *CFD* grid, the optimization algorithm, and the number of design parameters) in addition to the fidelity of the flow will be investigated. In the fidelity study, an optimization with viscous flow will be evaluated against another with an inviscid flow. The target here is to estimate the gain obtained by employing the viscous coupled adjoint approach, which is the target of this thesis. Then a *CFD* mesh consistency study is presented, where an O-type mesh topology is evaluated in order to find a suitable mesh for the intended aeroelastic optimization scenarios. After that, two gradient-based optimization algorithms are studied in order to find out which one performs more efficiently for the problem in hand. Finally, the effect of changing the number of design parameters on the optimum result is presented. The later three studies will respectively make the optimization results more reliable (mesh study), more efficient (optimization algorithm study) and with a higher degree of freedom to find an optimum (design variables study).

4.1 The Computational Structure Model

Before performing the mentioned studies, the *CSM* model is shortly introduced. The model at hand is a wing-body model that is based, as in the previous chapter, on the DO728 geometry. On the structure side, only the wing elasticity is considered and the fuselage elasticity is neglected. Hence, only the wing *CSM* model is required. Figure 30 presents the *CSM* model.

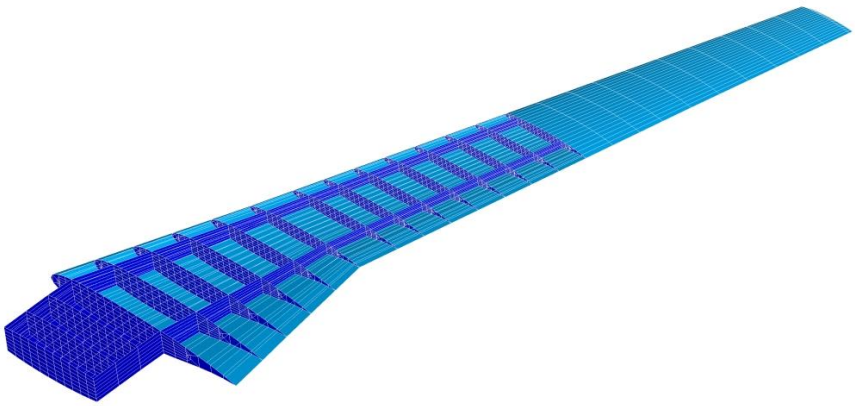

Figure 30: The *CSM* grid employed in the optimizations

The *CSM* grid, which was provided by the structure department of DLR, contains 4900 shell elements (dominantly quadrilaterals) and 4000 nodes. Each node possesses 6 degrees of freedom. This allows the wing to translate and rotate (bend and twist) in all directions. As seen in Figure 30, the structure model contains 27 ribs in the flow direction, two spars (front and back), and an upper and a lower skin (in light blue). The wing is made of aluminium alloys.

The *CFD* grid will be selected after the mesh consistency study in a following section.

4.2 Effect of Considering Viscosity

Reducing aerodynamic drag is one of the favored objectives in aircraft optimization studies. The aerodynamic drag can be divided into the normal to surface aerodynamic pressure, or form, drag, and the drag arising from the viscous shearing stresses, which is called the skin friction drag. In modern commercial transport aircrafts, the skin friction is said to contribute to around 50% of the total aircraft drag force [75]. Furthermore, viscosity results in building up the boundary layer around the wing surface. The pressure drag increases with the thickness of the boundary layer, which (the thickness) increases with the flow's Reynolds number. Hence, the effect of viscosity on the total drag is not negligible.

The coupled adjoint approach developed here can consider viscous as well as inviscid flows. To understand the gain obtained by considering the flow viscosity during the optimization, two optimization scenarios were defined, one with viscous flow and the other with inviscid flow. Unstructured grids of the MDOrmec configuration are used here. Figure 31 presents the grids. Both grids were controlled by 40 *FFD* design varia-

bles. The viscous grid contains 1.8 million grid points whereas the inviscid contains 200,000 nodes.

Two optimizations were performed, and after they converged, a viscous flow-structure coupling was computed for the best design resulting from the inviscid optimization. The convergence history of the optimizations and the resulting viscous computation on the final inviscid design are presented in Figure 32. Two aspects have to be considered here, the first is the drag reduction gained in both optimizations and the second is the computational time required.

The computational wall clock time required to perform the inviscid optimization was considerably less (around 50%) than that of the viscous optimization. However, as illustrated in Figure 32 the optimization that considers viscosity performed better (around 40%) in terms of drag reduction. This significant benefit clearly compensates the difference in the required computational power and boosts the consideration of viscosity during the optimizations.

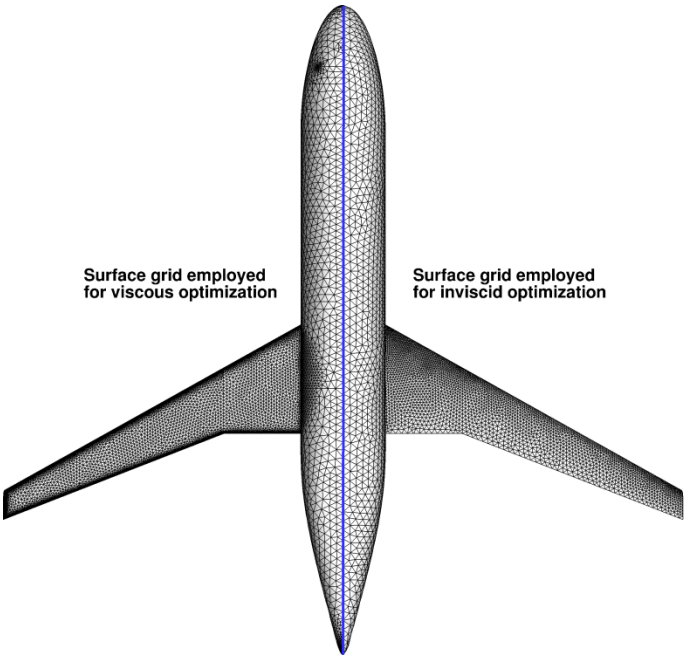

Figure 31: The grids employed in the flow fidelity study

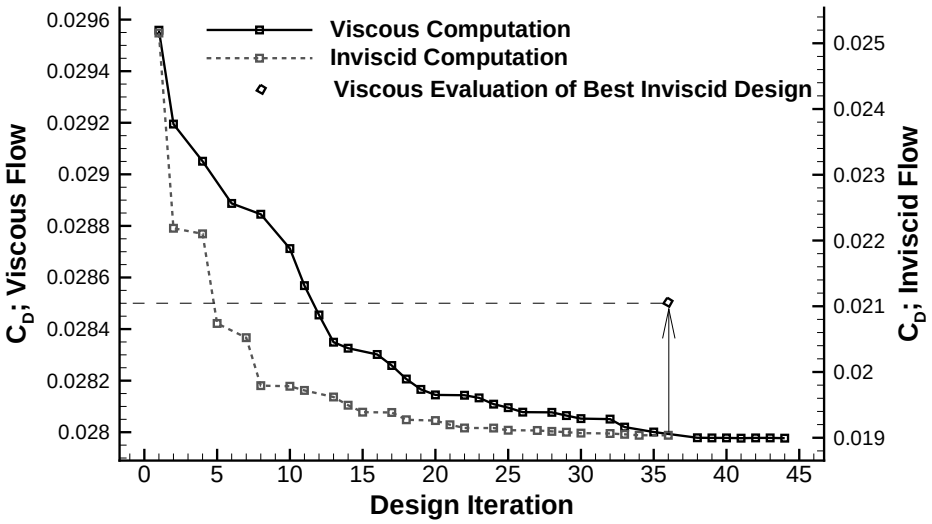

Figure 32: The convergence history of the inviscid and the viscous optimization and the viscous evaluation of the resulting inviscid design

4.3 CFD Mesh Study

While generating a *CFD* mesh that is intended for optimizations, one elementary aspect has to be considered. The mesh should be fine enough to catch the physics and coarse enough to be used efficiently in optimizations that might require several hundreds of flow computations to converge. Having the coupled aero-structural problem at hand only means that the number of flow computations will linearly increase by the number of couplings required for the system to converge. Fulfilling this aspect is not an easy task, and is usually tackled via a mesh study. Such study investigates if a coarse mesh and a finer mesh of the same geometry result in the same deviation in the (aerodynamic) coefficients when they are exposed to the same deformation. However, before starting such study, a so-called converged finer mesh needs to be found. Here the coarse grid is refined several times until a further refinement brings no change in the resulting flow coefficients.

The flow solver TAU can deal with both structured as well as unstructured grids. Unstructured grids are favoured, and often required, when the geometry is complex with many intersecting parts. On the other hand, structured grids are preferred when the geometry is less complex, since it is possible then to use fewer nodes in the wing spanwise direction (the direction normal to the flow direction), allowing for a higher aspect ratio of the grid elements. Since the geometry chosen for the optimizations is a clean wing-body geometry (not complex), a structured grid is favoured here.

Generally, structured grids can be O-type or C-type in the chordwise direction. Figure 33 shows the two grid types. As illustrated in the figure, the main difference between the two types is the resolution of the wake behind the wing in the C-type grid. Such resolution is beneficial since it enhances the prediction of the flow variables. However, the wake region in C-type structured grids might be negatively affected during the bending

of the wing, especially closer to the wing tip. This effect depends on the mesh deformation tool.

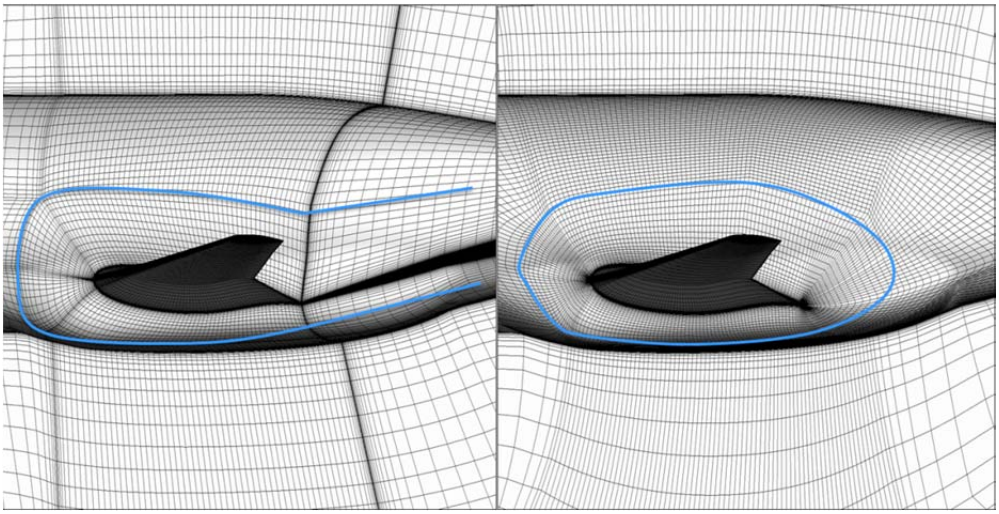

Figure 33: C-type (left) and O-type (right) structured grids

Figure 34 shows the wake region at the wing tip for the C-type mesh before and after the wing bending. As illustrated, the wake is not adequately following the wing anymore after the bending. One way to solve this problem would be to apply the same deformation that the wing undergoes on the wake region. However, handling the grid deformation technique is not the target of this study. This makes the O-type grid, which does not suffer from the deformation technique, more suitable for the aim of this study.

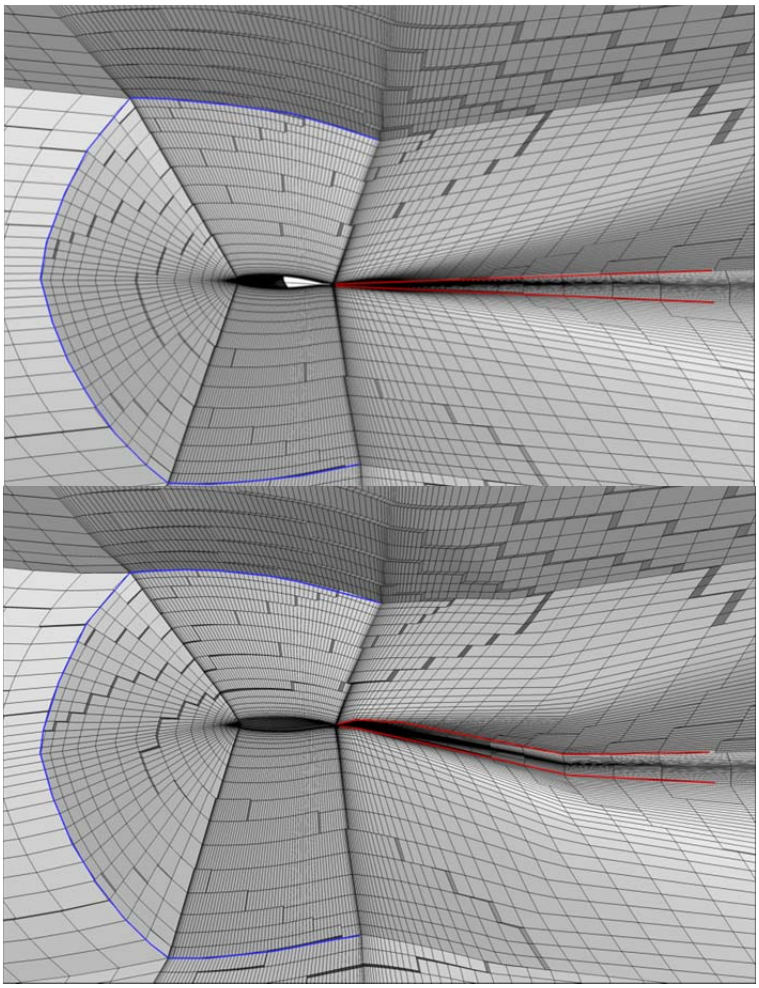

Figure 34: C-type grid cross-section at/behind the wing tip, before (upper) and after (lower) the wing deformation

4.3.1 Grid Refinement Study

If the computer round-off errors were excluded, the spatial discretization errors are expected to approach zero when the grid is refined. In the so-called grid refinement study, or *grid convergence* study, the O-type grid will be refined several times until a further refinement does not change the resulting flow variables. The grid is then said to have *converged*. Such study should actually be applied on the *CSM* model as well, until the structural displacements converge, however, in this work, such study is expected to be done by the provider of the *CSM* model [24], which is the structure department of DLR.

Four levels of grid refinement were required to get a converged grid. For the refinements, the number of nodes was firstly increased by a factor of 1.5 in each direction as suggested by [76], then by a factor of 2, and finally by a factor of 2.5 (for the third refinement) with respect to the basic grid. The basic (coarsest) grid had around 1.1 million nodes and the finest grid around 18 million nodes (see table 1). The grid was considered converged when the change in the drag coefficient was less than 0.5 drag counts for two successive grids. Figure 35 presents the grid convergence results. Here, the flow around

the wing-body configuration was computed for a target lift of C_L=0.417. The figure presents the drag for the different refinement levels.

As depicted in Figure 35, the difference in drag counts between the third and the fourth grid is around 0.4 drag counts, and hence the grid is considered *converged*.

Grid	Number of Nodes (*10^6)
Basic Grid	1.16
1st levelrefinement	3.92
2nd levelrefinement	9.28
3rd levelrefinement	18.13

Table 1: Number of nodes for the grids in study

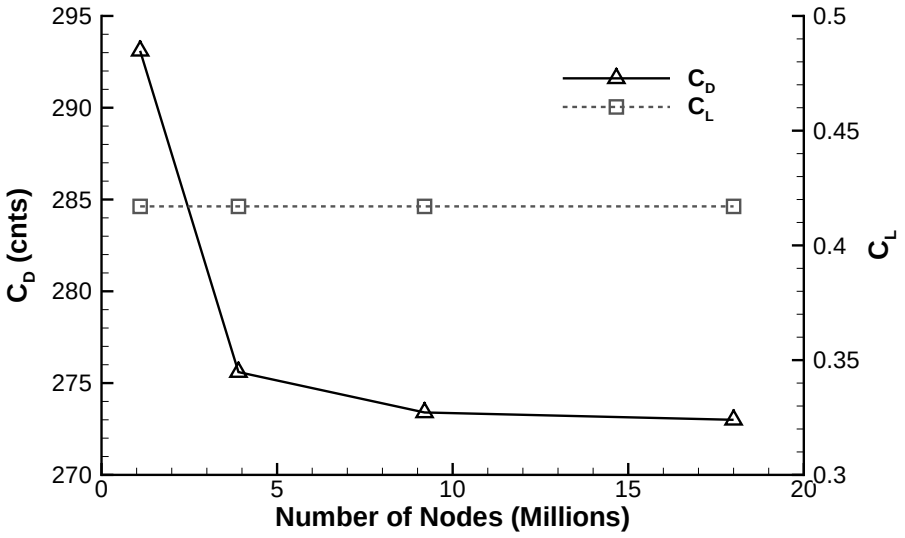

Figure 35: Grid refinement study

The grid refinement study has shown that a grid with 9 million nodes is required to predict acceptable values of the aerodynamic coefficients. In optimization however, considering such large grid is impractical from a computational cost point of view. Furthermore, the relative difference in aerodynamic coefficients that is achieved during the design iterations is of interest, and not the absolute values of these coefficients. Consequently, any coarse mesh that can catch the main aerodynamic features of the flow might be used in the optimization if the relative difference in aerodynamic coefficients is comparable to that on a *converged* grid when both grids undergo the same deformation.

To test that, every design variable has to be changed solely and the difference between the initial and the deformed grids of the coarse grid has to be validated with that of the fine grid. However, since this study is very expensive, a combination of design variables were modified once for both grids and the resulting deltas were compared. Both grids

were deformed using the same *FFD* design variables. Table 2 shows the results of the study.

As the table shows, the relative differences between the initial and the deformed grids are sufficiently close. One important source of difference here is that the computations were performed at a constant lift, which affects the angle of attack that has to be iteratively modified to satisfy the target lift. Having a little difference in the angle of attack deltas enhances the little difference in the aerodynamic coefficients. Nevertheless, the difference in the drag coefficient is small enough to consider the two grids to be *consistent*; bearing in mind the great benefit the coarser grid imposes on the computational cost.

Mesh	**O-type Mesh 1.16 Million Nodes**			**O-type Mesh 18.13 Million Nodes**		
Configuration	**Baseline**	**Deformed**	**Delta**	**Baseline**	**Deformed**	**Delta**
$C_{\text{-Lift}}$	0.417066	0.417081	**$1.57*10^{-5}$**	0.417122	0.417133	**$1.10*10^{-5}$**
$C_{\text{-Drag}}$	0.0293084	0.029889	**5.81** dc	0.0273056	0.0279025	**5.96**dc
$C_{\text{-My}}$	-2.242296	-2.239245	**0.0031**	-2.243720	-2.240171	**0.00355**
Angle α	-0.4574°	-0.4026°	**0.0548**°	-0.402	-0.355	**0.0470**°

Table 2: The aerodynamic coefficients of the initial and the deformed configurations for both grids

4.4 Optimization Algorithm Study

Three gradient-based optimization algorithms were introduced earlier in chapter 2, namely: the steepest descent (*SD*) algorithm, the conjugate gradient (*CG*) algorithm and the variable metric method (*VMM*) algorithm. This study will test the efficiency of the last two algorithms only; *CG* and *VMM*, since the *SD* algorithm is known to be less efficient. Both algorithms were tested before for different optimization problems and none have shown better efficiency for all cases. Since they were not tested for aero-elastic optimizations before, this study takes place here. In the following two optimizations will be carried out; one uses the *CG* algorithm and the other employs the *VMM* algorithm. The problem to be optimized is the same one introduced later in chapter 5.

The convergence history for both optimizations, which employed 40 design parameters, is plotted in Figure 36

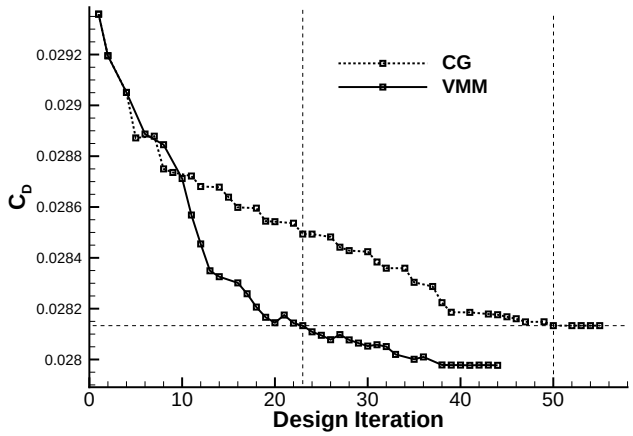

Figure 36: Convergence histories of the optimizations driven by *CG* and *VMM*

Before highlighting the difference between the two algorithms, it is worth mentioning the similarity. Figure 36 shows that the first two design iterations are exactly the same here, the reason is that the two algorithms follow the same step in the first two design iterations, afterwards *VMM* starts approximating the Hessian to use it in its progress.

Concerning the difference between the two algorithms, there are two points to consider here, first the efficiency (convergence rate) and second the number of gradient computations along the optimizations (computational cost). Concerning the efficiency, it is clear from the figure that the *VMM* algorithm has better convergence rate; the drag reduction that was achieved in 23 *VMM* design iterations is the same as that achieved by the *CG* algorithm after 50 iterations (the horizontal dashed line in Figure 36). Furthermore, concerning the second point, within the 23 iterations, the *VMM* optimizer needed the gradients 11 times (and 20 times along the whole optimization). On the other hand, using the *CG* algorithm, the optimizer required the gradients 14 times during the 50 iterations. This implies that the number of gradient computations is relatively higher during the *VMM* optimization. Assuming that a gradient computation costs roughly the same as a coupled flow-structure computation, the computational cost is still smaller using the *VMM* optimizer. Therefore, the *VMM* algorithm, which is cheaper and has better convergence rate, will be employed in this work.

4.5 Design Parameters Study

The advantage of using the adjoint approach in gradient-based optimizations is that the gradient computation is nearly independent of the number of design variables. Hence, having a high number of design variables, despite being too costly in gradient-free algorithms, introduces no cost problems. The highest number of design variables is reached when every grid point is controlled by the optimizer. This situation, however, does not guarantee a better result in terms of satisfying all constraints and reaching a lower minimum [77]. Hence, more design variables do not necessarily yield better final design, especially with the nature of the gradient-based algorithms that favours local minima.

Therefore, the target of this section is not to explore all the possibilities when it comes to the optimum number of design variables, but to perform some modifications on the

design parameter set described earlier (in section 2.4). The main idea here is to prove that such high-fidelity optimizations are possible to perform now with high number of design variables. This is neither possible with gradient-free algorithms, nor with gradient-based optimizations that do not employ the adjoint approach for the aero-elastic discipline, in a tolerable time.

The wing-body configuration will be controlled by *FFD* design parameters. The fuselage will be parameterized by fixed (not moving) parameters to keep it rigid, whereas the wing will be controlled by variable parameters. The structural thickness will not be optimized during the aero-elastic optimizations. To keep the volume inside the wing constant, the upper *FFD* control nodes are left to move freely, and their adjacent lower nodes follow them with exactly the same deformation. This implicit constraint is satisfied by letting the optimizer control only the upper nodes of the *FFD* box parameters on the wing. Such parameterization is comparable to a twist and camber-line parameterization.

In the basic parameterization a *FFD* box with 110 design parameters is used, 30 design parameters are fixing the body, and 80 parameters are on the wing, of which only 40 are independent (the upper side of the wing). Figure 37 presents the basic *FFD* parameterization used. The parameters in red are the fixed parameters, and the ones in green are free.

Two refinements to the basic design parameters setting were tested afterwards, the first was in the chordwise direction, and the second was in the spanwise direction. After that, the three settings; basic, chordwise refinement (CWR) and spanwise refinement (SWR), were optimized to test which setting enhances the design at most. The chordwise and the spanwise parameter refinements are presented in Figure 38 and Figure 39, respectively.

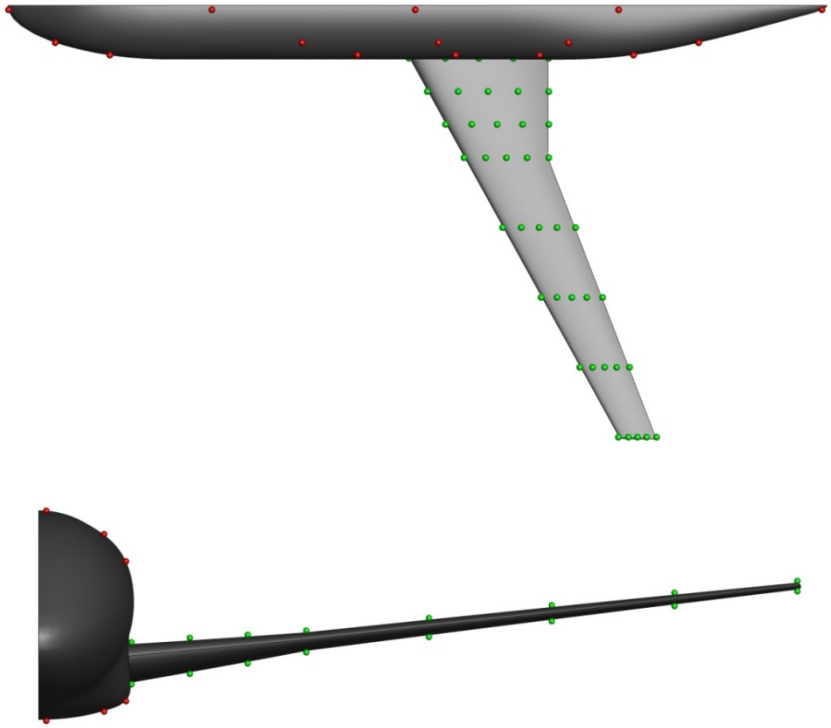

Figure 37: The top (up) and front (bottom) views of the basic design parameters setting, green are free and red are fixed parameters

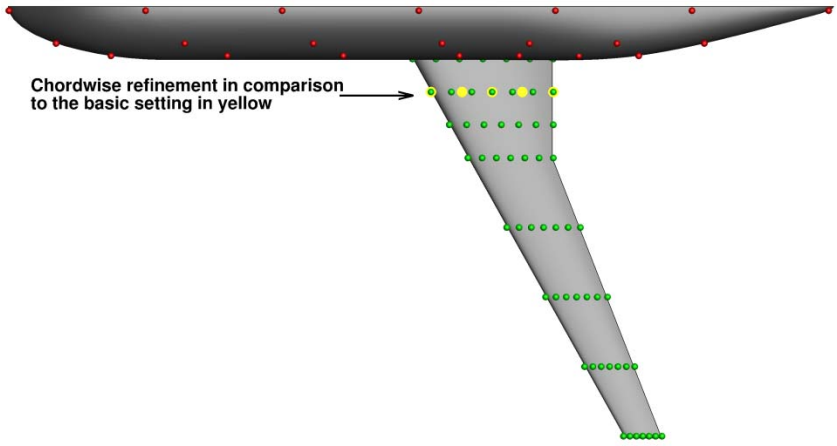

Figure 38: Top view of the chordwise refined (CWR) setting

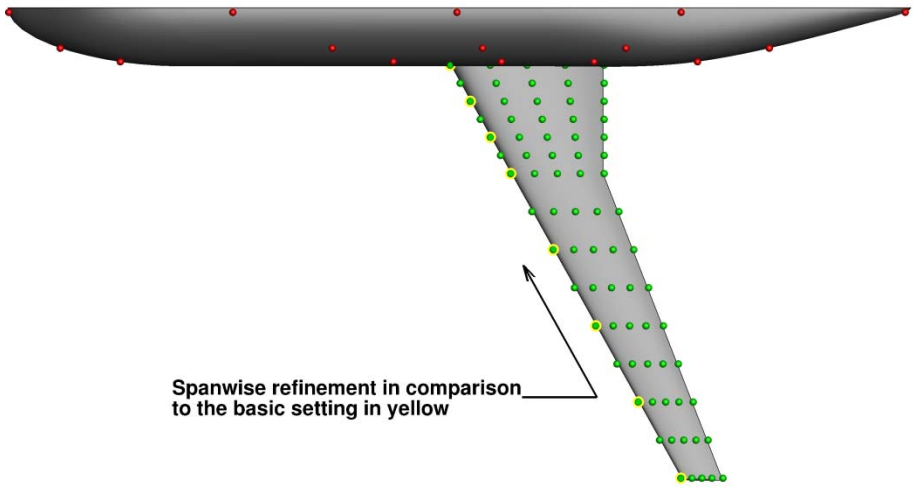

Figure 39: Top view of the spanwise refined (SWR) setting

Refining the basic parameterization in the chordwise-direction resulted in 112 design parameters on the wing, of which the upper half (56 parameters) is active. On the other hand, the spanwise refinement produced 150 wing design parameters, of which 75 control the wing upper side. Three aero-elastic optimizations corresponding to the three design parameters settings were performed. The convergence history of the optimizations is presented in Figure 40.

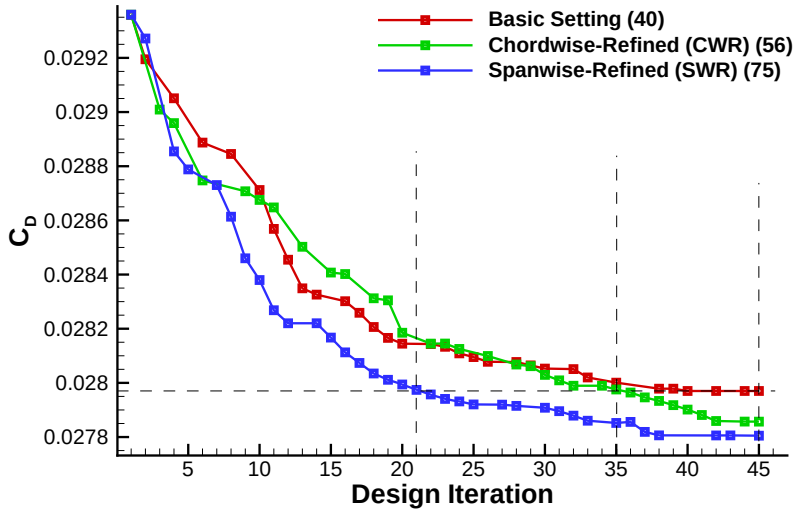

Figure 40: history of the optimizations performed within the design parameters study

As illustrated in Figure 40, both refinements converge to almost the same C_D, with a small benefit (less drag) for the SWR setting. The key factor to make a decision, which setting to choose here, is the rate of convergence. It is obvious here that the convergence rate of the SWR setting is much better than that of the other two settings. The drag reduction achieved in 21 design iterations with the SWR is the same achieved in 35 design iterations with the CWR setting and in 45 design iterations with basic setting. Con-

sequently, the SWR setting will be considered throughout the industry-relevant optimizations performed in the next chapter.

Chapter 5: Optimization Scenarios

Four aero-elastic optimizations will be presented in this chapter. The optimization elements chosen in chapter 4 will be employed here. This means that for *CFD* a structured O-type grid with 1.2 million grid points will be used, the *VMM* algorithm will drive the optimizations, and the wing will be parameterized using 75 *FFD* design variables that control the upper surface. The objective of the optimization is to reduce the drag at constant lift. Since changing the wing thickness can directly affect the drag, it will be implicitly constrained.

To start with, an unconstrained single point optimization will be run. Then the effect of taking several off-design points will be studied. After that, both optimizations will be repeated while taking a wing-root bending moment as an explicit constraint that the optimizer has to fulfil. At the end, the computational cost required during the optimizations will be presented.

5.1 Unconstrained Single-Point Optimization

The first optimization performed here is a single point optimization for cruise conditions of Ma=0.8, C_L=0.417 and Re=21e06. The optimization converged after 38 iterations, within which 25 gradient computations were required by the optimizer, where for each gradient computation; the gradients of drag as well as lift had to be computed. The convergence history is presented in Figure 41. The optimization reduced the drag by around 15 drag counts, while keeping both the lift and the wing thickness (Figure 42) constant.

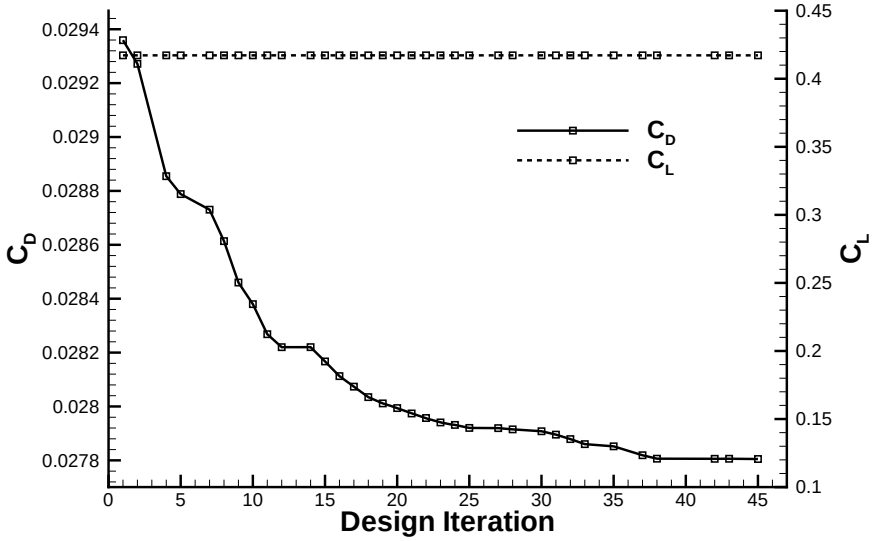

Figure 41: Convergence history of the unconstrained single point optimization

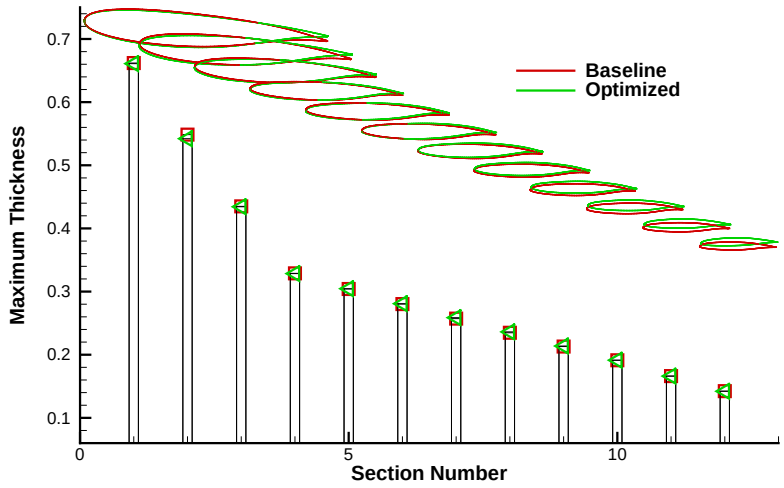

Figure 42: The wing sections' thicknesses were kept constant throughout the optimization

Figure 43 illustrates a comparison of the pressure contour between the baseline and the optimized designs for the top view followed by the front view. The top view emphasizes the fact that the pressure gradient decreased in the chordwise direction. The front view, on the other hand, shows how the optimized configuration is bent more than the baseline configuration. The reason for this higher bending will be discussed later.

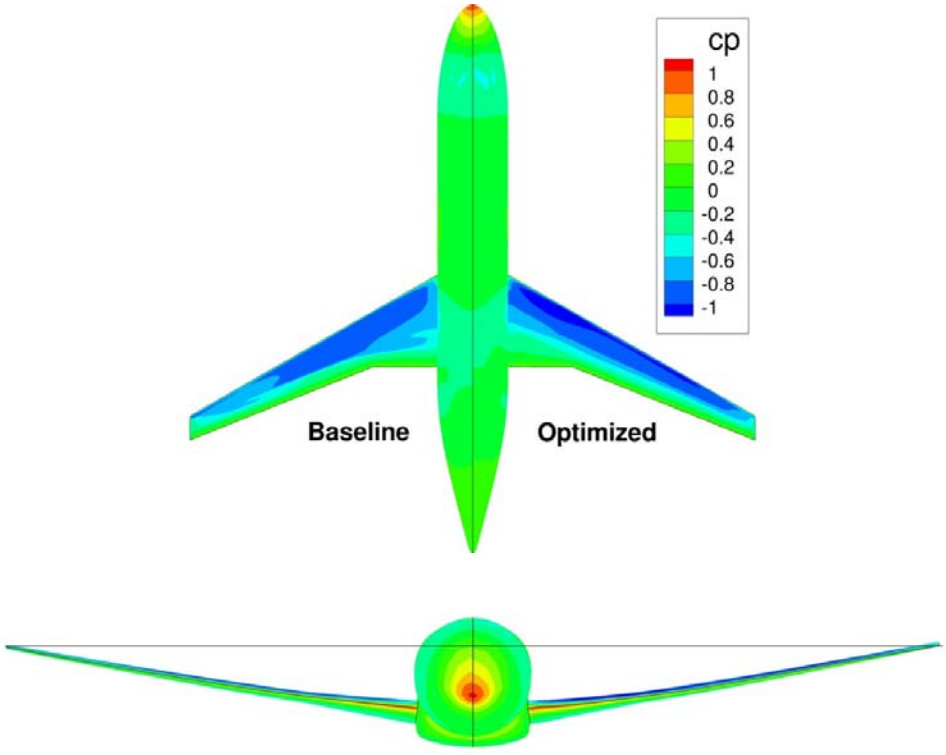

Figure 43: Top and front views for the Cp contour on both baseline and optimized configurations

A closer look at the chordwise pressure distributions is featured in Figure 44; here C_p is plotted at four sections chosen along the span of the wing. The figure shows how the shock was relatively smeared by the optimizer at the different wing sections.

The flow separation at the wing-body junction is plotted in Figure 45. It is clearly visible how the separation region is greatly decreased after the optimization. In order to decrease this separation, the optimizer twisted the wing section close to the wing-body junction as illustrated in Figure 46. At the station near the wing root (at around 0.2) we see a higher nose down twist for the optimized wing in comparison to the baseline wing. The difference in twists reduces afterwards until it increases again near the wing tip.

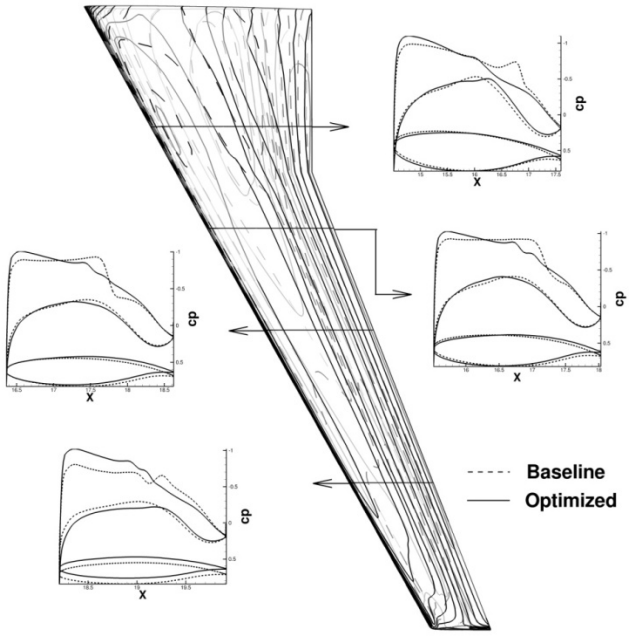

Figure 44: Chordwise Cp distribution of both baseline and optimized configurations for the single point optimization

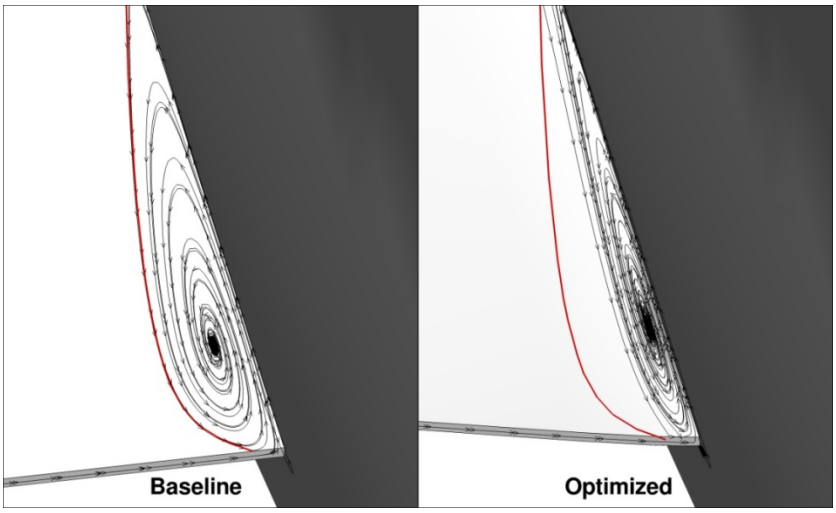

Figure 45: The flow separation at the wing-body junction for both configurations in the single point optimization.

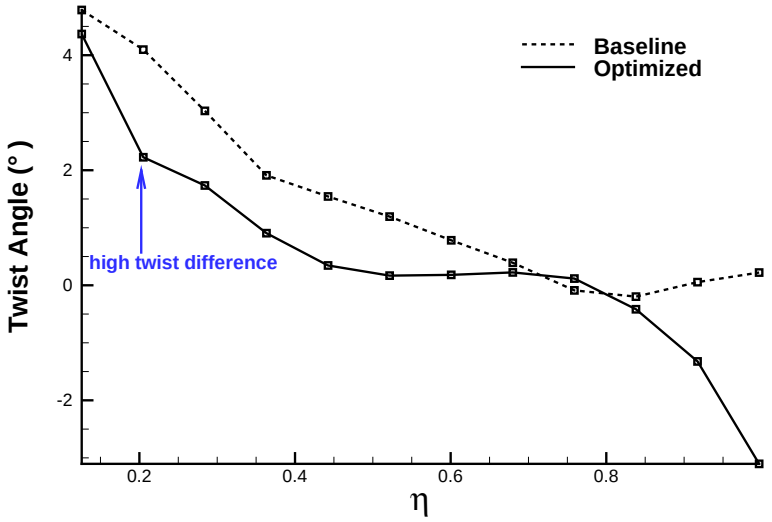

Figure 46: Twist distribution along the wings spans for the baseline and the optimized configurations

A comparison of the spanwise load distributions between the baseline and the optimized configurations is presented in Figure 47, which presents the lift and the local Cl, as well as the spanwise drag force distributions. The lift distribution plotted in the figure (upper part) shows that the optimized wing has a more elliptic distribution, which is expected because such distribution reduces the induced drag. However, this distribution also pushes the centre of lift towards the wing tip as illustrated in the figure (middle), and hence the higher root bending moment (and deflection at the wing tip) as mentioned earlier.

Increasing the root bending moment is disadvantageous from the structure point of view. The reason will be discussed later in section 5.3. This means that even though the optimization enhanced the configuration on the aerodynamic side, this should not be also the case for the structure side as well, especially that the optimizer is optimizing a purely aerodynamic objective, and lacks any feeling towards the structure of the wing.

5.2 Unconstrained Multi-Point Optimization

The previous optimization enhanced the configurations at the design point; however, the configuration flies at different flight conditions, therefore it is advantageous to consider other off-design conditions as well during the optimization. For this reason, this sections aims at performing the previous optimization while considering five flight conditions as pointed out (in blue) in Figure 48. Each point is defined using a different combination of Mach and C_L, with the main design point centring them as illustrated in the figure.

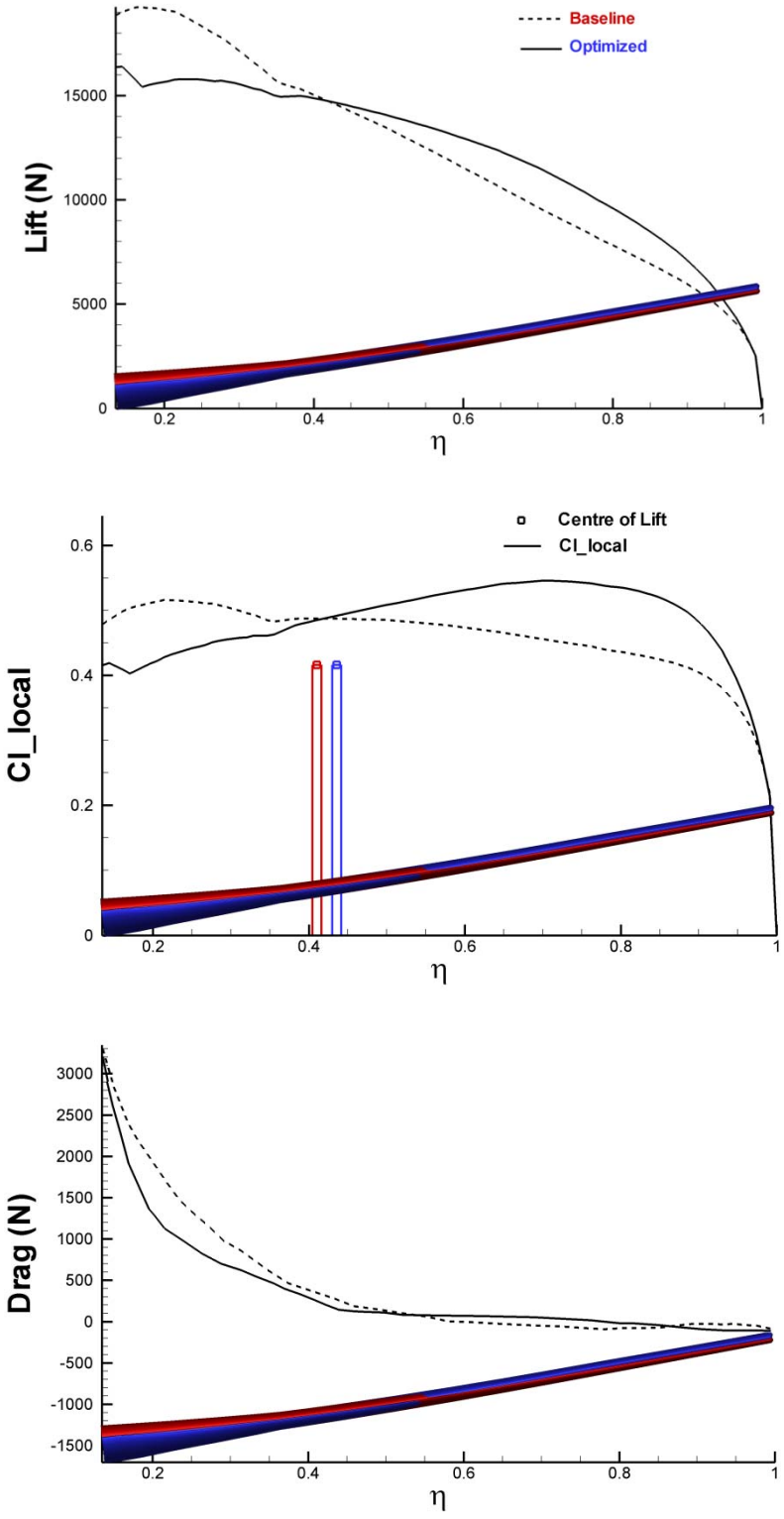

Figure 47: Comparison of load distributions; lift (upper), Cl (middle) and drag (lower)

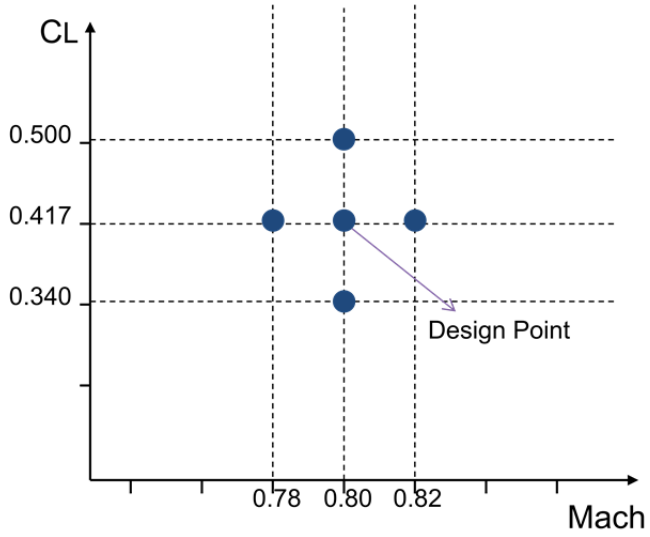

Figure 48: The points considered in the multi-point optimization

During the multi-point optimization, the five points were given the same weighting coefficient; this implies that they were equally treated and that it is wished that all five points would be enhanced equally. The cost function for this optimization would hence be:

$$Objective = \frac{1}{5}\sum_{i=1}^{5} C_{Di} \tag{79}$$

Having equal weighting coefficients, and a gradient based optimizer, it is expected that the points with the higher gradients achieve higher drag reduction. The reason is that the same weighting factors that apply on the points in the cost function, apply also on the points in the gradients computation. Hence, the two points with highest Cl and highest Mach number are expected to achieve higher drag reduction, as they are expected to have higher drag and hence higher drag gradients. This is probably not what a designer would seek; a designer would seek a higher drag reduction at the main design point. However, the idea here is simply to show that having the coupled adjoint approach makes it possible to perform such high-fidelity multipoint optimizations using the efficient gradient-based algorithms, which was not possible before with such high number of design parameters. Therefore, the weighting factors can be set equally and not much effort on studying their effect is set. An experienced designer might predict better which flight condition deserves higher weighting than the others do.

Figure 49 presents the convergence history of the multi-point optimization. Forty-two design iterations were needed for the optimization to converge. They included 11 gradient computations. Each included the solution of the coupled adjoint equations for both drag and lift. What is worth mentioning here is that using the coupled adjoint approach to compute the aero-elastic gradients saved around 80% of the computational time com-

pared to the conventional finite difference approach. This emphasizes the fact that this approach made such high-fidelity optimizations possible.

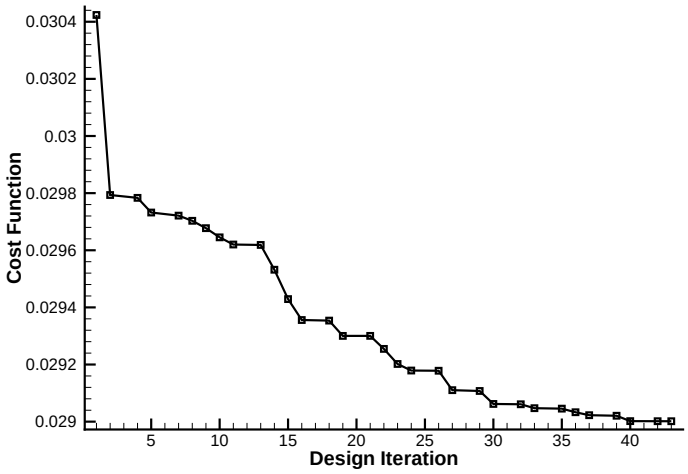

Figure 49: Convergence history of the multi-point optimization objective

As expected the two points with higher Mach number and higher Cl achieved higher drag reduction than the other points, see Table 3.Point 4 at Ma=0.82 enhanced the design at most by reducing 30 drag counts. The lowest drag reduction, on the other hand, was achieved at the lowest Mach number (Ma=0.78). Studying the table gives the designer a hint how to weight the different flight conditions.

	C_L	Ma	Drag reduct. (cnts)
Point 1	0.340	0.80	-7
Point 2	0.417	0.78	-5
Point 3	0.417	0.80	-8
Point 4	0.417	0.82	-30
Point 5	0.500	0.80	-19

Table 3: Drag reduction for the optimized flight conditions

To compare the multi-point optimization with the single-point optimization, the L/D and the drag rise (drag against Mach number) trends are plotted in Figure 50 and Figure 51, respectively. As illustrated in Figure 50, the design resulting from the single-point optimization performs better than the baseline configuration for the three Mach numbers at lower C_L values (mainly less than 0.46). For higher C_L values however, the baseline performs better. On the other hand, the resulting design of the multi-point optimization behaves better than the baseline for at all Mach values and for all C_L values. Furthermore, it also performs better than the single point for higher Mach numbers. The reason here is that the optimizer at higher Mach numbers, as mentioned earlier, had better chance to enhance the drag than at lower Mach number points. At Mach =0.82, the Multi-point design behaves better than the single-point design all over the plotted C_L range. At Mach=0.80, it is observed that the single-point design behaves better exactly at the design point (C_L=0.417), and worse otherwise. This last notice points out the expected behaviour of single-point and multi-point optimizations.

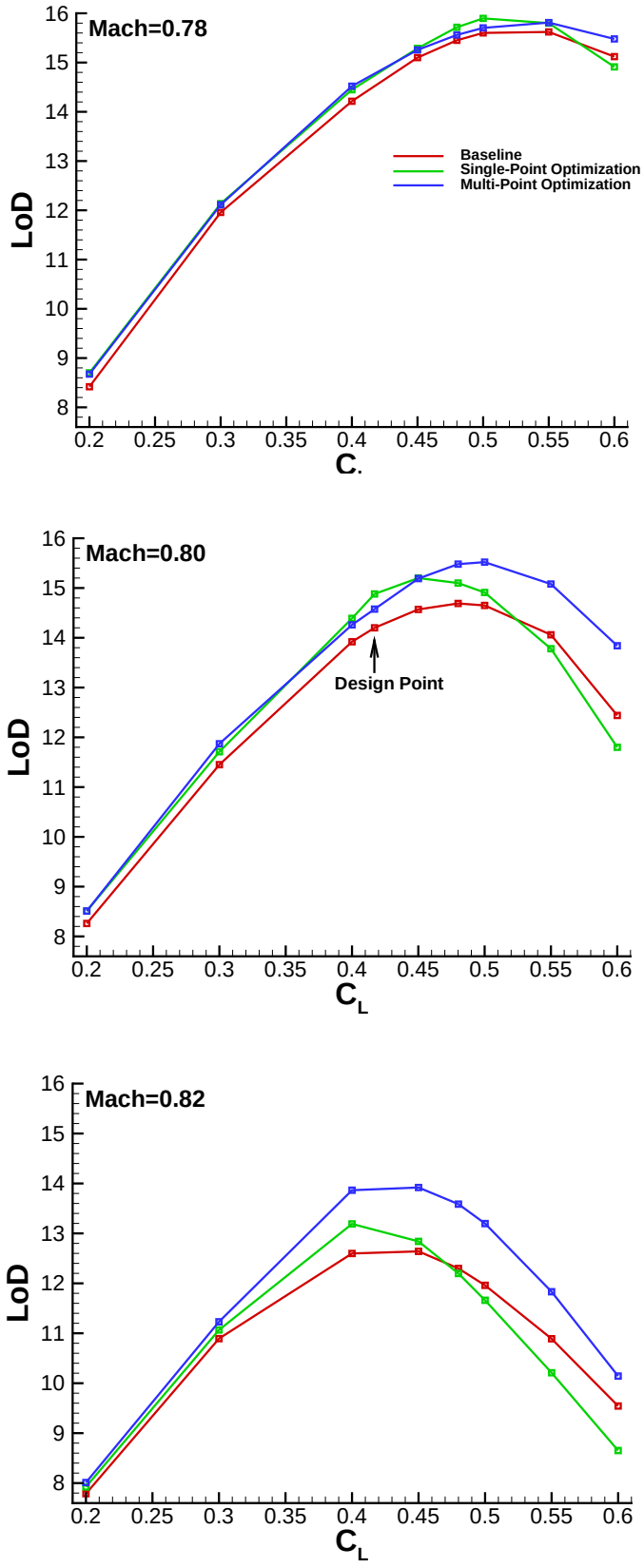

Figure 50: The LoD curve for the multi-point and single-point optimizations in comparison to the baseline configuration

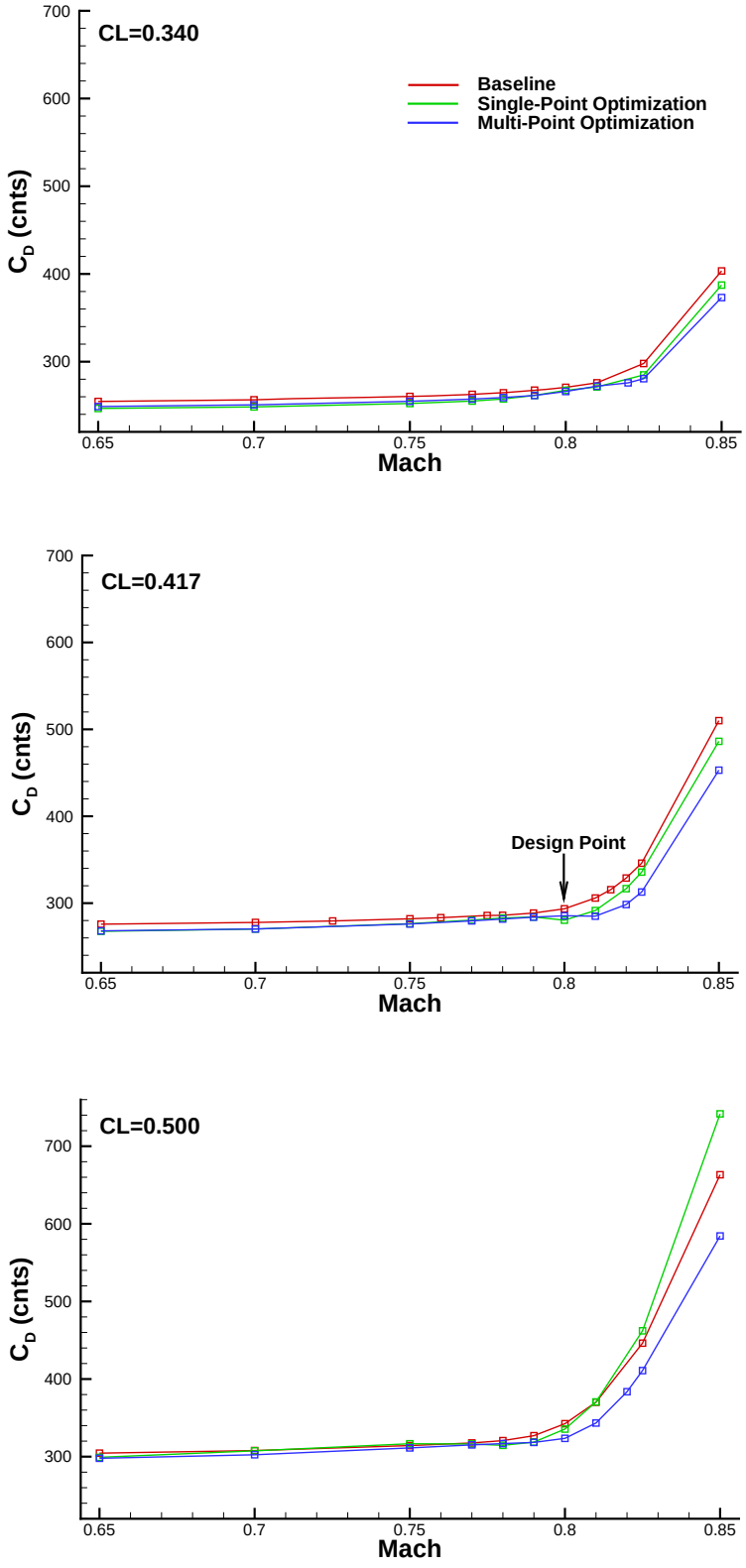

Figure 51: The drag rise trends for the multi-point and the single-point optimizations in comparison to the baseline configuration

The same behaviour can be seen in Figure 51, which presents the typical drag rise for a swept-back wing at three lift coefficients, where the single-point design produces less drag than the baseline configuration. However, at Cl=0.500, it starts to perform worse than the baseline for values higher than Mach=0.81. On the other hand, the resulting multi-point design experiences always less drag than the baseline, and performs better than the single-point design, at higher Mach numbers. Again, it can be noticed that at the design point, the single-point design performs better than the multi-point design as expected.

5.3 Constrained Single-Point Optimization

The spanwise lift distribution for the wing designed by the first single point optimization was close to the elliptical distribution as presented in Figure 47. This, relatively to the baseline configuration, shifted the centre of lift towards the wing tip and hence resulted in a larger bending of the wing. The elliptical distribution is of advantage for the aerodynamics as it refers to a lower induced drag. However, shifting the centre of lift towards the wing tip is disadvantageous for the structure, since this generates more wing root bending moment and hence higher structural stress, which requires increasing the structural thickness and consequently the wings structural mass.

As the cost function considered within this thesis is purely aerodynamic, it is not possible to consider the mass of the structure to deal with the mentioned root bending moment increase. A beneficial idea would be to keep the root bending moment constant. This, however, does not guarantee that the structural mass will not be increased. Nevertheless, keeping the bending moment constant can be used as a rough estimation for mass as will be shown and tested in the following.

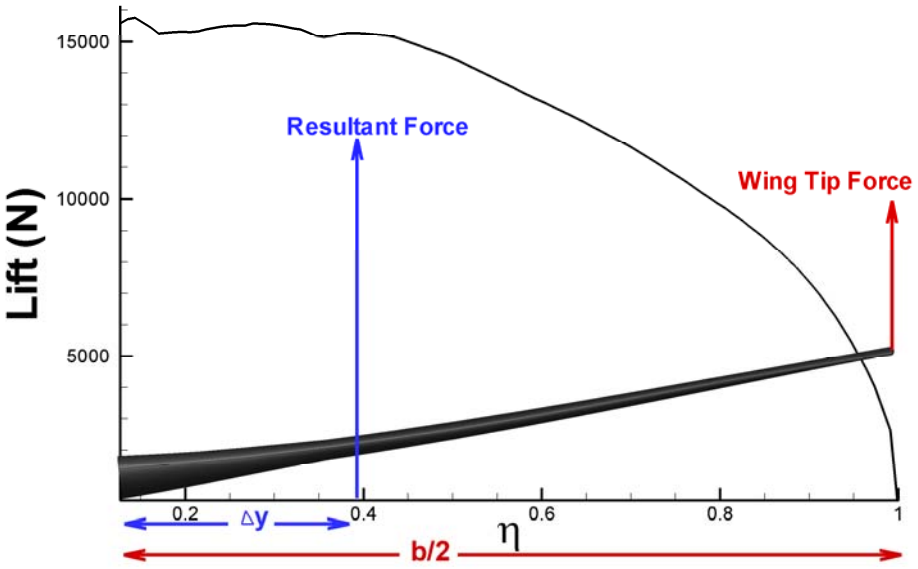

Figure 52: The resulting forces and moments on the wing

The rolling moment M_x and the root bending moment M_R for a given wing are defined in equations (80) and (81), respectively.

$$M_x = \frac{1}{2}\rho V^2 S C_{MX} \frac{b}{2} \tag{80}$$

$$M_R = \frac{1}{2}\rho V^2 S C_L \Delta y \tag{81}$$

Where S is the wing area, C_{MX} is the rolling moment coefficient and b is the span as illustrated in Figure 52. If the reference point is set to be the same -and at the wing root- for both moments, the moments become equal, hence:

$$C_L \Delta y = C_{MX} \frac{b}{2} \tag{82}$$

However, C_L is implicitly kept constant during the optimizations, and (b/2) which is half the span is not a design variable, therefore constant as well. This means that if the rolling moment coefficient C_{MX} is constrained during the optimization, the distance at which the resultant force applies will stay constant and this will keep the root bending moment constant. Therefore, in the next optimizations, the rolling moment will be explicitly constrained.

In order to have explicit constraints in the optimization, another optimization algorithm is required; one that can handle constraints. The sequential quadratic programming (SQP) algorithm [77] is used for this reason. SQP requires the value of the constraint (here C_{MX}) and its gradients with respect to the design variables at the end of each optimization cycle. Hence, the flow adjoint boundary condition of the rolling moment was modified by adding the term coming from the structural adjoint equation ($\psi_s^T \, dR_s/dW$) as presented in equation (50).

To test the relation between C_{MX} and the mass, a design of experiment (DOE) was performed for this configuration in another study [59] and the loose relation is plotted in Figure 53

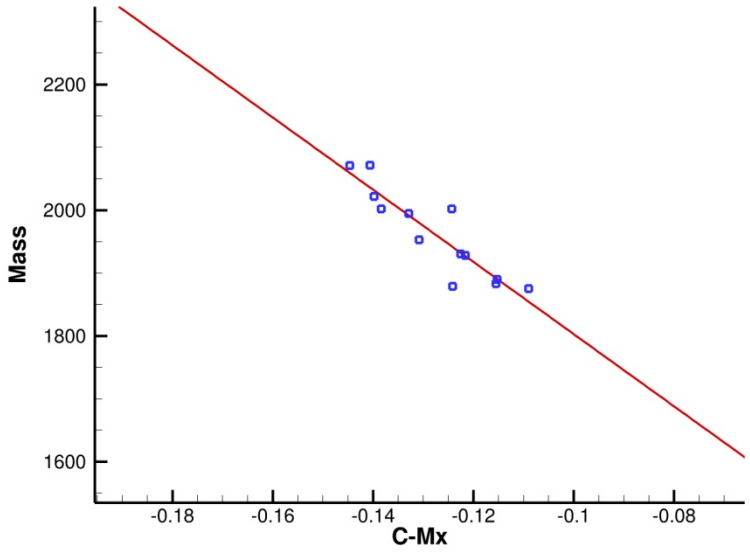

Figure 53: Rough relation between the wing mass and the rolling moment at constant C_L

The figure shows that when the rolling moment coefficient increases (here negatively), the mass of the wing increases, roughly linearly. Based on this rough linear relation and the unconstrained single-point optimization performed previously [section 5.1], Table 4 estimates the increase in mass due to the change in the root bending moment to be around 100 Kg.

	C_D	C_{MX}	Mass (Kg)
Baseline Configuration	0.2936	-0.1580	M_o
Optimized Configuration	0.2791	-0.1750	M_o + 100

Table 4: C_D, C_{MX} and the mass of the unconstrained single-point optimization

Therefore, another single-point optimization will be performed in this section with all the previous conditions kept the same expect for the rolling moment which will be explicitly constrained at its initial value of C_{MX} = - 0.1580.

Figure 54 presents the convergence history of the constrained optimization. It required 28 design iterations to converge and reduce the drag by around 13 drag counts, which is 2 drag counts less reduction than the unconstrained optimization. However, here C_{MX}, the centre of lift and hence the root bending moment are kept constant, as illustrated in Figure 55

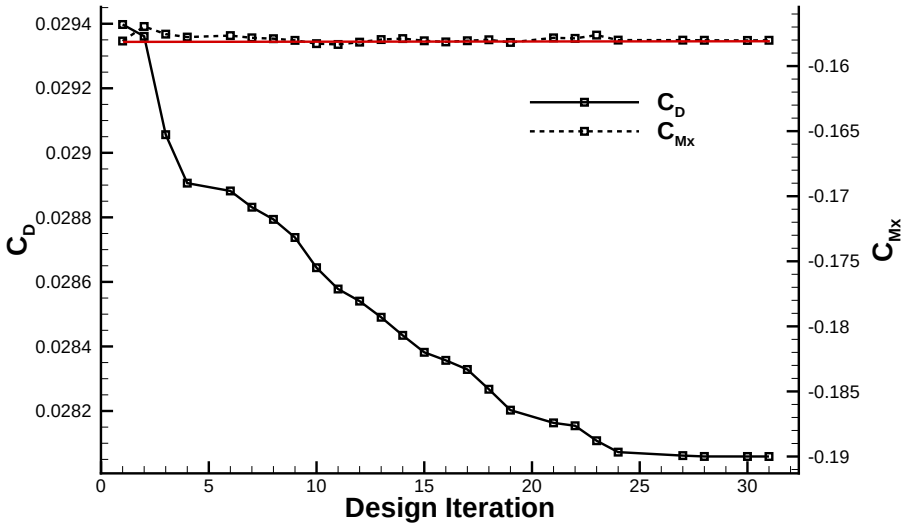

Figure 54: Convergence of the constrained single-point optimization

Constraining the problem also affects the number of design iterations required for convergence. As remarked from the convergence illustrated in Figure 54 in comparison to that in Figure 49, the constrained optimization needed 10 design iterations less than the unconstrained optimization.

Figure 55 shows that the spanwise lift distribution was not held constant; however, by adding the rolling moment constraint, the resulting spanwise lift distribution is closer to the baseline lift distribution than that of the unconstrained resulting design, and the local C_L distribution presents less chance for a flow separation close to the wing tip. The cost of fixing the centre of lift is two drag counts.

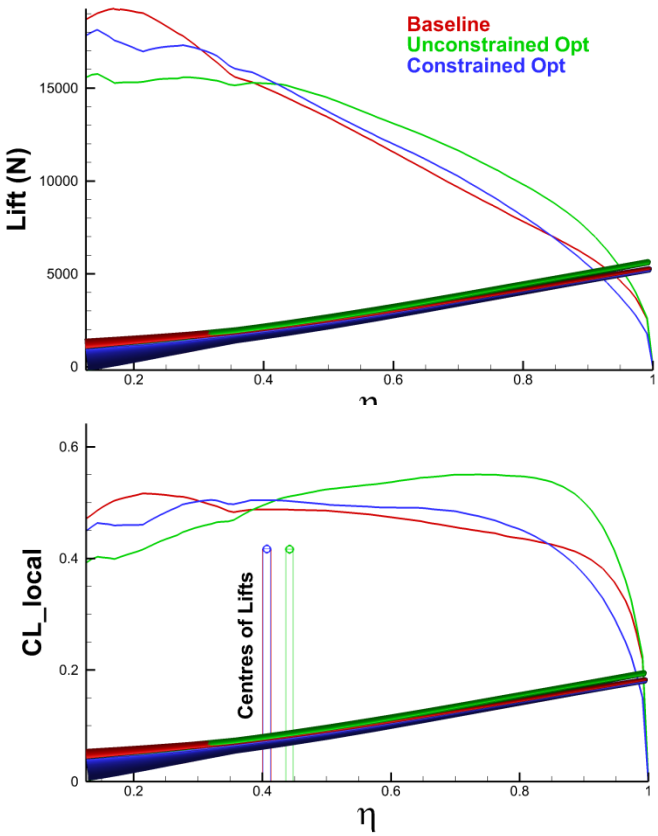

Figure 55: Spanwise local C_L and lift force distributions for the constrained and the unconstrained single-point optimizations compared to the baseline configuration

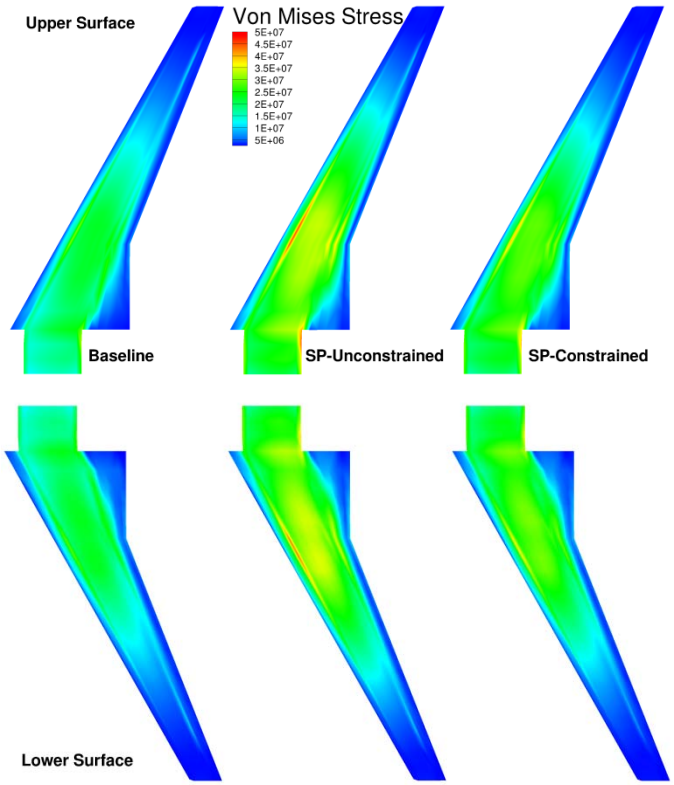

Figure 56: The Von-Mises stress for the wings resulting from the constrained and the unconstrained optimizations, in comparison to the baseline configuration

To look at the effect of constraining the rolling moment directly on the wing structure, Figure 56 presents the Von-Misses stress over the upper and the lower surfaces of the baseline wing in addition to the wings resulting from the unconstrained as well as the constrained optimizations. The stress on the wing resulting from the unconstrained optimization almost doubled at some regions when compared to the baseline wing. For the wing resulting from the constrained optimization, we can see that the stress increased as well but with much less values than in the unconstrained optimization. Figure 56 emphasizes the benefit achieved by adding the explicit rolling moment constraint to the aero-elastic optimization, which can be included now within the multi-point optimization.

5.4 Constrained Multi-Point Optimization

The addition of the rolling moment constraint to the aero-elastic optimization has its benefits on the wing structure; however, it can be computationally costly if the gradients of C_{MX} need to be computed for each flight condition. Therefore, the configuration resulting from the constrained single point optimization was further investigated, and the C_{MX} constraint was computed for this configuration at the five points. The results are plotted in Figure 57.

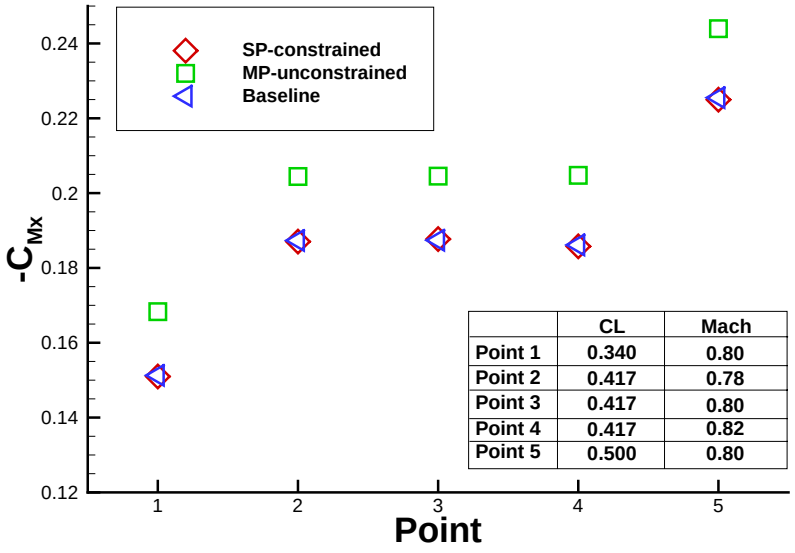

	CL	Mach
Point 1	0.340	0.80
Point 2	0.417	0.78
Point 3	0.417	0.80
Point 4	0.417	0.82
Point 5	0.500	0.80

Figure 57: C_{MX} of the Baseline configuration at the five points in comparison to the C_{MX} of the designs resulting from the constrained as well as the unconstrained optimizations

As illustrated in Figure 57, C_{MX} values of the baseline configuration those of the constrained single point optimization are very close. The highest deviation between the values for these two configurations occurs at the fifth point (C_L=0.5) and is equal to 0.24 % of its mean value (at the two points). This deviation is considered small enough in order to trade it for the computational cost benefit of computing the constraint gradient at one point only during the multi-point optimization. The point at which this constraint and its gradient are computed is chosen to be the design point.

The convergence history of the constrained optimization is presented in Figure 58.

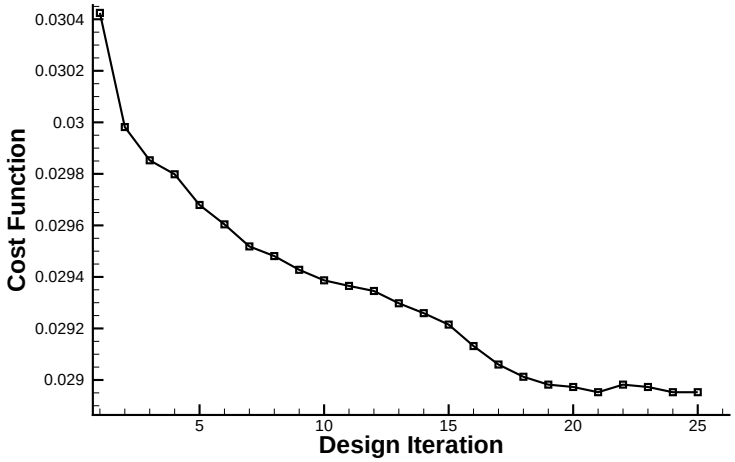

Figure 58: Convergence history of the constrained multi-point optimization cost function

The optimization required 25 design iterations to converge, within which, the gradients were required 20 times. Each gradient computation included five adjoint computations for drag, five for lift, and one for the rolling moment constraint, making 11*20 adjoint computations in total. The reduction of drag for each of the five points is presented in Table 5. Compared to the results shown in Table 3, it can be seen that the drag reduction for the constrained multi-point optimization is higher than that of the unconstrained multi-point optimization.

	C_L	Ma	Drag Reduct. (cnts)
Point 1	0.340	0.80	-7
Point 2	0.417	0.78	-5
Point 3	0.417	0.80	-7
Point 4	0.417	0.82	-32
Point 5	0.500	0.80	-22

Table 5: Drag reduction for the five points in the constrained multi-point optimization

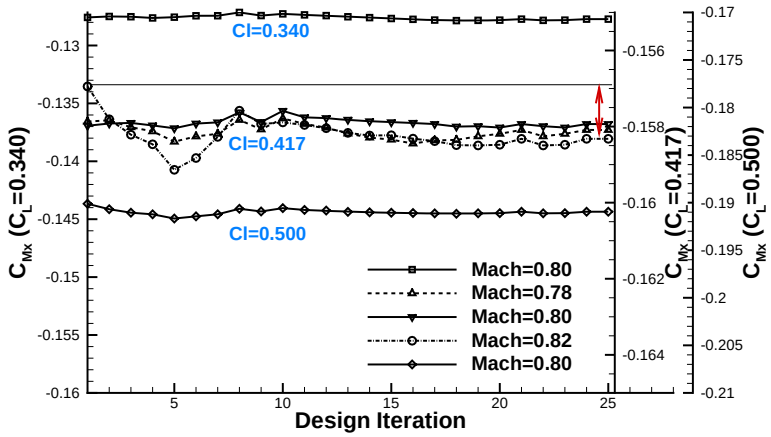

Figure 59: C_{MX} convergence throughout the constrained multi-point optimization

The rolling moment constraint convergence is illustrated in Figure 59. C_{MX} was kept almost constant for the five points during the constrained multi-point optimization, with point 4 (at Mach=0.82) having the highest deviation of 0.75 % from its initial value (highlighted in red). Consequently, the assumption that one point is enough to constrain the rolling moment is valid and recommended for such gradient-based optimization.

Finally, to compare the multi-point and the single point constrained optimizations, the *LoD* and the drag rise trends are plotted in Figure 60 and Figure 61, respectively. Both figures confirm that, as in the unconstrained optimizations, the multi-point optimization show better overall performance than the baselines and the single-point final design. The single-point design however, still performs better at the design point.

5.5 Computational Efficiency

Since efficiency is the driver of this study, this section provides an estimation of the computational costs that were required during the four optimizations. The optimizations employed the same *CFD* and *CSM* grids (same grid sizes), and ran over the same number of processors, therefore, it is possible to compare the costs of the various optimizations.

Figure 29, which presents the main components of the optimizations, defines the optimization process in three main blocks; the mesh deformation block, the aeroelastic coupling block and the aeroelastic coupled adjoint block. The mesh deformation tool is very efficient; hence, its cost will be neglected, which leaves only two blocks for cost considerations.

In the unconstrained single-point optimization, the aeroelastic coupling converged after six iterations, whereas in the constrained optimization, seven iterations were required. The reason behind that is that the rolling moment coefficient is more sensitive to the wing elasticity than the drag and lift, and hence required more flow iterations to converge. On the other hand, the unconstrained multi-point optimization required 20 iterations (for the 5 points) to converge, whereas the constrained multi-point optimization required 21 iterations.

The coupled aero-elastic adjoint has to be solved, as mentioned earlier, one time for each objective or constraint, and for each different flight condition. This means, for example, that the unconstrained single-point optimization requires two coupled adjoint computations whenever the gradients are required one for drag and one for lift. Table 6 shows the number of coupled adjoint required for each optimization scenario whenever the gradients are required.

	Single-Point Unconstrained	Single-Point Constrained	Multi-Point Unconstrained	Multi-Point Constrained
C_D	1	1	5	5
C_L	1	1	5	5
C_{MX}	0	1	0	1
Sum	2	3	10	11

Table 6: Number of required coupled adjoint computations whenever the gradient is required

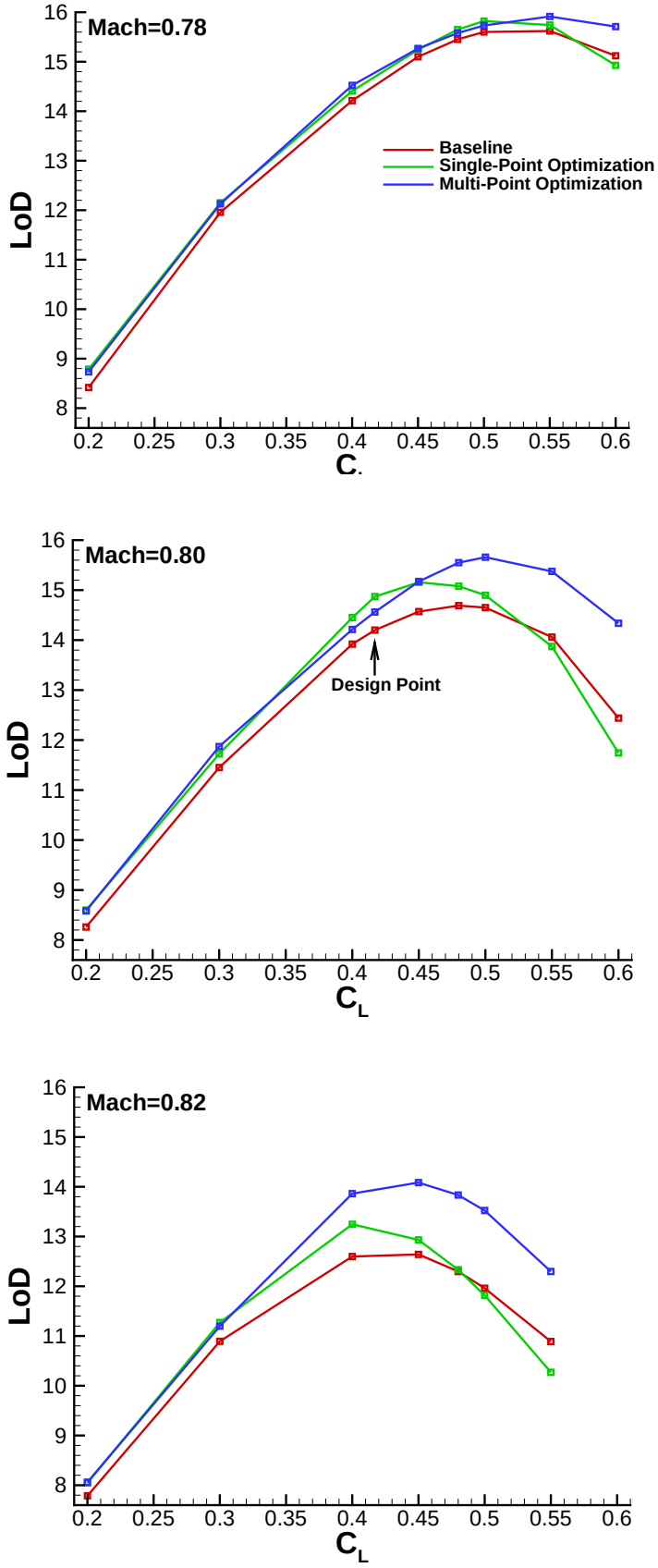

Figure 60: The LoD trends for the constrained optimizations

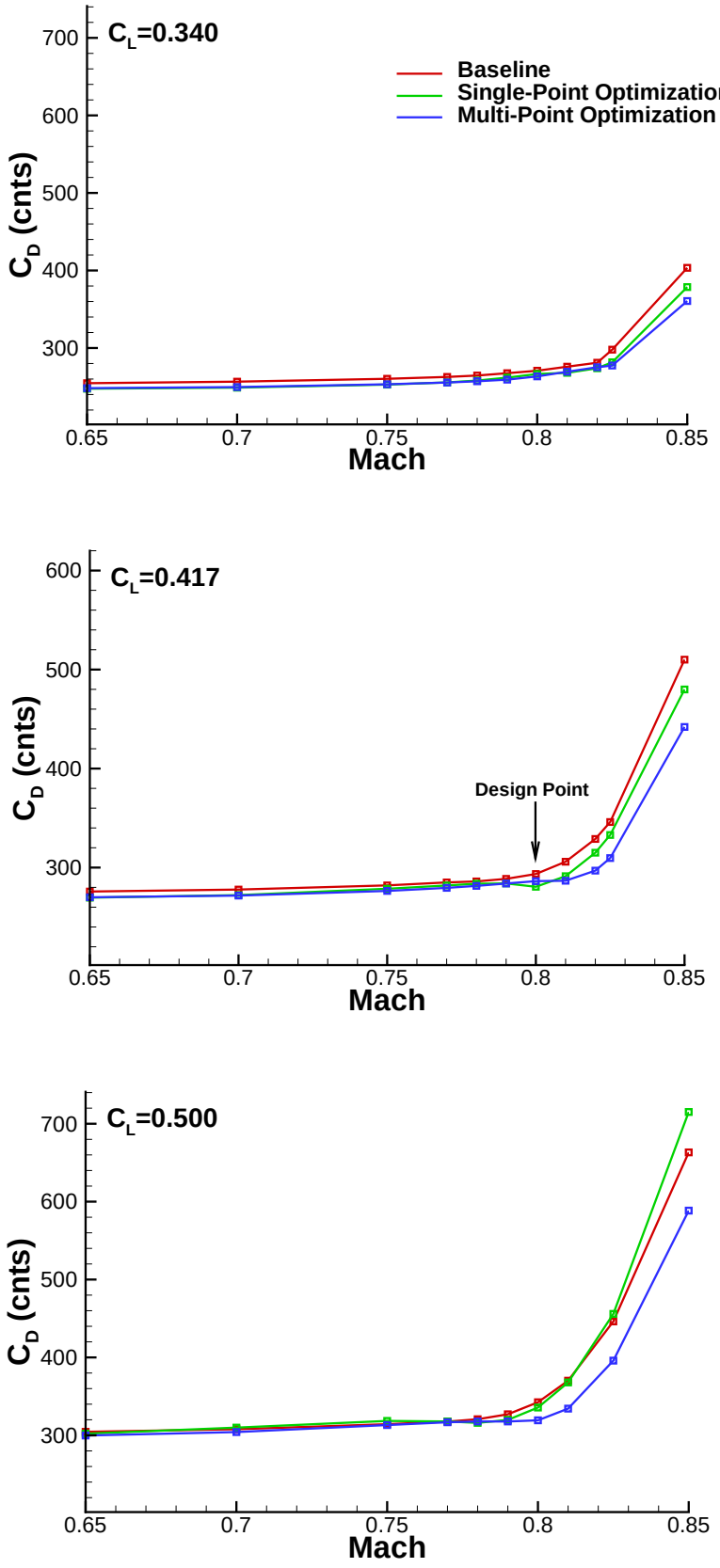

Figure 61: The drag rise trends for the constrained optimization

Obtaining the gradients of one cost function or constraint required almost the same time of one converged aeroelastic coupling iteration (6 flow structure couplings). To make the cost estimation easier, it will be indicated in terms of units, where one cost unit is one coupled aeroelastic iteration. This means, for example, that the cost of computing one converged state solution for the unconstrained single point optimization is equal to 6 cost units (it required 6 aeroelastic couplings), whereas the cost of computing one gradient (2 cost functions) for the same optimization is 12 cost units (as Table 6 presents).

Table 7 presents the computational cost of the various optimizations in cost units. In addition to the assumptions mentioned earlier, the table assumes that the computational cost of the adjoint is equal for all cost functions, where during the optimizations, it was realized that computing the adjoint for C_L requires slightly more time than for the other functions.

	Single-Point Unconstrained	**Single-Point Constrained**	**Multi-Point Unconstrained**	**Multi-Point Constrained**
Cost of State (unit)	6	7	20	21
Cost of Gradient (unit)	12	18	60	66
Number of States	38	28	42	25
Number of Gradients	25	19	11	20
Summed Cost (unit)	528	538	1500	1845

Table 7: Computational cost of the various optimizations

As the table presents, the constrained optimizations cost more than the unconstrained ones, since more adjoint computations are required per state computation, and adjoint computational cost dominates in comparison to state computational cost. The table also shows that less state computations were required in the constrained optimizations, when compared to the unconstrained ones.

Chapter 6: Conclusions and Outlook

The use of MDO in aircraft design can save a lot of the iterative work among the different departments that represent different disciplines. Gradient-based algorithms are efficient and well suited for high fidelity MDO. This thesis attempted at eliminating the obstacle that faces the use of the efficient gradient-based optimization algorithms in MDO context, and then applied the developed work on industry-relevant cases.

Several aspects have to be considered for adequate and reliable wing shape optimizations. The first aspect is the accurate prediction of the flow over the wing. This requires engaging high-fidelity *CFD* models that consider the flow viscosity, and considering the wing elasticity that directly affects the flow, during the optimization. The second aspect lies in employing high number of design parameters for the optimization in order to cover a large design space. The third aspect lies in performing the optimization at several flight points rather than at a single design point. This yields a design that performs better at several aircraft operating conditions.

The coupled aero-elastic adjoint approach developed in this work provides an efficient way to compute the gradients. These gradients can then be employed in aero-elastic wing optimizations whilst considering all the mentioned aspects necessary for realistic wing design. An existing viscous flow adjoint approach has been further developed in order to consider the wing elasticity and was afterwards employed in four optimization scenarios.

The inclusion of the elasticity effects within the adjoint approach resulted in two iteratively solved equations; a flow-dominant adjoint equation (72) and a structure-dominant adjoint equation (73). The flow-dominant adjoint equation is the same as the flow adjoint equation, added to it a term on the right-hand side. This term is obtained by differentiating the interpolation tool that interpolates pressure into forces during the aero-structure coupling process.

The structure-dominant adjoint equation, on the other hand, has the same form as the structure residual equation (42). Hence, it can be solved using the same structure solver. Furthermore, it can be solved using an external linear solver. Both methods were successfully used.

After the implementation, the aeroelastic gradients were validated against the central finite differences approach, and they matched very well. The computational time required for finding the aeroelastic gradients of nine design parameters with the adjoint approach was equal to 20% of that using the finite differences approach. Nevertheless, the more the number of design variables, the more the computational savings in comparison to finite differences. This result shows the main gain of this thesis.

In an attempt to industrialize the developed work, two optimization scenarios were performed on an industry-relevant wing-body configuration, one unconstrained, and one constrained. Both scenarios were tested for single-point as well as multi-point design optimizations, always keeping the lift and the wing thickness implicitly constant. In the multipoint optimization, the five considered flight conditions were given the same weighting factor. It was concluded here that multipoint optimizations, which are now possible to execute using the adjoint approach, produce better designs than single-point

optimizations, since they could enhance the design over a larger range of operating points. Furthermore, it is up to the designer to decide which operating point deserves which weighting factor, depending on the flight mission that the aircraft will be flying.

Constraining the rolling moment (or the wing root bending moment) proved to be useful on the structure side since it keeps the centre of lift constant when the optimizations run for a target lift, which decreases the stress level in the wing structure. In multipoint optimizations, it was found that applying the rolling moment constraint on one point only was enough to hold the constraint at the other points. This saved a considerable amount of computational power since the gradient of the constraints had to be computed only once, instead of being computed five times whenever the gradients are required.

The next step in this field would be including the structural thickness as design parameters, and performing aero-structural optimizations, rather than aeroelastic shape optimizations. This requires developing a method to find the sensitivities of the aerodynamic cost functions with respect to the structural design parameters, and the structural cost functions with respect to the aerodynamic shape design parameters.

Since the nature of the structural problem is different from that of the aerodynamic problem, a different way needs to be investigated. The structural problem includes much more constraints than design variables, which eliminates the advantages of the adjoint approach there. For this reason, this thesis did not develop the adjoint approach for the structure objectives.

Furthermore, the future optimizations should be performed for the whole aircraft including the engine and the horizontal tailplane, which is required for stabilizing the aircraft and maintaining the pitching moment. This will require including a gradient correction term to the gradient of the cost function, in order to account for the change in flow, and hence the gradients, due to the movement of the horizontal tailplane.

References

1 : Flightpath 2050: http://ec.europa.eu/transport/air/doc/**flightpath2050**.pdf

2: N.Gauger, *Adjoint approach in aerodynamic shape optimization and MDO context*, European conference on Computational Fluid Dynamics ECCOMAS CFD 2006, TU Delft, The Netherlands, (ISBN 90-9020970-0), paper no. 639, (2006)

3 : D. Roman, R.Gilmore, S.Wakayama, *Aerodynamics of High-Subsonic Blended-Wing-Body Configurations*, 41 ASME, AIAA 2003 554, (2003)

4 : S.Obayashi, K. Nakahashi, A, Oyama, N. Yoshino, *Design Optimization of Supersonic Wings Planform Using Evolutionary Algorithms*, ECCOMAS (1998)

5 : T.Wunderlich, *Multidisciplinary Wing Optimization of Commercial Aircraft with Consideration of Static Aeroelasticity*, CEAS Aeronautics Journal, DOI 10.1007/s13272-015-0151-6 (2015)

6 : H. Barnewitz, *Flexible Wing Optimization Based on Shapes and Structures*, MEGADESIGN and MegaOpt, NNFM 107, pp. 278-305. Springer (2009)

7 : F. Daoud et al. *Multidisciplinary Airframe Design Process: Incorporation of Steady and Unsteady Aeroelastic Loads,* AIAA 2012-5715 (2012)

8 : G. Schuhmacher, *Multidisciplinary Design Optimization of a Regional Aircraft Wing Box*, AIAA 2002-5406 (2002)

9 : P. Piperni, A. DeBlois, and R. Henderson, *Development of a Multilevel Multidisciplinary Optimization Capability for an Industrial Environment;* AIAA JOURNAL Vol. 51, No. 10, October 2013.

10 : P.E. Macmillin, *Multidisciplinary optimization of the high-speed civil transport*, Multidisciplinary Design Optimization; State of the art, p. 153-171

11 : Python Programming Language; http://python.org

12 : J. Nocedal, S.Wright, *Numerical Optimization*, Page:2, ISBN 0-387-98793-2

13 : J.Brezillon, M. Abu-Zurayk, *Aerodynamic Inverse Design Framework using Discrete Adjoint Method*, 17th DGLR-Fach-Symposium der STAB, (2010)

14 : A. Jameson, *Aerodynamic Shape Optimization Using the Adjoint Method.* VKI Lecture Series on Aerodynamic Drag Prediction and Reduction, von Karman Institute of Fluid Dynamics, P. 3-7 (2003)

15 : M. Vázquez A. Dervieux B. Koobus, *Aeroelastic coupling in sonic boom optimization of a supersonic aircraft*. INRIA report, (2003)

16 : J. Sobieski, R. Haftka. *Multidisciplinary aerospace design optimization: survey of recent developments*, AIAA 96-0711, (1996)

17: J. Periaux, E whitney, L. Gonzalez, *Distributed multidisciplinary design optimization in aeronautics using EA, game theory and hierarchy*, Multidisciplinary Methods for Analysis Optimization and Control of Complex Systems Mathematics in Industry Volume 6, 2005, pp 249-281.

18 : J. Martins, J. Alonso, J. Reuther, *A Coupled-Adjoint Sensitivity Analysis Method for High-Fidelity Structural Design*, Optimization and Engineering, 6, 33-62, (2005).

19 : A. Fazzolari, N. Gauger and J. Brezillon, *Sensitivity Evaluation for Efficient Aerodynamic Shape Optimization with Aeroelastic Constraints*. ECCOMAS (2004)

20 : A. Jameson, *Aerodynamic Design via Control Theory*, Princeton University Report MAE 1824, ICASE Report No. 88-64, November (1988).

21 : N. Kroll, R. Heinrich, W. Krueger, B. Nagel, *Fluid-Structure Coupling for Aerodynamic Analysis and Design: A DLR Perspective*, AIAA 2008-561 (2008).

22 : E. Elsholz, *Fluid-Structure Coupling: Simplified Structural Model on Complex Configurations*, MEGADESIGN and MegaOpt, NNFM 107, p.169-178. (2009)

23 : S. Keye, *Fluid-Structure Coupled Analysis of a Transport Aircraft and Flight-Test Validation*, Journal of Aircraft, Vol. 48 No. 2 March-April (2011)

24 : A.Ronzheimer, F.J.Natterer, J.Brezillon, *Aircraft Wing Optimization Using High-Fidelity Closely Coupled CFD and CSM methods*, 13th AIAA/ISSMO Multidisciplinary analysis optimization conference, AIAA 2010-9078, 13-15 September (2010)

25 : A. Giunta, J. Sobieszczanski-Sobieski, *Progress Towards Using Sensitivity Derivatives in a High-Fidelity Aaeroelastic Analysis of a Supersonic Transport*, AIAA, Reston, VA, pp. 441–453 (1998).

26 : O. Pironneau, *On Optimum Design in Fluid Mechanics*, Journal of Fluid Mechanics, Volume 64, Issue01, pp 97-110, (1974)

27 : E. Haug, K. Choi, V. Komkov, *Design Sensitivity Analysis of Structural Systems*. P. 104-129, Academic Press, London (1986)

28 : J. Reuther, J. J. Alonso, J. R. R. A. Martins, and S. C. Smith, *A Coupled Aero-Structural Optimization Method for Complete Aircraft Configurations*, in Proceedings of the 37th AIAA Aerospace Sciences Meeting and Exhibit, Reno, NV, AIAA 99-0187, (1999)

29 : J. Martins, J. Alonso, J. Reuther, *High-Fidelity Aerostructural Design Optimization of a Supersonic Business Jet*, Journal of Aircraft, Vol. 41, No. 3, May-June (2004)

30 : K. Maute, N. Nikbay, C. Farhat, *Coupled Analytical Sensitivity Analysis and Optimization of Three-Dimensional Nonlinear Aeroelastic Systems*, AIAA JOURNAL Vol. 39, No. 11, November (2001).

31 : Kroll, N., Rossow, C.-C., Schwambom, D., Becker, K., Heller, G.: “MEGAFLOW-A Numerical Flow Simulation Tool for Transport Aircraft Design”. ICAS Congress 2002, Toronto (can), 09.-13.09.2002, ICAS, CD-Rom, S. 1.105.1–1.105.20, (2002)

32 : MSC-NASTRAN Software; http://www.mscsoftware.com/products/cae-tools/msc-nastran.aspx

33 : K. Leoviriyakit, A. Jameson. *Aero-structural wing planform optimization*. AIAA paper 2004-0029, 42nd Aerospace Sciences Meeting & Exhibit, Reno, Nevada, January (2004).

34 : K. Leoviriyakit, A. Jameson. *Case studies in aero-structural wing planform and section optimization*. AIAA paper 2004-5372, 22nd Applied Aerodynamics Conference and Exhibit, Providence, Rhode Island, (2004)

35 : K. Leoviriyakit, S. Kim, A. Jameson. *Aero-structural wing planform optimization using the Navier-Stokes equations*. AIAA paper 2004-4479, 10th AIAA/ISSMO Multidisciplinary Analysis and Optimization Conference, Albany, New York, (2004)

36 : A. Jameson, K. Leoviriyakit, S. Shankaran, *Multi-Point Aero-Structural Optimization of Wings Including Planform Variation*, 45th Aerospace Sciences Meeting and Exhibit, (2007)

37 : K. James, G. Kennedy, and J. R. R. A. Martins, *Aerostructural Topology Optimization of an Aircraft Wingbox*. In: Proceedings of the CASI AERO 2011 Conference. Proceedings of the CASI AERO 2011 Conference. Montreal, QC; 2011

38 : G. Kennedy, J. Martins, *A Comparison of Metallic and Composite Aircraft Wings Using Aerostructural Design Optimization* 12th AIAA Aviation Technology, Integration, and Operations (ATIO) Conference and 14th AIAA/ISSM (2012)

39 : G. Kenway, G. Kennedy, and J. R. R. A. Martins. *Scalable Parallel Approach for High-Fidelity Steady-State Aeroelastic Analysis and Adjoint Derivative Computations*, AIAA Journal, Vol. 52, No. 5 (2014), pp. 935-951.

40 : M. Marcelet, J. Peter, G. Carrier, *Sensitivity Analysis of a Strongly Coupled Aero-Structural System Using Direct and Adjoint Method*, 12th AIAA/ISSMO MDO conference (2008)

41 : I. Ghazlane, G. Carrier, A. Dumont, J. Desideri, *Aerostructural Adjoint Method for Flexible Wing Optimization*, 8th AIAA MDO conference, AIAA-2012- 1924 (2012)

42 : E. Özkaya, N. Gauger, *An efficient One-Shot Algorithm for Aerodynamic Shape Design*, Numerical and Experimental Fluid Mechanics, Notes on Numerical Fluid Mechanics and Multidisciplinary Design Volume 112, pp 35-42, (2010)

43 : T. Rowan. *Functional stability analysis of numerical algorithms*. Dissertation, Dept. Of computer science, University of Texas, USA, (1990)

44 : J. Nelder, R. Mead, *A simplex method for function minimization*, Computer Journal**7**: 308–313. (1965)

45 : W. Hager, H. Zhang, *A Survey of Nonlinear Conjugate Gradient Methods*, Pacific journal of Optimization, Vol. 2, No. 1, pp. 35-58 (2006)

46 : P. Gill, W. Murray, *Quasi-Newton Methods for Unconstrained Optimization*, Journal of the Institute of Mathematics and its Applications 9, pp. 91-108, (1972)

47 : W. Davidon, *Variable Metric Method for Minimization*,SIAM J. OPTIMIZATION Vol. 1, No. 1, pp. 1-17, February (1991)

48 : J. Matrin, P. Strudza, J. Alonso, *The Complex-Step Derivative Approximation*, ACM transactions on Mathematical Software, Vol. 29, No. 3, Sept. 2003, P. 245-262.

49: C. Le, T. Bruns, D.Tortorelli, *A gradient-based, parameter-free approach to shape optimization*, Computational Methods Appl. Mech. Eng. 200 (2011) 985–996.

50 : M.B. Giles, M.C. Duta, J.-D. Muller and N.A. Pierce. *Algorithm developments for discrete adjoint methods*. AIAA Journal, 41(2):198-205, (2003)

51: Technical Documentation of the DLR-TAU code, Technical report (IB), DLR Institute für Aerodynamik und Strömungstechnic, Braunschweig/Göttingen (2014)

52: J. D. Anderson, *Computational Fluid Dynamics, the basics with applications*, McGraw-Hill Inc New York, ISBN 0-07-001685-2, (1995)

53: J. Brezillon, R. Dwight and M. Widhalm, *Aerodynamic Optimization for Cruise and High-Lift Configurations*. Notes on Numerical Fluid Mechanics and Multidisciplinary Design, Volume 107, *Edited by N. Kroll and D. Schwamborn*, Springer, ISBN 978-3-642-04092-4, (2009)

54 : M. Widhalm, et al. *Investigation on Adjoint Based Gradient Computations for Realistic 3d Aero-Optimization*, 13th AIAA/ISSMO Multidisciplinary Analysis Optimization Conference, (2010)

55 : J. Brezillon, R. Dwight and M. Widhalm, *Aerodynamic Optimization for Cruise and High-Lift Configurations.* Notes on Numerical Fluid Mechanics and Multidisciplinary Design, Volume 107, *Edited by N. Kroll and D. Schwamborn*, Springer, ISBN 978-3-642-04092-4, (2009)

56 : PETSc, www.mcs.anl.gov/petsc/

57: A. Naumovich, M. Forster, R. Dwight. *Algebraic Multigrid within Defect Correction for the Linearized Euler Equations*. Linear Algebra Appl. 17:307–324. (2010)

58 : Nielsen and Park: *Using an Adjoint Approach to Eliminate Mesh Sensitivities in Computational Design*, AIAA 2005-0491: Reno (2005)

59: J. Brezillon1, A. Ronzheimer, D. Haar, M. Abu-Zurayk, M. Lummer, W. Krüger, F. Natterer, *Development and application of multi-disciplinary optimization capabilities based on high-fidelity methods,*

53rd AIAA/ASME/ASCE/AHS/ASC Structures, Structural Dynamics, and Materials Conference (2012)

60 : A. Ronzheimer, *Shape parameterization Using Freeform Deformation*. In: MEGAFLOW- Numerical Flow Simulation for Aircraft Design, ISBN 3-540- 24383-6 (2005)

61 : Centaursoft "CENTAUR" : www.centaursoft.com/

62 : P. Spalart, S. Allmaras, A *One-Equation Turbulence Model for Aerodynamic* Flows, AIAA Paper 92-0439 (1992)

63 : P.Flick, M.Love, P.Zink, *The Impact of Active Aeroelastic Wing Technology on Conceptual Aircraft Design*, RTO AVT Specialists' Meeting, Canada, (1999)

64: M.Vázquez, A.Dervieux, B.Koobus, *A methodology for the shape optimization of flexible wings*, Engineering Computations, Vol. 23 Iss: 4, pp.344 – 367. (2006)

65 : P.Röhl, D.Mavris, D. Schrage, *Combined Aerodynamic and Structural Optimization of a High-Speed Civil Transport Wing*, AIAA-95-1222 (1995)

66 : K. Maute, M. Allen, *Conceptual design of Aeroelastic Structures by Topology Optimization*, Structural and Multidisciplinary optimization volume 27, issue 1-2, p. 27-42. (2004)

67 : J. Cebral. *Loose Coupling Algorithms for Fluid Structure Interaction*, PhD thesis, Institute for Computational Science and Informatics, George Mason University, (1996)

68 : K. Park, C. Felippa. *Partitioned analysis of coupled systems*, Computational Methods for Transient Analysis in Computational Methods in Mechanics, 1:157,218, (1983)

69 : R. Heinrich, *Development and Application of TAU–ANSYS Coupling Procedure*, Results of the Closing Symposium of the MEGADESIGN and MegaOpt Projects, Springer–Verlag, New York, 2009, pp. 151–168.

70 : S. Jakobsson, O. Amoignon, *Mesh Deformation Using Radial Basis Functions for Gradient-Based Aerodynamic Optimization*, FOI-R- -1784- -SE, scientific report Dec. (2005)

71 : Y.C.Fung, *An Introduction to the Theory of Elasticity*, ISBN: 9780486469362, sec 1.3, page 18, (2002)

72: R. Heinrich, J. Wild, T. Streit, B. Nagel: *Steady fluid-structure coupling for transport aircraft.* DGLR-Tagung 2006 in Braunschweig, DGLR-Jahrbuch 2006, Band III, (2006)

73: I.J. Schoenberg: *On certain metric spaces arising from Euclidean spaces by a change of metric and their imbedding in Hilbert space*, Annals of Mathematics, 38 (1937), 787-793.

74 : A. Fazzolari, *An Aero-Structure Adjoint Formulation for Efficient Multidisciplinary Wing Optimization*, PhD Thesis, TU-Braunschweig (2006)

75: G. Zilliac,T. Pulliam et al, *A Comparison of the Measured and Computed Skin Friction Distribution on the Common Research Model*, AIAA 2011-1129 (2011)

76 : J. Vassberg, *A Unified Baseline Grid about the Common Research Model Wing-Body for the fifth AIAA CFD Drag Prediction Workshop,* 29th AIAA Applied Aerodynamics Conference, (2011)

77: C. Ilic, M. Wildham, J. Brezillon, *Efficient polar optimization of transport aircraft in transonic RANS flow using adjoint gradient based approach,* ECCOMAS (2012)